

**EXTENSIVE ANALYSES ON LARGE AMPLITUDE GUSTY-  
WIND-INDUCED VIBRATIONS OF OVERHEAD  
TRANSMISSION LINE SYSTEMS**

ガスト風に起因した架空送電線システムの  
大振幅振動に関する詳細解析

2014年3月

埼玉大学大学院理工学研究科（博士後期課程）

理工学専攻                      山口宏樹

提出者氏名                      Pham Viet Hung

# TABLE OF CONTENTS

**ACKNOWLEDGEMENT**

**ABSTRACT**

**LIST OF TABLES**

**LIST OF FIGURES**

<b>Chapter 1 .....</b>	<b>1</b>
<b>Introduction.....</b>	<b>1</b>
1.1. INTRODUCTION OF TRANSMISSION LINE SYSTEMS .....	1
1.2. STATEMENT OF RESEARCH PROBLEM AND LITERATURE REVIEW.....	4
1.3. RESEARCH MOTIVATION AND OBJECTIVES .....	7
1.4. MAJOR WORKS AND RESEARCH METHODOLOGY.....	7
1.5. STRUCTURE OF DISSERTATION .....	8
1.6. CONCLUSIONS .....	11
REFERENCES.....	12
<b>Chapter 2 .....</b>	<b>15</b>
<b>Full-scale measurement and preliminary study on the field data .....</b>	<b>15</b>
2.1. INTRODUCTION .....	15
2.2. FULL-SCALE MEASUREMENT .....	23
2.3. DISCUSSION ON FIELD-MEASURED WIND VELOCITY .....	27
2.4. IDENTIFICATION OF FIELD-MEASURED VIBRATION RESPONSES .....	29
2.5. CONCLUSIONS .....	38
REFERENCES.....	39
<b>Chapter 3 .....</b>	<b>40</b>
<b>Characterization of responses with eigenvalue analysis .....</b>	<b>40</b>
3.1. STATIC EQUILIBRIUM CONFIGURATION .....	40

3.1.1. <i>Introduction</i> .....	41
3.1.2. <i>Catenary theory based static equilibrium configuration of conductor</i> .....	42
3.1.3. <i>Sag-to-span ratio</i> .....	43
3.1.4. <i>Deriving static equilibrium configuration of conductor FE model</i> .....	44
3.1.5. <i>Convergence criteria</i> .....	45
3.2. FINITE ELEMENT MODEL OF THE TRANSMISSION LINE SYSTEM .....	47
3.3. NATURAL FREQUENCIES AND MODE SHAPES.....	50
3.4. INTERPRETATION OF CHARACTERISTICS OF FIELD-MEASURED VIBRATION .....	52
3.5. CONCLUSIONS .....	54
REFERENCES.....	55
<b>Chapter 4</b> .....	<b>56</b>
<b>Interpretation of field-measured responses based on gust response analysis</b> .....	<b>56</b>
4.1. INTRODUCTION .....	56
4.2. BUFFETING THEORY .....	57
4.3. ASSUMPTIONS ON PARAMETERS IN GUST RESPONSE ANALYSIS .....	60
4.4. RESULTS OF GUST ANALYSIS AND COMPARISON WITH FIELD MEASURED RESPONSES.....	62
4.4.1. <i>Gust response analysis of Line A</i> .....	62
4.4.2. <i>Gust response analysis of Line B</i> .....	64
4.4.3. <i>Gust response analysis of Line C</i> .....	68
4.5. CONCLUSIONS .....	70
REFERENCES.....	71
<b>Chapter 5</b> .....	<b>72</b>
<b>Prediction of large amplitude gust response in time domain</b> .....	<b>72</b>
5.1. INTRODUCTION .....	72
5.2. TIME-DOMAIN-GUST-RESPONSE ANALYSIS.....	73
5.2.1. <i>Typical time series of the vibration response</i> .....	74
5.2.2. <i>Equation of motion</i> .....	74
5.2.3. <i>Solution of the vibration response analysis</i> .....	75
5.3. WIND-FIELD SIMULATION .....	76

5.3.1. Introduction .....	76
5.3.2. Hypotheses for wind field simulation.....	77
5.3.3. Theory of wind-field simulation .....	77
5.3.4. Application of wind-field simulation .....	80
5.4. GUST RESPONSE SIMULATION .....	84
5.4.1. Assumptions on parameters .....	84
5.4.2. Time-domain gust response analysis.....	85
5.5. REMARK AND FUTURE WORKS .....	89
REFERENCES.....	90
<b>Chapter 6 .....</b>	<b>91</b>
<b>Conclusions.....</b>	<b>91</b>

**Appendix – A**

**Appendix – B**

**Appendix – C**

**Appendix – D**

**Appendix – E**

# ACKNOWLEDGEMENT

First of all, I would like to express my special thanks and sincere gratitude to my supervisor, Professor Hiroki Yamaguchi, for his guidance, everlasting inspiration, constant encouragement and patience in teaching me throughout my graduate study program.

I am grateful to Professor Yoshiaki Okui, Professor Yasunao Matsumoto and Associate Professor Masato Saitoh, the members of my advisory committee, for their helpful review and constructive criticism of this dissertation.

The research was accomplished under the support of the Tokyo Electrical Power Company (TEPCO) in providing the field data details of the transmission lines. Support of the organization is appreciated.

Special thanks are extended to the staffs and friends from my laboratory, Department of Civil and Environmental engineering, Graduate School of Science and Engineering and from Saitama University for their assistance and support during the course of my graduate study.

I shall ever remain indebted to my wife T. Phuc, my son Q. Minh and my daughter P. Thao for their loves, kind blessings and the moral support during my stay away from home.

Finally, I would like to express 'Thanks' to my parents, to whom I dedicate this dissertation.

# ABSTRACT

Large amplitude wind-induced vibrations of ice-accreted/unaccreted conductors in overhead transmission lines are frequently observed in the field. Damage due to the large vibrations is costly and affects many aspects of modern society. In this study, an attempt is made to identify the large amplitude gust responses and to distinguish them from the unstable phenomena of galloping in field-observed vibrations of long-span-overhead transmission lines that have bundled conductors. An extensive method of combining field-measured data analysis, eigenvalue analysis and gust response analysis is applied. The field-measured wind and vibration characteristics and their relations are first discussed to study preliminarily the types of field-measured responses. Next, the natural frequencies and mode shapes of the transmission lines are estimated by eigenvalue analysis using reliably created finite element models to verify the field-measured response characteristics in the frequency domain. Gust response analysis is finally conducted to interpret intensively the large-amplitude gust responses of overhead conductors, and results in good agreement with field-measured vibrations. For further interpretation, the time-domain gust-response analysis is conducted. A significant feature of this approach is that the time-dependent characteristics of the unsteady-aerodynamic forces and nonlinearities of both aerodynamic and structural origins can be taken into account.

Through this extensive study, it is concluded that most of the field-measured responses are gust-type vibrations and that a gust response can be sufficiently large to cause damage in the overhead transmission lines, regardless of their type.

## LIST OF TABLES

Table 2.1 Geometrical description of Line A, B and C.....	25
Table 2.2 Number of field data sets from Dec. 2008 to July 2009.....	27
Table 2.3 Maximum of MPPAs of Line A, Line B, and Line C. ....	34
Table 3.1 Specification of the transmission lines: Line A, Line B, and Line C.....	49
Table 3.2 Natural frequencies and mode shapes of transmission lines. ....	51
Table 4.1 Uncertain parameters assumed in gust response analysis. ....	61
Table 4.2 Aerodynamic damping ratios assumed in gust response analysis. ....	62
Table 4.3 Results of RMS comparison .....	63

# LIST OF FIGURES

Fig.1.1: An example of transmission line.....	2
Fig.2.1: (a) The wind field model and (b) turbulence profiles .....	17
Fig. 2.2: Geometries of the transmission lines and cross sections of bundled-conductors: (a) Line A; (b) Line B; and (c) Line C.....	24
Fig. 2.3: Direction and magnitude of mean wind velocity of Line A (refer Hung et al. 2014 for Line B and C).....	28
Fig. 2.4: Turbulence intensity of wind versus normal component of mean wind velocity of Line A (refer Hung et al. 2014 for Line B and C).....	28
Fig. 2.5: PSDs of large amplitude vibrations in Line A at L/2 span. ....	30
Fig. 2.6: PSDs of large amplitude vibrations in Line B: (a) L/2 624m span; (b) L/4 624 m span; (c) jumper; (d) L/2 407 m span; and (e) L/4 407 m span. ....	31
Fig. 2.7: PSDs of large amplitude vibrations in Line C at L/2 span.....	32
Fig. 2.8: RMS response versus normal component of mean wind velocity of Line A (refer Hung et al. 2014 for Line B and C). ....	33
Fig. 2.9: MPPA response versus normal mean wind velocity for Line A (refer Hung et al. 2014 for Line B and C). ....	34
Fig. 2.10: Time series of Line A at L/2. ....	35
Fig. 2.11: Time series of Line B: (a) L/2 624 m span; (b) L/2 407 m span, (d) jumper.....	36
Fig. 2.12: Time series of Line C: (a) L/4 439 m span; (b) L/4 421 m span.....	37
Fig. 3.1: Change in natural frequencies with respect to sag-to-span ratio and the position of Line A, B and C.....	43
Fig. 3.2: Scheme of iterative algorithm. ....	45
Fig. 3.3: Scheme of Effect of Tolerance Size on Solution .....	46
Fig. 3.4: Convergence checking based on sag tolerance of three lines .....	46
Fig.3.5: FE models of the transmission lines: (a) Line A; (b) Line B; and (c) Line C.....	48
Fig.3.6: Coupling of jumper motion with two-loop torsional mode of 407 m span in Line B.....	51
Fig.3.7: Examples of PSD of field measured responses of Line A (due to copyright of Elsevier, refer Hung et al. 2014 for Line B and C).....	53
Fig. 4.1: Davenport’s approach for wind-induced resonant response (Davenport 1967).....	58
Fig. 4.2: Horizontal RMS comparison at L/2 of 615 m span in Line A (refer Hung et al. 2014 for other RMS comparisons). ....	63
Fig. 4.3: Horizontal PSD comparison at L/2 of 615 m span in Line A (refer Hung et al. 2014 for other PSDs). ....	64

Fig. 4.4: RMS comparison of coupled jumper and span responses in Line B: (a) Torsional RMS of jumper; (b) Torsional RMS of quarter-point 407 m span. ....	65
Fig. 4.5: PSD Comparison of jumper in Line B. (a) Torsional PSD of jumper and (b) Torsional PSD of quarter-point 407 m span. ....	65
Fig. 4.6: RMS comparison at L/2 of 407 m span in Line B. ....	66
Fig. 4.7: Time series of responses in Events No. 1 and No. 2: (a) Horizontal, (b) Vertical, (c) Torsional, (d) Event No. 2-maximum amplitude torsional, and Event No.1-maximum amplitude torsional responses. ....	67
Fig. 4.8: PSD comparison at L/2 of 407 m span in Line B. ....	67
Fig. 4.9: Comparison of vertical response at L/4 of 439 m span in Line C: (a) RMS; (b) PSD of Event No. 3 (weak agreement) and (c) PSD of Event No. 4 (good agreement). ....	69
Fig.5.1: Typical response time history of structure to wind. ....	74
Fig.5.2: Turbulent field at nodes. ....	78
Fig.5.3: Grid used in turbulence simulation ....	81
Fig.5.4: Comparison of PSD in along wind direction. ....	82
Fig.5.5: Distribution of the wind series along span ....	83
Fig.5.6: Wind time series at node ....	84
Fig. 5.7. Scheme of framework in time-domain gust-response analysis. ....	85
Fig. 5.8. FE model of Line A.....	86
Fig. 5.9. An example of unit wind force of sub-conductor at mid-span with 30s-gredually-increased loading ....	86
Fig. 5.10: Time series of response at mid-span. ....	88

# CHAPTER 1

## INTRODUCTION

- 
1. Introduction of transmission line systems
  2. Statement of research problem and literature review
  3. Research motivations and objectives
  4. Major works and research methodologies
  5. Structure of dissertation
  6. Conclusions
  7. References
- 

### **1.1.Introduction of transmission line systems**

#### *1.1.1. Component of transmission line system*

The high-voltage electrical-power transmission lines that have long span, bundled-conductor are considered in this study. The bundled-conductor transmission line is different from a single-conductor transmission line about both of structure and dynamic characteristic.

An example of transmission line includes some main parts as shown in Fig. 1.1, in which conductor is slender, flexible, and sensitive to wind. The conductor is cable-type element that can carry only tension, neither compression nor bending stiffness. Conductor can be single or bundled-conductor. The bundled conductor is used to reduce

the corona losses and audible noise. For the bundled-conductor, spacers arrange the sub-conductors along span separately. Each spacer connects the sub-conductors by its spacer's arms in one cross section of the conductor bundle. In this study, the 8-conductor (Line A), 4-conductor (Line B), and 2-conductor (Line C) bundles are considered.

The spacers have function to avoid the short-circuit between different phases conductors. Connection between sub-conductors and a spacer may be complicated and significantly affects to the torsional stiffness of the bundled-conductor. The spacers must resist the wind-induced force and magnetic forces that might lead to short-circuit accident.

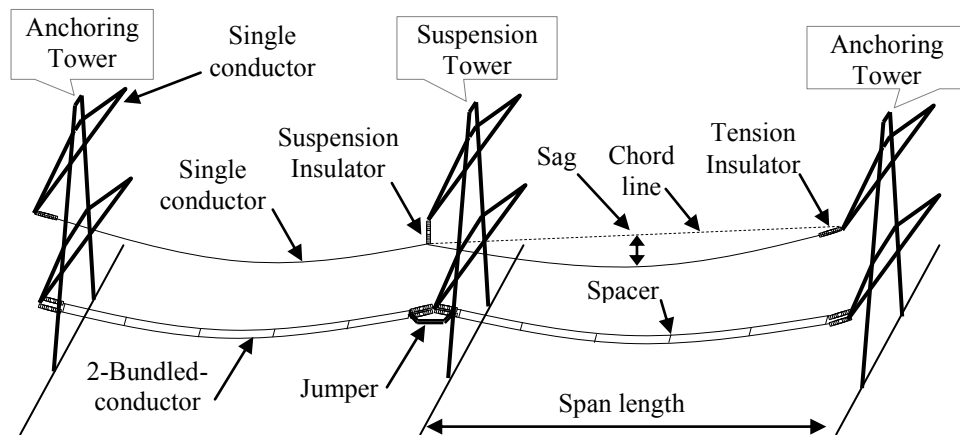


**Fig.1.1:** An example of transmission line.

The bundled-conductor is connected to towers through insulators. The insulator often has very low bending stiffness. The insulators connect tower arms at the one end and yoke plates at the other end. There are two types of insulators, the tension insulators and suspension insulator. The bundled-conductors are attached to the anchoring tower by the tension insulators and to the suspension tower by the suspension insulator.

There are two types of towers, anchoring and suspension tower. The anchoring tower is usually at end of the transmission line or at the direction-changed point of the transmission line. The suspension tower is where the conductors are simply suspended from a horizontal arm the tower and the mechanical tension being the same on each side.

Jumper is sometime employed in connection between bundled-conductors and intermediate tower. In this case, the bundled-conductor goes from this side to other side

of the intermediate tower through the jumper. The bundled-conductor at the left span and the right span of the intermediate tower are connected to the intermediate tower by the insulators. However, the sub-conductors are freely inside jumper pipes. The mechanism of jumper's vibrations might be quite different from the mechanism of span vibrations in the transmission line system. Fig. 2.6 shows the jumper of Line B in the detail.

### *1.1.2. Dynamic characteristics of conductor*

#### *a. Sag of conductor*

Sag is defined as maximum distance that is measured vertically from the conductor to chord line. The chord line is a straight line joining two points of the conductor support. Sag is usually lowest point of cable. Sag is considered as a key parameter to specify the characteristics of conductor because it concerns the conductors' tension, stiffness, and geometry. In transmission line system modeling, sag is employed to find out their appropriate static equilibrium configurations.

#### *b. Torsional stiffness of conductor*

In fact, the torsional stiffness is quite different between a single conductor and a bundled-conductor. When the torsional stiffness of single conductor is constant depending on only the size of conductor, the bundled-torsional stiffness is mainly non-linear and depends on some parameters such as sag-to-span ratio, spacer, and geometry of bundled-conductor and attachment conditions to towers.

In the single conductor, the torsional stiffness is an intrinsic characteristic of the conductors. Wang J. (1970) established a good approximate relation between the intrinsic stiffness and the diameter of the single conductor. In bundled-conductor, it is more complex. Nigol was the first to propose an analytical expression for torsional

stiffness. In his work, the expression is obtained for a symmetrical arrangement of bundled-conductors. He also shows that the design of the so-called “yoke plate” assembly can explain a large part of the physical mechanism of bundled-torsional stiffness and this particularly for dead-end span. The importance of the yoke plate assembly is that it imposes a relationship between the tensions in each sub-conductor during the rotation of the bundled-conductors.

## **1.2. Statement of research problem and literature review**

The basic function of transmission line system is to transmit electricity from power plants. The continuous and efficient functioning of the transmission lines is needed in order to managing the demand-supply balance. Any damage leading to power-supply interruption may be very costly and affects many aspects of the modern society. For meeting this demand, it may need a great effort to understand the dynamic behavior of the transmission line systems, and make the transmission lines to be more structurally reliable.

The electrical-transmission-line systems are engineered structures that traverse over all types of terrain. The transmission line conductors are long, slender, flexible, and wind sensitive structures. The large-amplitude wind-induced vibration of the transmission line conductors is frequently observed in the field. Probably no other structure has as much of its mass in highly flexible form, and so continuously exposed to the forces of wind, as the transmission line conductors expose.

With regard to the causes of large amplitude wind-induced vibrations, people often think that such vibrations of the overhead transmission lines are caused by the galloping unstable phenomenon, which was first identified and explained by Den Hartog (1932). The galloping, which is characterized as a low-frequency, large-amplitude, wind-induced vibration with self-excited mechanism, usually occurs in moderately strong and steady wind, while its incidence is rather infrequent and unpredictable under the interaction of wind and asymmetrically ice or wet snow accreted conductors. The galloping phenomenon is well recognized as one of the major wind induced vibrations to cause damages in the transmission lines. Phase to phase flashovers may occur on

leading to widespread electrical power outages. Large amplitude vibrations of conductors may cause overloads on towers, fatigue damages to hardware as well as insulators and conductors. Galloping is one of the classical problems in the overhead transmission lines under certain climatic conditions. Many researchers through field observations (Yukino et al., 1995; Diana et al., 1990; Rawlins, 1981), wind tunnel experiments (Keutgen, Lilien, 2000; Nakamura, 1980; Novak, Tanaka, 1974; Nigol, Buchan, 1981), and numerical analysis (Yamaguchi et al. 1995; Desai et al., 1995; Ohkuma, Marukawa, 1999) has studied the galloping phenomenon. Furthermore, there has been extensive research on the identification of the galloping mechanism (Nigol, Buchan, 1981; Wang, Lilien, 1998; Blevins, Iwan, 1974; Nakamura, 1998) and its prevention through different devices (Havard, Pohlman, 1979; Hunt, Richards, 1969; Richardson, 1965). An excellent survey of the state of the art on galloping unstable phenomena is given in the technical brochure (CIGRE, 2005).

Since the Den Hartog's findings of galloping phenomena, any large amplitude wind-induced vibration is generally thought to be caused by the galloping unstable mechanism. However, so-called gust response that is a randomly forced vibration in gusty wind can be another source of large amplitude wind-induced vibrations in overhead transmission line conductors (Yamaguchi et al., 2003). Because of the high flexibility of the transmission lines, the possibility of large amplitude random response due to atmospheric gusty wind cannot be overlooked, which is pointed out in numerical analysis (Ohkuma, Marukawa, 1999). It is also confirmed by the analysis of field-measured data (Gurung C.B. et al., 2003; Gull J.H. et al., 2011) that besides the galloping, the occurrence of large amplitude gust response is not only in the horizontal direction but also in the vertical direction. Regarding the computational modeling of gusty wind-transmission line conductor interaction, a refined computational model of the conductor in surrounding moving air is used to investigate the dynamic interaction between wind and conductor motion (Keyhan et al., 2013). In the computational model, wind load time histories are used as input for the nonlinear dynamic analysis with the direct time integration of incremental equations of motion. In consideration of the nonlinear dynamic response of the transmission line conductor subjected to gusty wind in arbitrary direction, the formulation and computing procedure have been proposed and introduced. In the computational modeling, the exact static equilibrium configuration

according to the elastic catenary equation under self-weight, non-leveled supports, arbitrary sag, large displacement and deformation fields etc. have been considered (Impollonia et al., 2011; Miguel et al., 2012; Keyhan et al., 2013). Most of the references emphasized on the computational methods for the transmission line-imposed wind force interaction in time domain, without interpreting the characteristics of the large amplitude gusty wind-induced vibration and validating the methods by full-scale vibration measurements.

Despite of such numerous field observations, studies and applications on the large amplitude wind-induced vibrations for more than a half century, a practical protection method that is recognized as fully reliable has not yet been developed. Minimization or control method for wind-induced vibrations of the transmission lines still depends on field trial and error procedure (Ohkuma, Marukawa, 1999; CIGRE brochure, 2005). The accidents like loosening of bolts, breaking of insulators attachments, spacers, and porcelain plates due to the large amplitude vibrations of the iced and un-iced transmission line conductors in gusty winds are observed even recently by Tokyo Electric Power Company (TEPCO).

For the rational design of the overhead transmission lines and their smooth operation, some measure for controlling both the galloping phenomenon and the gust response is necessary. However, since the characteristics of galloping and gust response are entirely different, the way to minimize or control them would be different. It is, therefore, indispensable to identify galloping and gust responses separately. From that point of view, an extensive method combining of field-measured data analysis, eigenvalue analysis and gust response analysis based on the finite element (FE) model is employed to identify characteristics of large amplitude gust responses observed in the long-span, overhead transmission lines with bundled-conductors.

Through current extensive analysis, the characteristics of field-measured vibration and cause of damages observed in the field by TEPCO are expected to be interpreted properly. The result is a first extensive and intensive analysis on the causes of recently field observed damages in the long span, large bundled-conductor transmission lines. The greatest contribution of the research is to blast embroilments in identification of vibration characteristics in order to do right things in designing as well

as application of vibration control. The results may be a usable reference for other researches on vibration control for minimizing large amplitude vibration and corresponding damages of our popular long span, different-type of the bundled-conductor transmission line systems in gusty wind.

### **1.3. Research motivation and objectives**

Demand of designing and constructing the reliable transmission line system is increasing with increasing of serious damages due to LAV as having been observed in the field recently. Additionally, numerous field observations, studies, and applications on controlling and minimizing the LAV as previously mentioned, no practical protection method has been fully reliable. A number of accidents have been reported in the transmission line system due to LAV as a series of accidents reported by TEPCO.

In systematically studying, the causes of unrealizable protection methods for minimizing vibration amplitude and avoiding damages may be due to misunderstanding the actual characteristics of vibration that is happened and observed in gusty wind climatic condition, different from characteristics of other unstable-phenomena as galloping. Properly understanding of characteristics of field-measured vibration is critical point. The objectives of this research, therefore, are to identify, interpret and distinguish the LAV of the transmission line system due to wind gust measured in the field with other ones based on field measured wind and displacement characteristics, finite element model (FEM) analysis, gust response analysis in frequency domain and time domain.

### **1.4. Major works and research methodology**

In this research, the works can be classified into two categories, in frequency domain and in time domain. In the frequency domain, an extensive method consisting of field-measured data analysis, eigenvalue analysis and gust response analysis based on the finite element (FE) model, is applied to fully identify and interpret the characteristics of large amplitude gust responses observed in the long-span, overhead

transmission lines with bundled-conductors. The field-measured wind and displacement characteristics, such as the mean wind velocity, wind direction, turbulence intensity, root mean square (RMS) and power spectral density (PSD) of wind velocity and response displacement, are first discussed to have an initial idea on the type of field-measured vibrations. The eigenvalue analysis is next conducted to evaluate the response spectral peaks, followed by the gust response analysis in the frequency domain. From the gust response analysis the PSDs and RMS of responses are obtained to compare with the field-measured PSDs and RMS of responses to ascertain the type of field-observed vibrations in different types of the transmission lines. In the second category, the time-domain gust-response prediction is considered. A significant feature of this approach is that the frequency dependent characteristics of unsteady aerodynamic forces and nonlinearities of both aerodynamic and structural origins can be taken into account when estimating the response. All the observed events are associated with large amplitude and a relatively longer period are carefully checked for distinguish large amplitude gust response of galloping response by using time history of structural response and wind force, and Lissajous diagrams.

### **1.5. Structure of dissertation**

Dissertation presents results of an attempt to identify the large amplitude gust responses and to distinguish them from unstable phenomena of galloping in the field-observed vibrations of the transmission lines by employed an extensive method that combines field-measured data analysis, eigenvalue analysis and gust response analysis is applied. Through this study, the characteristics of field-measured vibration and causes of field-observed damages can be identified properly. The following is organization of dissertation in which the mentioned contents are discussed in detail.

In the first chapter, a brief description of the contents of this dissertation is given. In this chapter, a highlight of research topics, objectives, methodologies, the studied transmission line systems, and field measurement is presented.

In Chapter 2, in order to have insight into the characteristics of gusty wind and dynamic response in the field, mean wind direction, mean wind velocity, wind

turbulence intensity, RMS and MPPA, PSD, and time series of the dynamic displacement responses are first studied. In the preliminary interpretation, for example, wind direction is taken into account in comparisons of RMS, MPPA, etc. Turbulence intensities are analyzed to get idea of wind velocity fluctuations. RMS, MPPA, time series give essential information for understanding characteristics of the field large amplitude response of the overhead transmission line conductors. Based on results of parabolic trends of RMS, MPPA and the way large amplitude developed in time, it can be preliminarily conclude that field-measured vibration is possibility of gust response.

In Chapter 3, the dynamic characteristics of the transmission lines have been identified based on the eigenvalue analysis. Finite element models (FEM) of the three transmission line systems are created in FEMAP with NX Nastran computing software. In the creating FE model of the transmission line systems, one of the most important parts is to find out the proper static equilibrium configurations of conductors subjected to the body loads. Therefore, to solve this nonlinear problem, an iterative algorithm is proposed to obtain proper FE models. Then eigenvalue analysis is conducted. The results of natural frequencies and mode shapes are used in interpretation of field-measured vibration and conjunction with gust response analysis in further analysis.

In Chapter 4, the detail interpretation based on the gust response analysis is done by comparison of analytically evaluated RMS responses and all the measured-vibration data at all the measure point of the three transmission lines. It was found that almost all the cases show good agreement. In detail, some important examples of RMS comparison are discussed. From the reasonable agreements between the gust theory-based and the field-observed RMS responses as well as their PSDs, this chapter confirms that the most of the observed vibrations could be gust responses, there might be a possibility of galloping phenomena in some cases, and more vivid interpretation for identifying the galloping phenomenon is required in future.

In Chapter 5, an attempt is made to analyze gust response of the three transmission lines in the time domain. Firstly, in each transmission line analysis, model wind force is given based on field measured wind velocity in along and vertical directions. FE model of the transmission lines associated model of nodal wind forces is analyzed in NX Nastran computing software by using “Direct transient response

analysis” solver. Time series comparison of field-measured data and simulation is presented to investigate the way of large amplitude gust response developed in time. The result may be usable in designing and controlling damages due to large amplitude response. A significant feature of this approach is that the time dependent characteristics of unsteady aerodynamic forces and nonlinearities of both aerodynamic and structural origins can be taken into account when estimating the response.

Chapter 6 shows main conclusions on the characteristics of field-measured vibration, causes of recent damages observed in the field by TEPCO. Conclusions on results of parts are also mentioned.

## **1.6. Conclusions**

In this chapter, a background of the research topic has been presented. Some essential conclusions can be conducted as follows.

It is indispensable to identify properly the characteristics of the field-measured vibration and to distinguish such large-amplitude vibration in the gusty wind with other unstable phenomena as the galloping phenomenon response. That is a critical point to find out the causes of damage observed recently in the field.

Three type of the long span, bundled-conductor transmission lines including an enormous number of the field datasets of the wind velocity and vibration response could be sufficient for a statistic analysis of the stochastic processes as the natural wind turbulence.

The extensive analysis that is combined the three approaches is a potential method to conduct the research objectives based on the field-measurement and theory-based analysis.

**References**

- Blevins R.D., Iwan W., 1974. The galloping response of a two-degree-of-freedom system. *J. Appl. Mech.*, 41, pp. 1113-1118.
- CIGRÉ 2005. "State of the Art of Conductor Galloping, Technical Brochure No. 322"  
CIGRE TF B2.11.06.
- Davenport A.G., 1962. The response of slender, line-like structures to a gusty wind. *Proceeding of the ICE*, 23, pp. 389- 408.
- Den Hartog J.P., 1932. Transmission Line Vibration due to sleet. *AIEE Trans.*, 51, pp. 1074- 1076.
- Desai Y.M. et al., 1995. Finite element modelling of transmission line galloping. *Comput Struct.*, 57, pp. 407- 420.
- Diana G. et al., 1990. Oscillation of bundled-conductors in overhead lines due to turbulent wind. *IEEE Trans Power Delivery*, 5(4), pp. 1910- 1922.
- Gull J.H. et al., 2011. Interpretation of field-measured vibrations in transmission lines by gust response analysis. *Proceedings of 9th International Symposium on Cable Dynamics, Shanghai (China)*, pp. 281- 286.
- Gurung C.B. et al., 2003. Identification of large amplitude wind-induced vibration of ice-accreted transmission lines based on field observed data. *Journal of Wind Engineering and Industrial Aerodynamics*, 91(7), pp. 903- 924.
- Havard D.G., Pohlman J.C., 1979. Field-testing of detuning pendulums for controlling galloping of single and bundled-conductors. *IEEE symposium on Mechanical Oscillations Overhead Transmission Lines, Canada*, pp. 499-5.
- Holme J.D., 2001. *Wind loading of structures*. London Spon Press.
- Hunt J., Richards D., 1969. Overhead line oscillations and the effect of aerodynamic damper. *Proc. IEEE, London*, pp. 1869- 1874.
- Irvine H.M., 1981. *Cable structures*. The MIT Press.
- Keutgen R., Lilien J.L., 2000. Benchmark cases for galloping with results obtained from wind tunnel facilities-validation of a finite element model. *IEEE Trans Power Delivery*, 15, pp. 367- 374.

- Keutgen R., Lilien J., 1998. A new damper to solve galloping on bundled-lines, theoretical background, laboratory and field results. *IEEE Trans.*, 13 (1), pp. 260- 265.
- Keyhan, H., McClure, G., Habashi, W.G., 2013. Dynamic analysis of an overhead transmission line subject to gusty wind loading predicted by wind–conductor interaction. *Computers and Structures* 122, 135–144.
- Matheson, M.J., Holmes, J.D., 1981. Simulation of the dynamic response of transmission lines in strong winds. *Engineering Structures*, Vol.3, Issue 2, 105–110.
- McClure, G., Lapointe, M., 2003. Modeling the structural dynamic response of overhead transmission lines. *Computers and Structures*, 81, 825–834.
- Miguel, L.F.F, Riera, J.D., João Kaminski Jr., Menezes, R.C.R., 2012. Assessment of code recommendations through simulation of EPS wind loads along a segment of a transmission line. *Engineering Structures*, 43, 1–11.
- Nakamura Y., 1980. Galloping of bundled-power line conductors. *J. Sound Vibr.*, 73 pp. 363- 377.
- Nakamura Y., 1998. Galloping of bundled-power line conductors. *J. Sound and Vibration*, 73 (3), pp. 909- 916.
- Nicholas I., 2012. Davenport’s mark on wind engineering. *J. Wind Eng. Ind. Aerodyn.*, pp. 104- 106.
- Nigol O., Buchan P.G., 1981. Conductor galloping part I — Den Hartog mechanism. *IEEE Trans Power Apparatus Syst.*, 100, pp. 699- 707.
- Novak M., Tanaka H., 1974. Effect of turbulence on galloping instability. *J Eng. Mech.*, ASCE, 100, pp. 27- 47.
- Ohkuma T., Marukawa H., 1999. Galloping of overhead transmission lines in gusty wind. *First International Conference on Advances in Structural Engineering and Mechanics*, Seoul (Korea), pp. 71- 76.
- Ramberg S.E., Griffin O.M., 1977. “Free vibration of taut and slack marine cables.” In: *Proceedings of the American Society of Civil Engineers*, Vol. 103.

- Rawlins C.B., 1981. Analysis of conductor galloping field observations — single conductors. *IEEE Trans Power Apparatus Syst.* 100(8), pp. 80- 89.
- Richardson A., 1965. Dynamic damper for galloping conductors. *E.World*, pp. 154- 155.
- Stroman E.N., 2006. *Theory of Bridge Aerodynamics*. Springer.
- Wang J., Lilien J.L., 1998. Overhead electrical transmission line galloping: A full multi-span 3-DOF model, some applications and design recommendations. *IEEE Trans Power Delivery*, 13(3), pp. 909- 916.
- Yamaguchi H. et al., 1995. Galloping analysis of transmission lines with bundled-conductors. *Proceeding of International Seminar on Cable Dynamics, Liege (Belgium)*, 1995, pp. 61–66.

## CHAPTER 2

### FULL-SCALE MEASUREMENT AND PRELIMINARY STUDY

#### ON THE FIELD DATA

---

1. Introduction
  2. Full-scale measurement
  3. Discussion on field-measured wind velocity
  4. Interpretation of field-measured vibration responses
  5. Conclusions
  6. References
- 

#### 2.1. Introduction

To have insight about the characteristics of the field-measured gusty wind and dynamic response of the transmission line systems, the mean wind direction, mean wind velocity, wind turbulence intensity, PSD, RMS, MPPA and the time series of the dynamic displacement responses are first studied. This fundamental information not only is usable for the discussion in this section but also is necessary for the gust response analysis in the other chapters. The field-measured acceleration is numerically integrated twice to obtain the time series of displacement. Before integrating an acceleration record, the data is filtered to remove the low-frequency components of the noise by using the Butterworth high-pass filter with an appropriate-cut-off frequency. In the current analysis, the cut-off frequency of the high-pass filter is set to be a half of the

first natural frequency, 0.05Hz for the data of Lines A and B, and 0.07 Hz for the data of Line C.

### *2.1.1. Study based on field measurement*

The advance-measuring equipment and technique have made it possible to carry out the measurement of full-scale structures such as stay cables, transmission lines, bridges, etc. A main objective of this measurement is to interpret the real phenomena.

Yamaguchi et al. (2003) and Zuo et al. (2009) introduced such efforts made for transmission lines and for stay-cables, respectively. Former have used multi-channel modal analysis in order to separate galloping events from gust response for bundled-conductors in iced storm. In their case, in-plane vertical vibrations were main discussion and classical galloping was identified that is due to coupling of vertical and torsional motion.

EPRI Research report (2005) pointed out that the so-called gust response can be another source of large amplitude wind-induced vibrations in of overhead transmission line conductors.

Yamaguchi et al. (2003, 2011) also confirmed by the analysis of field-measured data that besides the galloping, the occurrence of large amplitude gust response is not only in the horizontal direction but also in the vertical direction.

This study presents many full-scale measurements and observations those have been conducted in the different span-length, type of the bundled-conductor transmission lines for long time. Based on the field data analysis, the characteristics of field-measured large amplitude vibration and effect of difference in span-length, type of bundled-conductor, etc. will be investigated properly. It is desired for rational designing with reliable protection methods.

### *2.1.2. Wind characteristics*

a. Mean wind velocity

Tubino & Solari (2005) presented that wind fluctuates randomly both in time and space. Wind velocity over a given time interval can be considered as consisting of mean wind velocity component  $\bar{U}(x,y,z)$  and fluctuating component  $u(x,y,z,t)$  as shown in Eq. (2.1) and Fig. 2.1.

$$U(x,y,z,t) = \bar{U}(x,y,z) + u(x,y,z,t) \quad (2.1)$$

Knowledge of both the mean wind velocity and the fluctuating component assists in evaluating wind loads on the transmission line conductors. The mean wind velocity, wind profile, turbulence intensity, and gust spectra are presented as part of this sub-section.

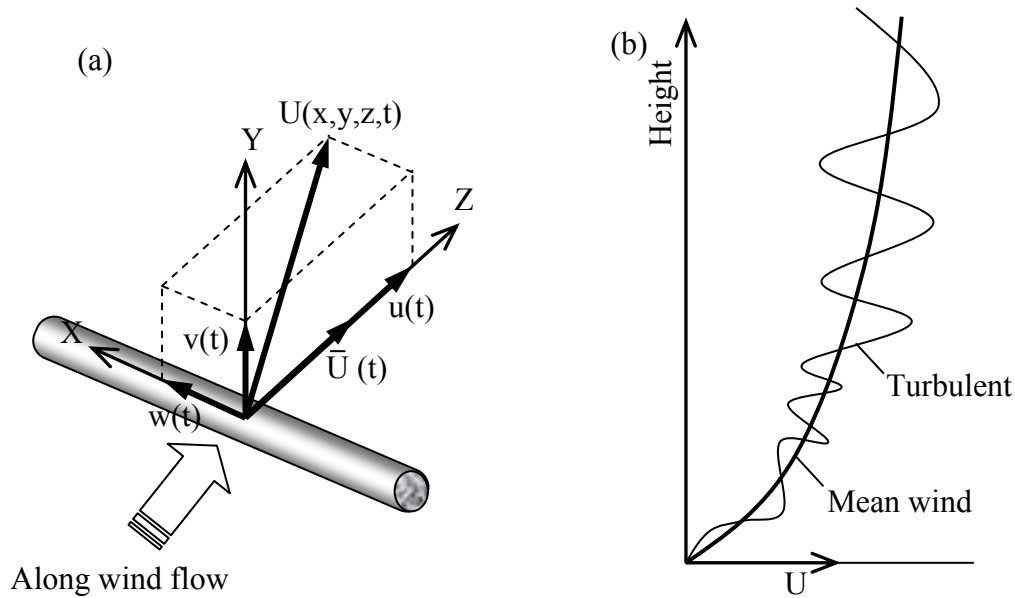


**Fig.2.1:** (a) The wind field model and (b) turbulence profiles

Mean wind velocity is defined as an average wind velocity for a specified time interval. The numerical value of the mean wind velocity can have large variations depending on the interval used for averaging the wind velocity. A shorter averaging time leads to a higher mean wind velocity value, while a longer averaging time leads to a smaller mean wind velocity value. This is primarily due to short gusts of high wind

velocity that last for short periods. In this study, the wind velocities are averaged over record length of 10 minutes.

An important characteristic of wind is the variation of wind velocity with height. The surface friction effects of the ground retard the movement of air close to the ground surface. This retardation causes a reduction in wind velocity near the ground. At some height above the ground, the movement of air is independent of the ground obstructions. This unobstructed wind velocity is termed the 'gradient wind velocity,' and the corresponding height at which the air movement is not retarded is termed the 'gradient height.' Mean wind profiles near ground level are currently represented by either power-law or logarithmic-law profiles.

Davenport (1960) introduced power-law of mean wind profile as follows

$$\frac{\bar{U}(z)}{\bar{U}_g} = \left( \frac{z}{z_g} \right)^\alpha \quad (2.2)$$

where  $\bar{U}(z)$  is mean wind velocity at height  $z$ ;  $\bar{U}_g$  is mean wind velocity at gradient height  $z_g$ ;  $\alpha$  is power-law exponent.

Simiu (1984) introduced logarithmic-law of mean wind profile based on the assumption of physical phenomena and is valid particularly up to 30 m above ground as follows

$$U(z) = \frac{1}{k} u^* \ln \left( \frac{z}{z_0} \right) \quad (2.3)$$

where  $k$  is scale factor ( $k=0.4$ ).  $(u^*)^2 = \frac{\sigma_u^2}{\beta_u}$ ;  $\beta_u = 4.4 \div 8.4$ .

#### *b. Turbulence intensity*

The fluctuating part of wind is termed as the turbulence. The turbulence presented in the wind flow is due to the ground roughness characteristics of the terrain over which it is passing or due to thermally induced convection or both. The turbulence

due to ground roughness is known as mechanical turbulence and that due to heat convection is known as convective turbulence.

Simiu (1985) presented that depending on the relative importance of convective to mechanical turbulence, the stability conditions of the atmosphere are classified as stable, neutral, and unstable.

The longitudinal  $u(t)$ , vertical turbulent components  $v(t)$  are considered as two multi-variate spatially correlated Gaussian random turbulent processes with zero mean (lateral turbulent component  $w(t)$  is omitted due to very small effect to structure). The turbulent fields at  $N$  discrete nodes are expressed as follows.

$$\begin{aligned} u(t) &= \{u_1(t), u_2(t), \dots, u_N(t)\}^T \\ v(t) &= \{v_1(t), v_2(t), \dots, v_N(t)\}^T \end{aligned} \quad (2.4)$$

The turbulence intensity is a measurement of the gustiness of the wind and expressed as follows

$$I_{uv} = \frac{\sigma_{uv}}{\bar{U}} \quad (2.5)$$

where  $I$  is turbulence intensity,  $\sigma$  is RMS of wind velocity fluctuations, and  $\bar{U}$  is mean wind velocity.

In the statistical terminology, this number is often called the coefficient of variation. Turbulence intensities are higher for records, which have lower mean wind velocities than for records that have high wind velocities for the same terrain. The turbulence intensity is strongly related to the terrain roughness; a greater turbulence is caused by a rougher terrain. A decrease in turbulence intensity with height is also expected.

Jan (1982) pointed out that at greater heights both mean and RMS values of wind velocity increase but the RMS value increases less because the shearing action of the ground surface is less.

Twu (1983) and GAI (1981) conducted parametric study of the Davenport analytical model and shows that the turbulence intensity is the influential parameter in predicting the response of the transmission line structure to extreme wind.

*c. Power spectral density*

A randomly fluctuating phenomenon such as wind velocity can be conceived of as the superposition of a large number of harmonic fluctuations with frequencies ranging from zero to infinity. The spectral representation of turbulence is related to this concept, and it provides information on the contributions of fluctuating components (energy) with various frequencies. The energy of any random process, like wind, is usually expressed in terms of a quantity called the 'Power Spectral Density (PSD).' The PSD at any particular frequency,  $f$ , may be considered as the average fluctuating wind power passing a fixed point when the wind as a random process is filtered by a narrow band filter centered at  $f$ . In this study, PSDs of vibration data is obtained by Fast Fourier Transform (FFT) analysis.

Simiu (1985) pointed out that in the dynamic analysis of structures subjected to gust loading, significant dynamic amplification of the response may occur at a resonant frequency, i.e., when the natural frequencies of vibration of the structure and of the wind match. Flexible structures like conductors can have dynamic amplification of the response because the fluctuating component of wind has a fair amount of power at frequencies of structural vibration. Therefore, peak response in PSD can be used to compare with analytical natural frequency of the transmission lines.

In some cases, without field-recorded wind velocity or in time-domain gust response analysis, empirical PSD is very usable. Many empirical formulae can be applied for simulating the longitudinal turbulence  $u(t)$  and the vertical one  $w(t)$ . Von Karman (1948) firstly introduced a practical empirical formula of the auto power spectral density based on ongoing turbulent flow conditions such as mean velocity, intensities of turbulence, length scale of turbulence and so on. So far, some authors to develop their empirical formulae have exploited von Karman method. Some empirical formulae are widely used for the auto PSDs of  $u$ -turbulence,  $w$ -turbulence,  $S_u(n)$  and  $S_w(n)$ , in the practical application introduced hereafter.

Kaimal & Panofsky' spectra:

$$\begin{aligned} S_u(f) &= \frac{200nu_*^2}{f(1+50n)^{5/3}} \\ S_v(f) &= \frac{3.36nu_*^2}{f(1+10n)^{5/3}} \end{aligned} \quad (2.6)$$

where  $n = \frac{fz}{U}$  is non-dimensional coordinates; f is frequency variable (Hz); U, z are mean velocity (m/s) and altitude z (m), respectively;  $u_* = \frac{kU}{\ln(z/z_0)}$  is friction or shear velocity (m/s); k,  $z_0$  are scale factor and roughness length (m).

Von Karman's spectra:

$$\begin{aligned} S_u(f) &= \frac{4\sigma_u^2 L_{ux} / U}{[1 + 70.78(fL_{ux} / U)^2]^{5/6}} \\ S_v(f) &= \frac{(2\sigma_v^2 L_{vx} / U)[1 + 188.8(fL_{vx} / U)^2]}{[1 + 70.78(fL_{vx} / U)^2]^{11/6}} \end{aligned} \quad (2.7)$$

where  $\sigma_u, \sigma_v$  are standard derivatives;  $L_{ux}, L_{vx}$  are chord-wise length scales of u-turbulences and v-turbulences.

### 2.1.3. Characteristic of vibration response

#### a. Peak vibration response

Peak vibration response, rather than a mean response value, is needed in designing and health monitoring. Peak response is predicted by the summation of mean and fluctuating responses as shown in Eq. (2.8).

$$\hat{R} = \bar{R} + g \cdot \sigma_R \quad (2.8)$$

where  $\hat{R}$  is peak response;  $\bar{R}$  is mean response;  $\sigma_R$  is RMS of the fluctuating response;  $g$  = statistical peak factor

In equation (2.8), the mean response of conductors is obtained from the mean wind pressure acting at the effective height of the conductors as shown in Eq. (2.9). In most cases, the force coefficient is determined from wind tunnel tests and, in general, it is a function of Reynolds Number, the angle of incidence of the wind, and the shape and roughness of the conductor. The fluctuating response is a product of peak factor and RMS value of response. The dimensionless peak factor,  $g$ , is probabilistic because of the random nature of the fluctuating response. In current studies, maximum peak-to-peak is taken into account to avoid accident due to phase-to-phase flashovers that can lead to short circuit, etc.

$$\bar{P} = \frac{l}{2} \rho \bar{U}^2 C_f \quad (2.9)$$

where  $\rho$  is air density;  $\bar{U}$  is mean wind velocity;  $C_f$  is force coefficient.

*b. Root Mean Square of response (RMS)*

To determine the response of a conductor subjected to fluctuating wind, frequency domain methods are usually used. Frequency domain methods are popular for computation because they are cost effective and efficient. In frequency domain analysis, fluctuations in the wind and conductor response are represented by a spectrum. A spectrum is a plot of energy at each frequency versus the frequency. Therefore, it represents a distribution of energy over the entire frequency range. The area under the spectrum is equal to the mean square value of the fluctuations. Spectral analysis is conducted to investigate the time average characteristics of wind-induced responses in frequency domain.

*c. Maximum peak-to-peak amplitude (MPPA)*

Maximum peak-to-peak amplitude also is very important to structural health monitoring as well as designing for the transmission lines. In order to understand the general characteristics of the field vibration, maximum peak-to-peak amplitude (MPPA) and time history of dynamic response should be considered. It is usable to interpret the cause of damages due to MPPA events as observed in the field by TEPCO. In other hand, understanding of MPPAs versus mean wind velocity can easily to confirm whether the field vibration data is gust response or not. Knowing that, increasing tendency of MPPA in parabolic fashions with the increase of mean wind velocity is the characteristics of gust responses.

## **2.2. Full-scale measurement**

### *2.2.1. Outline of the transmission line systems*

In this section, the three long-spans bundled-conductor electrical-power transmission line systems (so-called Line A, Line B, and Line C) with the equipments for the field measurement are considered. Figure 2.2 shows the geometries of Line A for example with the instrumentation for the field measurement.

Line A has eight bundled-conductors in a single dead-end span of 615 m between two anchoring towers No. 58 and No. 59 with 40 m difference in their levels. Line B has four bundled-conductors in two spans: 624 m long span between the towers No. 3 and No. 4, and 407 m long span between the towers No. 4 and No. 5. The level differences of two anchoring points in the first and second spans are 137 m and 51.6 m, respectively. The two spans are not aligned having an acute angle of  $8^{\circ}58'$  as shown in Fig. 2.2(b). It should be noted that conductor is anchored to the intermediate tower in

Line B and freely in the jumper's pipe. The vibration of the transmission line could affect the dynamic characteristics of the jumper.

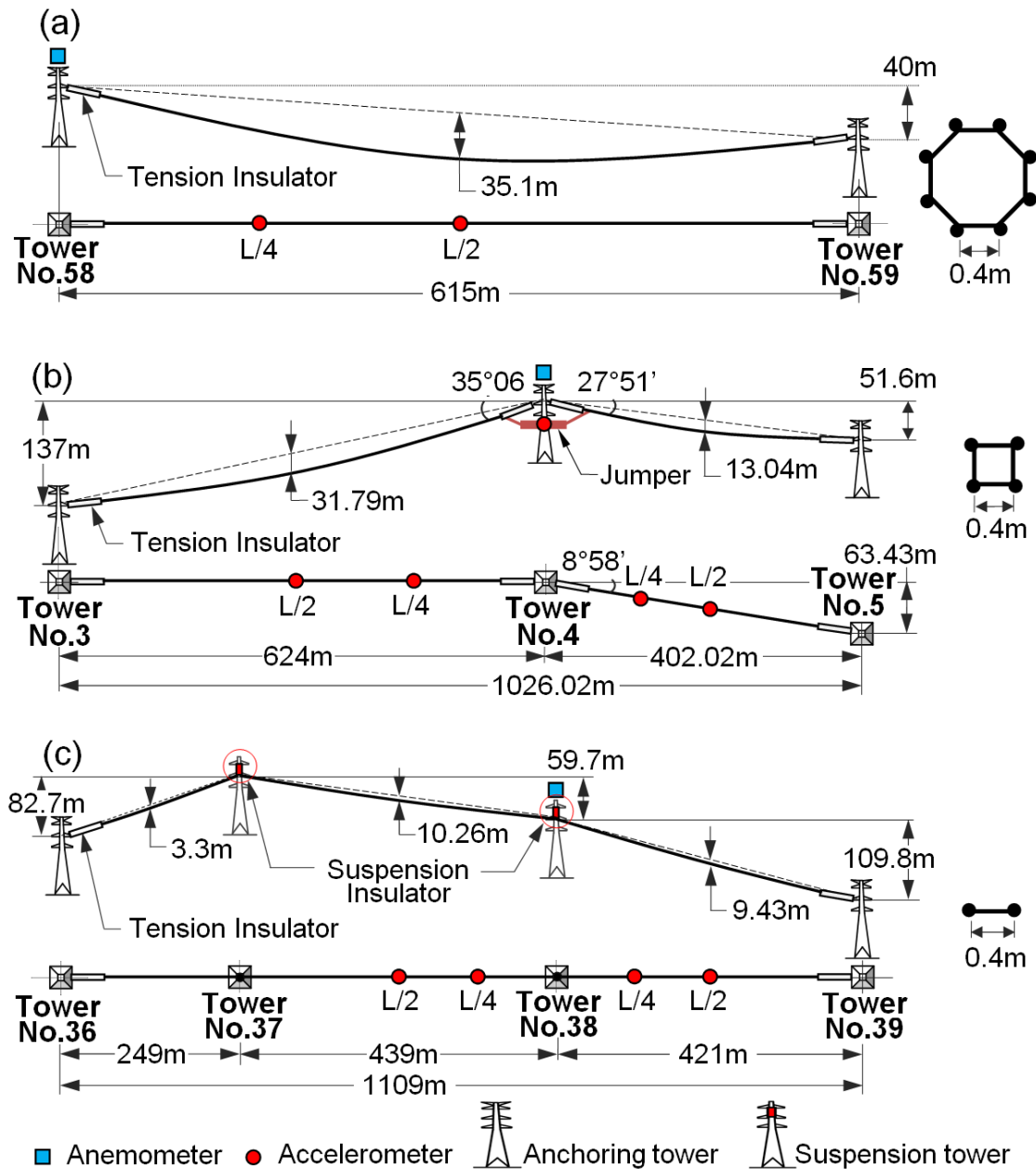


**Fig. 2.2:** Geometries of the transmission lines and cross sections of bundled-conductors: (a) Line A; (b) Line B; and (c) Line C.

Line C has two bundled-conductors in three spans: 249 m long span between the towers No. 36 and No. 37, 439 m long span between the towers No. 37 and No. 38, and 421 m long span between the towers No. 38 and No. 39. The level differences of anchoring/suspending points in the first, second and third spans are 82.7 m, 59.7 m and

109.8 m, respectively. In Line C, suspension type insulators are used for the intermediate towers. The specification of lines A, B, and C is given in Table 2.1.

In detail, the transmission line system is made of bundle-conductor connected to suspension and/or anchoring towers. There are two types of insulators in the three transmission line systems, tension insulators and suspension insulator. Bundled-conductors are attached to anchoring tower by tension insulators and to suspension tower by suspension insulator. In bundle-conductors, spacers along span arrange the cables separately. Spacers maintain the distance between two phases to avoid short-circuit of different phases. Connection assembly of spacer and insulators to conductors is complicated and significantly affect torsional stiffness of bundled-conductors. In Line B, jumpers are arranged to impose sub-conductors jumping through towers from this side to other side of tower.

Table 2.1 Geometrical description of Line A, B and C.

		Line A	Line B	Line C
Lines	No. of conductor	8	4	2
	No. of span	1	2	3
	Span length (m)	615	624/402.02	249/439/421
	Sag to span ratio	0.057	0.051/0.032	0.013/0.023/0.022
Conductor	E (N/m <sup>2</sup> )	69.9e9	90.6e9	90.6e9
	Weight (kg/m)	3.056	1.11	1.328
	Diameter (mm)	40.3	22.4	24.5
	Spacing (m)	0.4	0.4	0.4
Spacer	Weight (kg)	28	9.5	27
	E (N/m <sup>2</sup> )	210e9	210e9	210e9
	Length (m)	13.905	7.43	3.6
Tension insulator	Weight(kg)	14330	4076	275
	E (N/m <sup>2</sup> )	210e9	210e9	210e9

Suspension insulator	Length (m)	3.5
	Weight(kg)	290
	E (N/m <sup>2</sup> )	210e9
Jumper pipe	Diameter (mm)	120
	E (N/m <sup>2</sup> )	63e9
Jumper hanger	Diameter (mm)	40
	E (N/m <sup>2</sup> )	210e9

### 2.2.2. Field measurement

The measurement data used in the present study are all the full-scale measured vibration events with wind data from December 2008 to July 2009. It should be noted that the wireless sensor that was developed by TEPCO was mounted on the spacer frame of conductor bundle to measure the vibration acceleration of conductor bundle in three directions. The wind and acceleration measurements are synchronized for real time but different sampling frequencies/different trigger level for each type of data. The wind velocity data was recorded continuously for four months. Therefore, 10-minute length wind records corresponding to each 10-minute length acceleration data can be extracted appropriately from the continuous wind velocity data, in which 10-minute length wind record is commonly assumed stationary in practice. The summary of field measurement is given in Table 2.2 indicating the numbers of datasets of all the measured vibration events and the vibration events with wind data.

The main advantage of testing under natural field condition is that it is realistic. However, responses observed in such tests are usually somewhat complicated than those observed in laboratory environment. Therefore, interpretation of such response is difficult and sometimes it may not depend on theoretical assumptions about which even experts may disagree.

The accelerations in all three translational directions and the angular velocity were measured by using accelerometers and angular velocimeters, respectively, at the quarter and mid spans as shown in Fig. 2.2. In the case of Line B, in addition, the motions of jumper pipe are measured by the accelerometer located at its midpoint. The sampling frequency of each record is 10 Hz and the record length is 10 minutes. For the measurement of wind velocity, a three dimensional ultrasonic anemometer was placed at the top of tower in the each transmission line with the sampling frequency of 50 Hz.

Table 2.2 Number of field data sets from Dec. 2008 to July 2009.

Lines	Datasets	Left Span			Right Span	
		L/2	3L/4	Jumper	L/4	L/2
Line A	All vibration data	-	-	-	44	191
	Vibration with wind data	-	-	-	44	191
Line B	All vibration data	104	220	121	137	157
	Vibration with wind data	88	166	116	135	152
Line C	All vibration data	10	61	-	52	1
	Vibration with wind data	4	22	-	27	1

### 2.3. Discussion on field-measured wind velocity

#### 2.3.1. Wind direction and mean wind velocity

Figure 2.3 shows the variation in the direction and the magnitude of mean wind velocity during the measured vibrations along with the alignment of Line A for example. The direction of mean wind velocity is not normal to the transmission line and the

variation in wind direction is large especially in the case of Line B. This indicates the importance of skew correction for further discussions calculating the component of mean wind velocity normal to the transmission line.

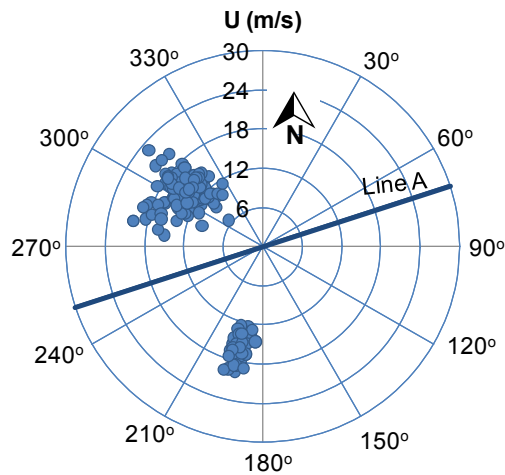


**Fig. 2.3:** Direction and magnitude of mean wind velocity of Line A (refer Hung et al. 2014 for Line B and C).

2.3.2. *Turbulence intensities*

The longitudinal  $u(t)$ , vertical turbulent components  $w(t)$  are calculated by using Eq. (2.5). For example, the magnitude of turbulence intensity of Line A is plotted with respect to the normal component of mean wind velocity in Fig. 2.4. All the transmission lines are located on mountainous terrain and therefore the turbulence intensities are relatively high especially in the case of Line B.

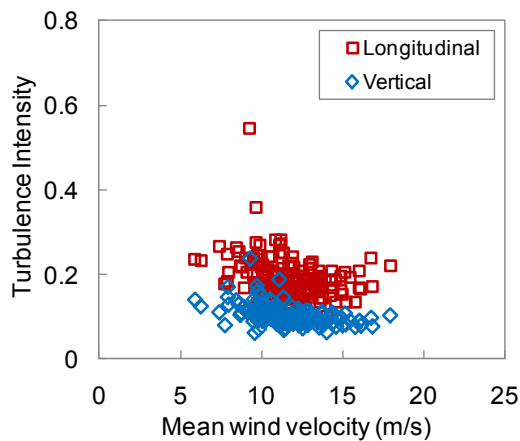


**Fig. 2.4:** Turbulence intensity of wind versus normal component of mean wind velocity of Line A (refer Hung et al. 2014 for Line B and C).

Turbulence intensities of longitudinal wind velocity fluctuations are greater than 0.15 with maximum, minimum, and average values as 0.544, 0.101, and 0.190 respectively. Maximum, minimum, and average values of turbulence intensities for vertical wind fluctuations are 0.237, 0.062, and 0.104 respectively. These turbulence intensities as supposed to be higher than normal. For Line B, an overview of turbulence intensities show higher turbulence intensities as compared to the turbulence intensities in case of Line A. Turbulence intensities in case of Line B are as high as 0.7 for longitudinal and 0.45 for vertical wind velocity fluctuations. It is confirmed in the figure that the turbulence intensity decreases with the crease of mean wind velocity and that the vertical component is almost one-half of the horizontal one. Both the high turbulence intensities and the skew of wind direction could preclude the possibility of vortex formation or aerodynamic effect of one conductor on the other in the bundled-conductors.

#### **2.4. Identification of field-measured vibration responses**

The acceleration records are integrated numerically twice to obtained displacement records. Before each integration step, the data is high pass filtered to remove erroneous low frequency components. Cut-off frequency of the filter is set to be half of the first natural frequency or 0.1 Hz less than the natural frequency if record has low frequency component (Liu, 2005). However in case of the transmission line low frequency component may be important and erroneous part of the low frequency component is impossible identify. So in order to adjust the cut off frequency and obtain meaningful displacements through integration, TEPCO carried out additional measurements. In these additional measurements, displacements are measured directly by charge-coupled device (CCD) camera. Integration schemes with high pass filters of different cut off frequencies are applied to acceleration records to obtain displacement records, which are then compared to displacement records obtained directly through CCD camera. The integration scheme that gives best agreement is finally utilized.

2.4.1. Identification of peak response in PSDs

Spectral analysis is conducted to investigate the time average characteristics of wind-induced responses in frequency domain as well as to obtain RMS of response and compare with eigenvalue analysis. In the following, for example, PSD of all measured points of the three transmission lines are shown. PSDs of selected data are shown in Fig. 2. (5-7) will be employed in further discussion in Chapter 3 and 4.

For example, in the case of Line A, at mid-point measurement, there is some dominant peak of frequency as shown in Fig. 2.5 at 0.1 Hz in horizontal spectra, 0.2 Hz in vertical spectra, and 0.3Hz in torsional spectrum. In the case of Line B, at jumper measurement shown in Fig. 2.6 (c), power density is smaller than other span power density. There is a dominant peak of frequency at 0.35 Hz at both horizontal and torsional spectra. In span-spectra of Line B, very large field-vibration amplitudes are observed in 407 m span. As its spectrum shown in Fig. 2.6 (d, e), there are dominant peaks of frequency at 0.15 Hz in horizontal spectrum, at 0.35 Hz in torsional spectrum. This characteristic will be discussed more in interesting phenomena of Line B in Chapter 3.

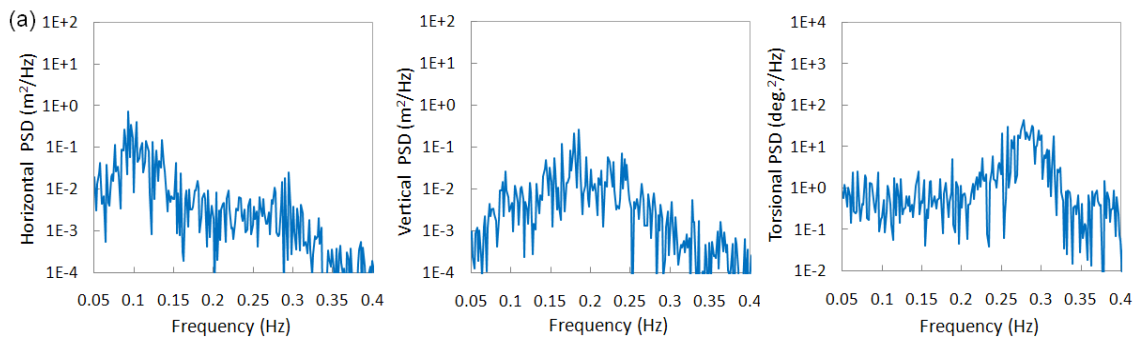


**Fig. 2.5:** PSDs of large amplitude vibrations in Line A at L/2 span.

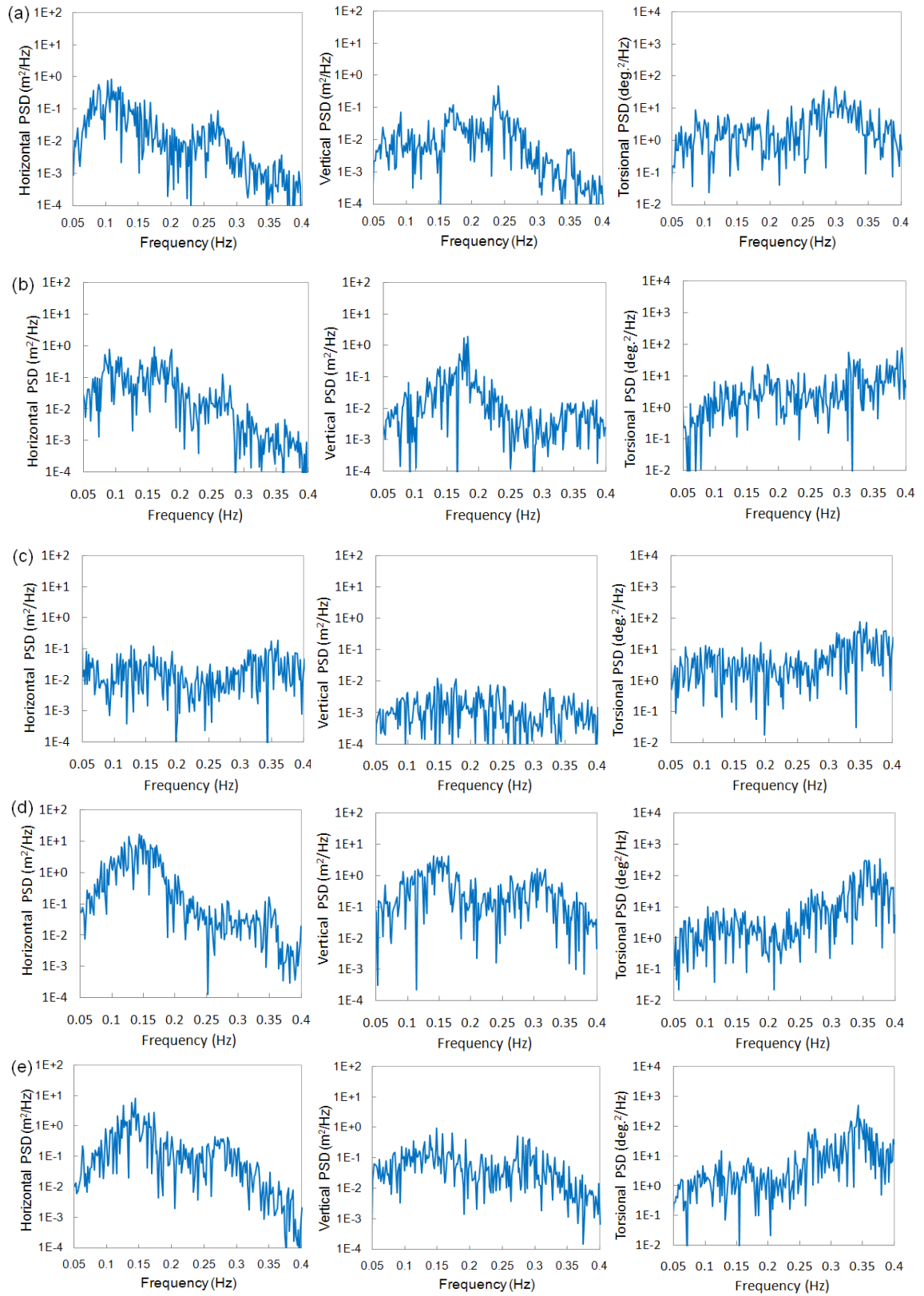


**Fig. 2.6:** PSDs of large amplitude vibrations in Line B: (a) L/2 624m span; (b) L/4 624 m span; (c) jumper; (d) L/2 407 m span; and (e) L/4 407 m span.

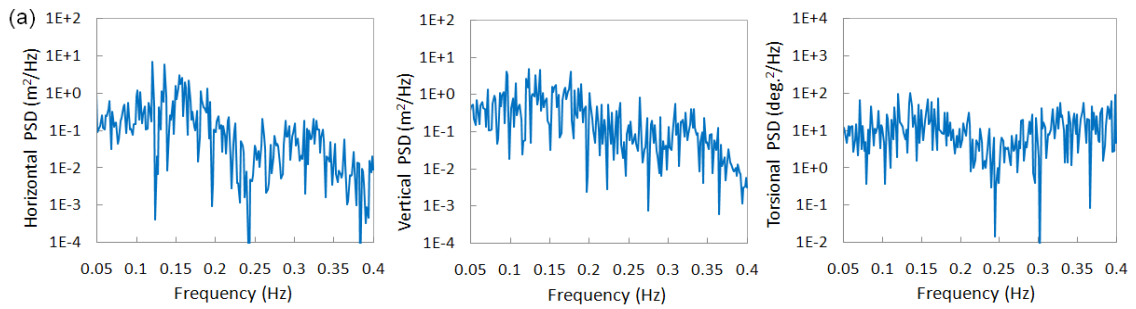


**Fig. 2.7:** PSDs of large amplitude vibrations in Line C at L/2 span

#### 2.4.2. Discussion on RMS of field-measured response

The RMS of horizontal, vertical, and torsional responses in Line A are plotted with respect to the normal component of mean wind velocity in Fig. 2.8. It is noted that the RMS responses appeared correlative with the normal-wind component. As shown in the figure, the trend of RMS response versus the normal component of wind is parabolic in almost all the cases except for the vertical vibration of Line C. While there might be a possibility of aerodynamically unstable phenomena, it is difficult to ascertain the type or the mechanism of vibration in Line C with small number of data. It is also understood that the RMS responses of Line B are larger and more scattered than that of either Line A or Line C, which is mainly due to the difference in both the magnitude and dispersion of turbulence intensity of wind. Except for Line C, furthermore, the horizontal responses are larger than the vertical responses, which is partly because the turbulence intensities in the horizontal direction are higher than that in the vertical direction. Almost all the above discussions on RMS response characteristics suggest that most of the field-measured responses could be gust responses. As for the differences in the RMS values for different measure points, those are very much related with the dominant modes in the wind-induced responses, which will be discussed later.

#### 2.4.3. Discussion on MPPA of field-measured response

Figure 2.9 shows the variation of MPPA with respect to the normal component of wind velocity for Line B, as an example, which has the largest MPPA among three transmission lines. The parabolic trend of MPPA in the figure is almost similar to the trend of RMS response, which is also one of the characteristics of gust response, as the peak response can be obtained by multiplying the RMS response by a peak factor. The maximum values of MPPAs for three lines are summarized in Table 2.3. While the RMS responses are relatively small for Line A and Line C, their maximum MPPAs are large enough up to 1.62 m and 4.48 m, respectively. One event shows very large responses with horizontal, vertical, and torsional MPPAs of 7.65 m, 4.83 m and 71.0 degree, respectively, at the middle point of 407 m span of Line B. This kind of event should be carefully identified as a gust response or a galloping in further analysis. It is noted that the large horizontal MPPA of 1.65 m at the midpoint of jumper is observed, which can induce some damage in the jumper line. The mechanism of this jumper vibration will be discussed later in relation to jumper.

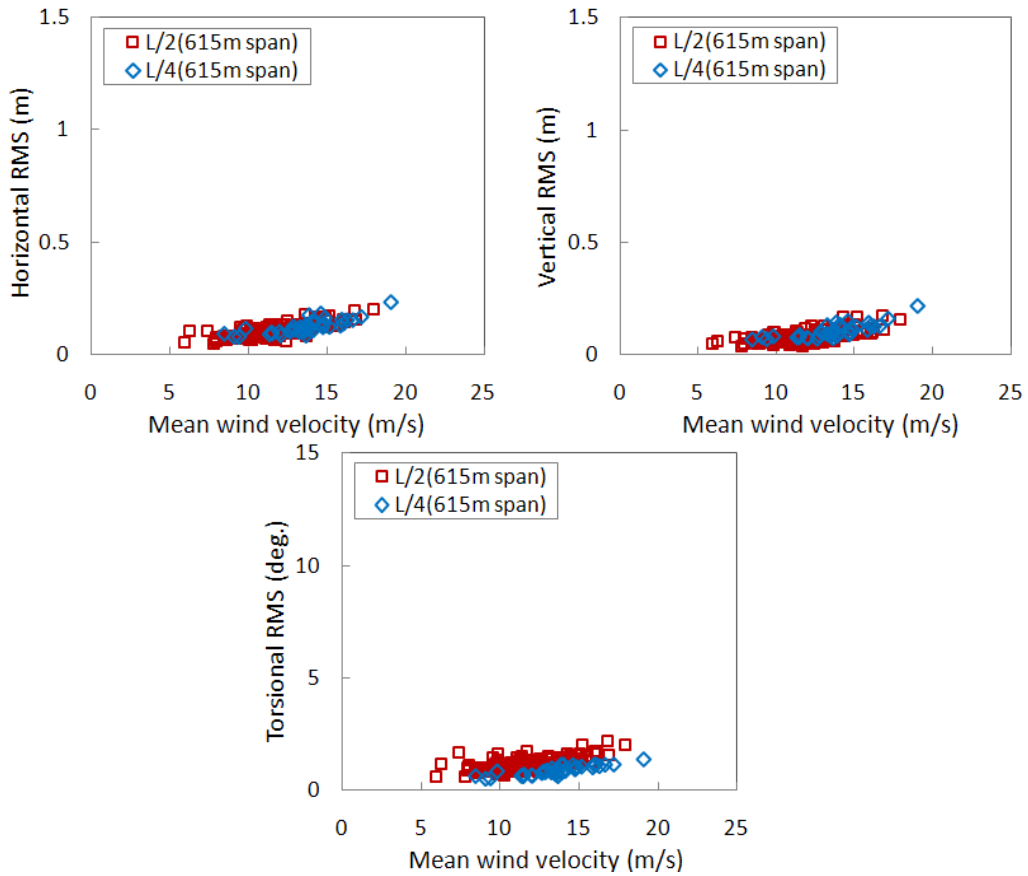


**Fig. 2.8:** RMS response versus normal component of mean wind velocity of Line A (refer Hung et al. 2014 for Line B and C).

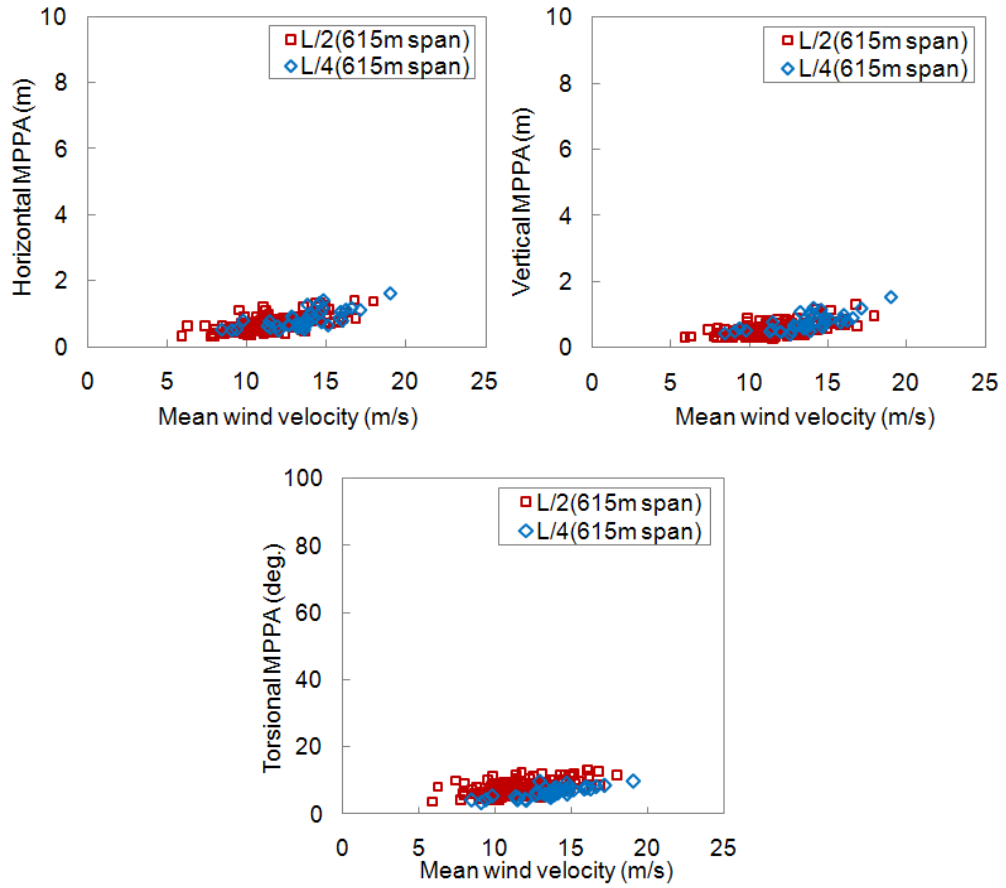


**Fig. 2.9:** MPPA response versus normal mean wind velocity for Line A (refer Hung et al. 2014 for Line B and C).

Table 2.3 Maximum of MPPAs of Line A, Line B, and Line C.

Lines	Span	Measured point	Horizon (m)	Vertical (m)	Torsion (deg.)
Line A		L/2	1.42	1.29	13.2
		L/4	1.62	1.53	9.81
Line B	Left	L/2	4.62	3.40	31.4
		3L/4	3.44	3.74	26.3
	Jumper	L/2	1.65	0.42	33.9
	Right	L/4	5.86	3.98	37.7

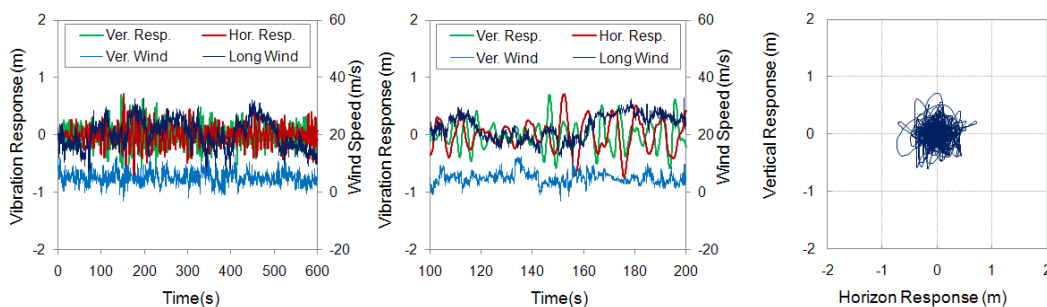
		L/2	7.65	4.83	71.0
Line C	Left	L/2	2.36	2.38	20.1
		3L/4	1.31	3.39	16.9
		Right	L/4	2.54	2.24
		L/2	2.97	1.99	20.7

#### 2.4.4. Time series based identification

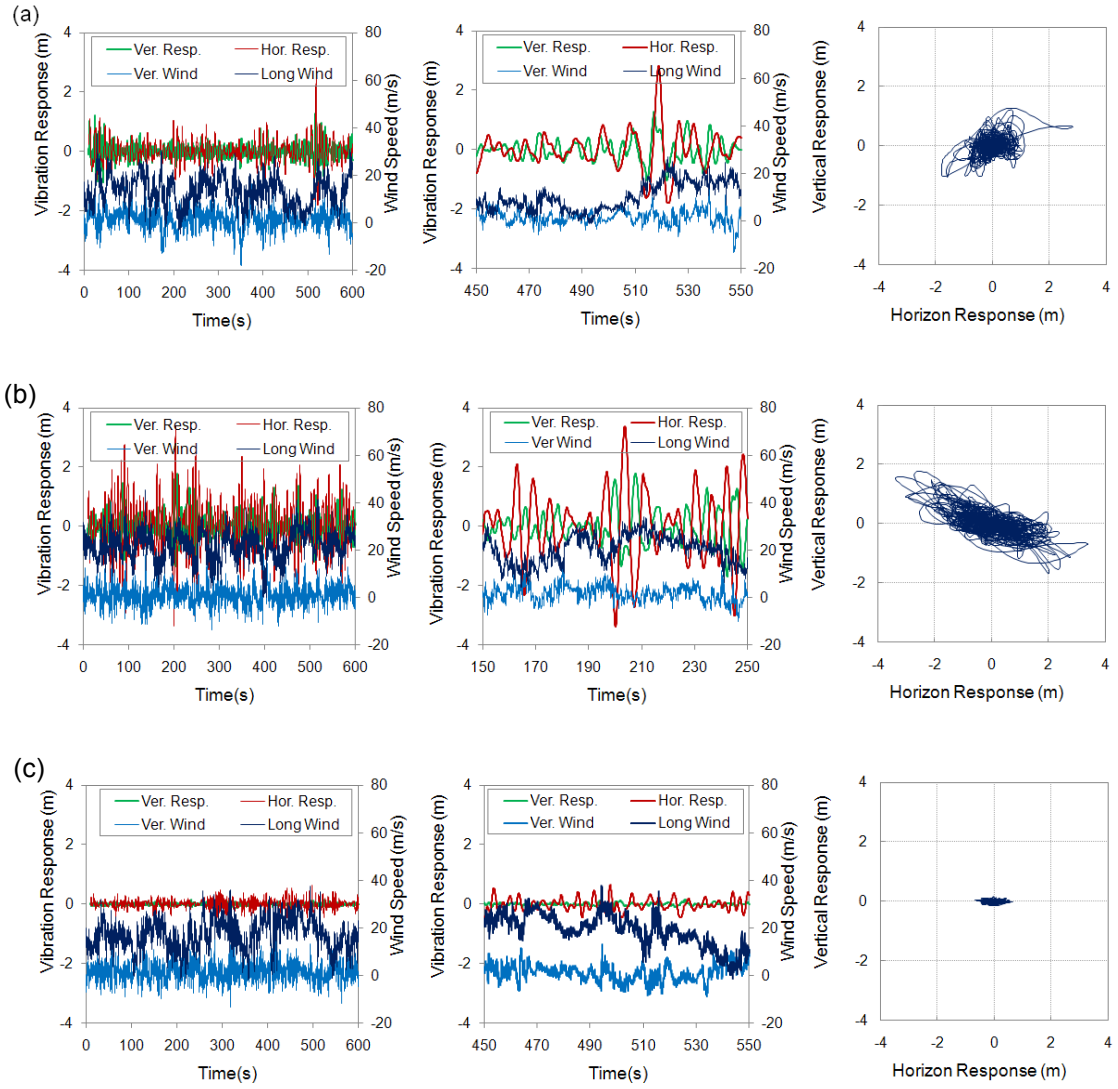
In order to understand further the nature of large vibrations discussed, it is important to show time series of these vibrations and compared them with corresponding time series of wind velocity.

In case of galloping, responses develop gradually due to negative aerodynamic damping. Opposite is the case of gust response in which response builds suddenly within very short time period and do not have gradually building cycles before appearance of peak cycle. Almost horizontal, vertical, and torsional responses appear suddenly and are not gradually developed Moreover every sudden peak is accompanied by a sudden change in wind velocity. Impulsive nature of these peaks indicates the possibility that observed vibrations are gust response.

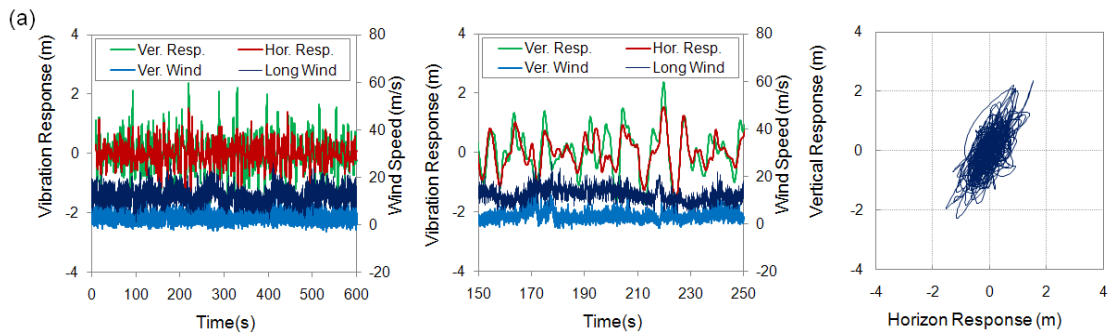
The time history of typical events in Figure 2.(10-12) again confirm that, different from galloping response, the LAGs appear with the peak responses increasing suddenly within very short period of time corresponding to the increases of wind velocities.



**Fig. 2.10:** Time series of Line A at L/2.



**Fig. 2.11:** Time series of Line B: (a) L/2 624 m span; (b) L/2 407 m span, (c) jumper.



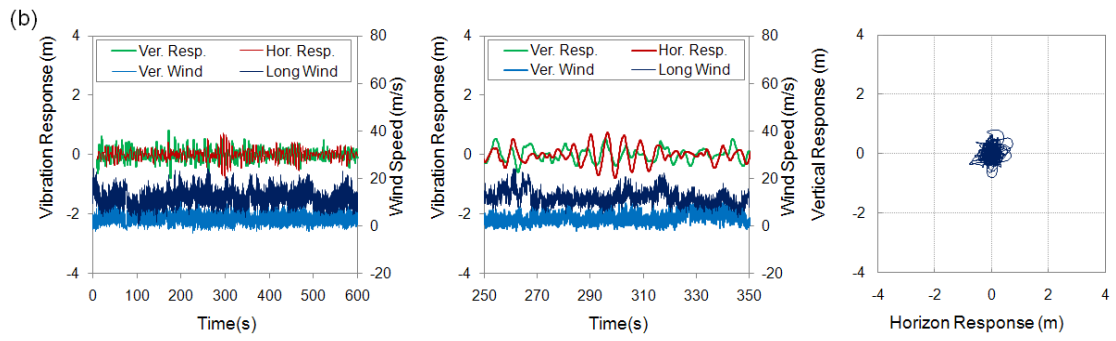


**Fig. 2.12:** Time series of Line C: (a) L/4 439 m span; (b) L/4 421 m span.

## 2.5. Conclusions

In this chapter, an outline of the field measurement is conducted firstly. The preliminary interpretation of the field-measured wind velocity and vibration response is discussed. In detail, some conclusions can be conducted as follows.

The number of the field-measured datasets is a sufficient large for the identification of the essential characteristics of the stochastic processes as the natural wind turbulence and the random vibration of the transmission lines.

The direction of the mean wind velocity is not normal to the transmission line conductors. Therefore, in the all of comparisons, the normal component of the mean wind velocity is taken into account.

Almost of the field-measured vibrations of the conductors in the gusty wind have large amplitude, especially in the case of Line B. The dominant frequencies that were shown clearly in the PSDs may make identification of characteristics of the transmission lines more easily.

Based on the data analyses about RMS, MPPA, the time series of large amplitude, the large-amplitude field-measured vibration intends to follow the gust characteristics.

**References**

- Yamaguchi H, Xie X, Yukino T, (1995). Galloping analysis of transmission lines with bundled-conductors. In: Proceeding of International Seminar on Cable Dynamics, Liege (Belgium), pp. 61–6.
- CIGRE, (2005). “State of the Art of Conductor Galloping.” Technical Brochure 322. Task Force B2.11.06.
- Gull JH, Yamaguchi H, Kumagai K, Hung PV, (2011). Interpretation of field-measured vibrations in transmission lines by gust response analysis. In: Proceedings of 9th International Symposium on Cable Dynamics, Shanghai (China), pp. 281-286.
- Zuo, D., & Jones, N. P. (2009). Interpretation of field observation of wind- and rain-wind-induced stay cable vibrations. *J. Wind Eng. and Industrial Aerodynamics*.
- Macdonald, J. H. (2003). Evaluation of buffeting predictions of a cable-stayed bridge from full-scale measurements. *Journal of Wind Engineering* , pp. 1465–1483.
- Solari, G.; Carassale, L. (2000), “Modal transformation tools in structural dynamics and wind engineering”, *Wind & Structures*, 3(4), pp. 221-241.
- Davenport, A.G. (1962), “Buffeting of a suspension bridge by storm winds”, *J. Struct. Div., ASCE* 88(3), pp. 233-268.
- Simiu, E., and Scanlan, R.H., (1985): "Wind Effects on Structures: An Introduction to Wind Engineering," John Wiley and Sons, Inc., New York, NY.
- Jan, Con-Lin, (1982): "Analysis of Data for the Response of Full-Scale Transmission Tower Systems Real Winds," Masters thesis, Texas Tech Univ.
- Twu, S.R., (1983): "Gust Response Factor for Transmission Line Structures," Masters Thesis, Texas Tech University, Lubbock, Texas, August.
- Liu M.Y., Z. D. (2005). Deck induced stay cable vibrations: field observations and analytical model. Sixth International Symposium on Cable Dynamics, (pp. 175-182). Charleston, SC, USA.
- Hung, PV., Yamaguchi, H., Isozaki, M., Gull, JH, (2014). Large amplitude vibrations of long-span transmission lines with bundled conductors in gusty wind. *J. Wind Eng. Ind. Aerodyn.* 126, 48–59

## CHAPTER 3

### CHARACTERIZATION OF RESPONSES WITH

### EIGENVALUE ANALYSIS

---

1. Static equilibrium configuration
  2. FE models of the transmission line system
  3. Natural frequencies and mode shapes
  4. Interpretation of characteristics of field-measured vibration
  5. Conclusions
  6. References
- 

In order to evaluate the dynamic characteristics of the transmission line systems and identify the modal parameters from the field-measured data, the eigenvalue analysis is performed. The results of eigenvalue analysis, in which the proper FE models of the transmission lines with their accurate static-equilibrium-configurations play an important role not only are used to interpret the field-observed vibrations but also are used in a conjunction with the wind-force model to conduct the gust response analysis. The FE models of the transmission lines are created and analyzed by using the general-purpose computing program FEMAP/NX Nastran.

#### **3.1. Static equilibrium configuration**

### 3.1.1. Introduction

In creating the FE models of the transmission lines, the important part is to find out the appropriate static equilibrium configurations of the conductors subjected to the body loads.

Wilson and When (1974) assumed the cable to have a parabolic profile based on the consideration of the inclined cable subjected to the both cases of the concentrated load and a partial-uniformly-distributed load.

Irvine (1975) developed general solutions for the response of a horizontal-chord, free-hanging cable subjected to a point load and/or a distributed load. The solutions assumed that the profile of the cable is an elastic parabola and are limited to cables with sag to span ratios of less than (1:8).

Irvine and Sinclair (1976) produced non-dimensional equations that give an exact solution for an elastic cable hanging under self-weight with any number of vertical point loads. The solution provides an elastic catenary solution for the case of no concentrated loads. These solutions describe the exact theoretical static behavior of a flexible-linearly-elastic-guy wire having insulators spaced along its length.

Irvine (1981) published his well-known book *Cable Structures*, a comprehensive reference that documented the history and development of theoretical work in the field of mechanics of cables and cable structures. In his book, he included his own work as well as that of others accomplished prior to 1980. The book described many aspects of cable-related analyses, such as: exact and approximate equations describing the static behavior of suspended cables including both horizontal and inclined cables, and generalized equations for a cluster of guy wires considering both sag and elasticity effects.

Leonard (1988) published *Tension Structures: Behavior & Analysis*, a reference book that considers the subject of cable structures. His book is considered as an up-to-date, and has a wider-scope and better presentation than the previously published book by Irvine (1981). This reference emphasized the use of finite element analysis as the main technique used to solve the general problem of a cable/cable-structure subject to

different loading types. It introduced the characterization of tension structures including their definition, application, general aspects of behavior, and their construction materials. It also discussed the statics of cable segments and systems considering response to uniform and concentrated loads and three-dimensional behavior. The book described the finite element static analysis of cable networks, including the methodology, the development of cable elements and the nonlinear cable finite element analysis. Finally, it introduces both the linear and nonlinear behavior of membranes and explains the pre-stress effects on behavior of membranes of revolution.

Vallabhan (2000) introduced a new model describing the two-dimensional static equilibrium of a cable element when loaded by either uniform or concentrated loads. In his model, he used the least number of assumptions to derive the nonlinear differential equilibrium equation of the cable. To solve these equations, he used an efficient finite difference formulation combined with an iterative procedure. Later in the same year, he extended his work to three-dimensional cable statics problems, maintaining the same assumptions and using the same techniques.

### *3.1.2. Catenary theory based static equilibrium configuration of conductor*

As mentioned previously, catenary theory is popular solution for static equilibrium configuration of cable under its self-weight. Catenary equation can be obtained based on assumption of extensible or inextensible cable. Based on theory of inextensible or extensible catenary, the static equilibrium configuration of conductor in FE model of the transmission line system in FEMAP/NX Nastran computing software is derived and presented. Theory of static equilibrium configuration of in/extensible catenary equations is introduced in detail in Appendix - A.

The equation of in-extensible catenary curve can be given as follows.

$$z = \frac{H}{q_0} \cosh\left(\frac{q_0}{H} x + C_1\right) + C_2 \quad (3.1)$$

The equation of extensible catenary curve in  $z$  coordinate and  $x$  coordinate can be shown in Eq. (3.2) and Eq. (3.3), respectively, as follows.

$$z = \frac{1}{AE} \left( \frac{q_0 s_0^2}{2} - F s_0 \right) + \frac{1}{q_0} \sqrt{H^2 + (q_0 s_0 - F_3)^2} + C \quad (3.2)$$

$$x = \frac{H}{AE} s_0 + \frac{HL_0}{w} \cosh \left( \frac{q_0 s_0 - F_3}{H} \right) + C \quad (3.3)$$

where  $s_0$  is un-deformed length ( $s$ = Lagrangian coordinate);  $q_0$  is conductor weight per unit length;  $AE$  is axial stiffness of conductor;  $x$  and  $z$  are Cartesian coordinates;  $H$  is the constant horizontal component of cable tension.

### 3.1.3. Sag-to-span ratio

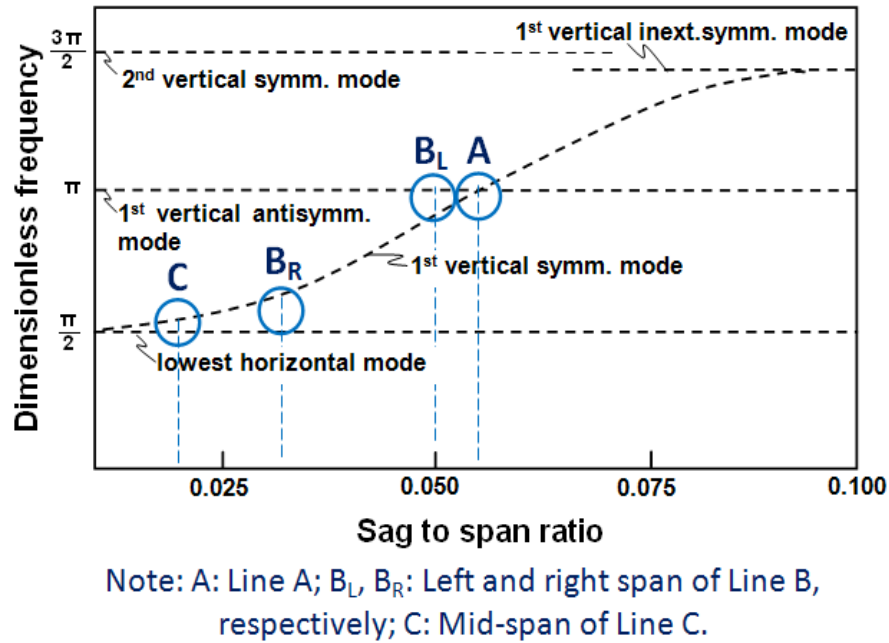


**Fig. 3.1:** Change in natural frequencies with respect to sag-to-span ratio and the position of Line A, B and C.

The sags in the FE models should be set equal to the field-measured sags of real conductors, because the sag-to-span ratio affects significantly on the natural frequencies of vertical symmetric modes as shown in Fig. 3.1 (Irvine, 1981).

In fact, in the cases of Line A and Line B, their sag-to-span ratios are located closely to so-called cross-over point where the natural frequencies of vertical symmetric and anti-symmetric modes coincides with each other, and slight errors in setting the sag-to-span ratios cause relatively large changes in the natural frequencies.

#### *3.1.4. Deriving static equilibrium configuration of conductor FE model*

In fact, given data in hand includes information of sag, material properties, and general geometries of the transmission lines without coordinate data of the real transmission line configuration. Therefore, we have to find out the coordinate of the real static transmission line configurations that impose appropriately the given sag (real sag or target sag). The well-known catenary could be the best solution to simulate the real conductor configuration coordinates. These simulated data with the given sag is considered as the real-cable coordinates or the so-called “real simulated data”. It’s should be noted that the “real coordinate data” can be the best-fitting data of real cable configuration but it cannot be coordinates of the target cable configuration of FE model due to pre-stiffening in modal analysis in computing software.

In order to derive the target conductor configuration of FE model, an alternative program will be proposed. In the procedure of deriving the target cable configuration of FE model, the “real coordinate data” is just considered as input coordinate data of initial configuration in beginning step of the alternative program. The initial configuration of cable can be arbitrary. Therefore, in the beginning step of the alternative program, it should freely select “the real coordinate data” to be the initial configuration. Therefore, “the real coordinate data” or the catenary theory calculated coordinate is considered as input coordinate data, not directly used as the FE target conductor configuration.

The static equilibrium configuration analysis associated with pre-stiffening of the transmission lines under their body loads for inducing the tension inside the conductors is a nonlinear problem, which is solved by an iterative algorithm employing the sag as a convergence controlled parameter as shown in Fig. 3.2. The iterative algorithm in this study is summarized in four steps. In the first step, inelastic catenary configurations are theoretically calculated as input data. Then the theory-based models

are analyzed by using the static nonlinear solution of FEMAP/NX Nastran to get the initial sag in the second step. In the third step, the difference between the current sag and real target sag is checked. If the error is within the convergence tolerance, then the calculation go to the fourth step, otherwise the calculation returns to the first step with modified sag. Finally, in the fourth step, the iteration program is stopped with proper transmission line configurations.

3.1.5. *Convergence criteria*

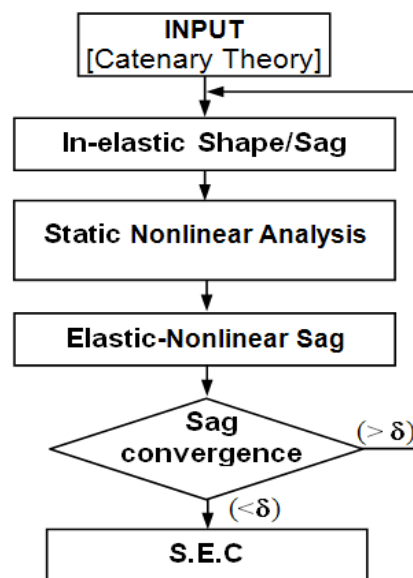


**Fig. 3.2:** Scheme of iterative algorithm.

The convergence of the solution can be based on two results, displacement, and energy. In a nonlinear analysis, a solution is considered to be converged when the displacement in the last iteration ( $\Delta d$ ) compared to the overall displacement ( $D$ ) is less than the convergence tolerance ( $\delta$ ) as in Eq. (3.4).

$$\Delta d/D < \delta \tag{3.4}$$

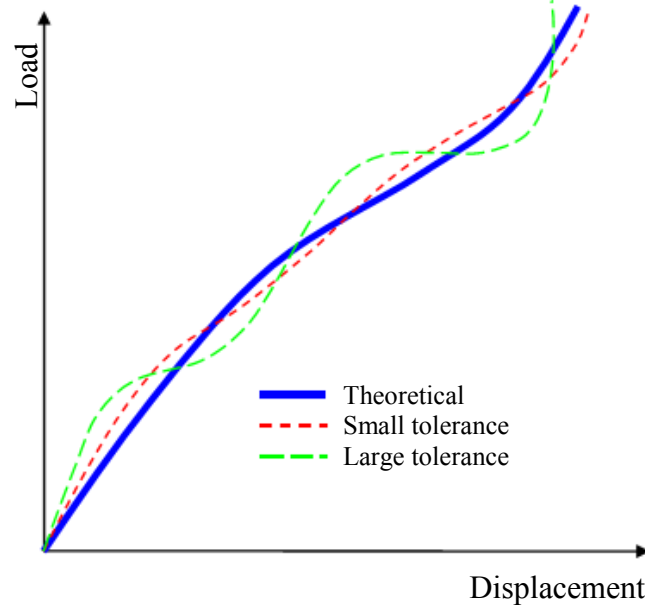


**Fig. 3.3:** Scheme of Effect of Tolerance Size on Solution

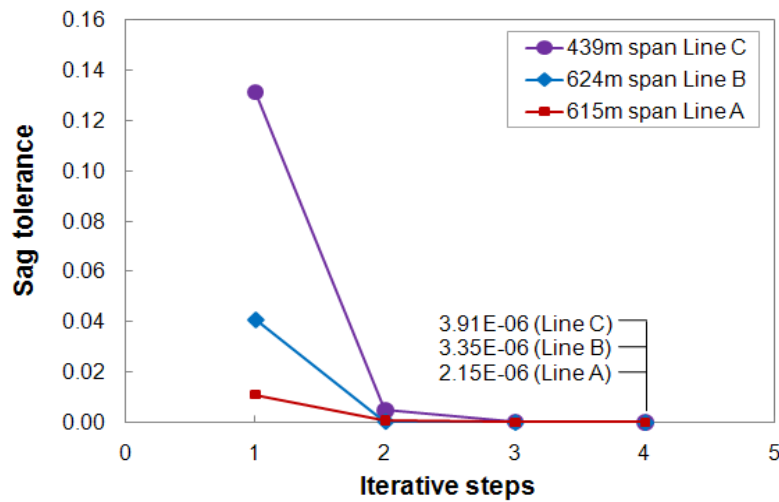


**Fig. 3.4:** Convergence checking based on sag tolerance of three lines

Convergence type based on displacement can employ “Total displacement”, “Last time step Displacement” or “First iteration Displacement” for verifying the convergence of solution. In which, method of displacement from last time step is very accurate for analyses with relatively small time steps. This method is the default and is useful for analyses that involve large-scale motion (as cable deformation). The displacement tolerance can be set around  $1e-3$  to  $1e-5$  for this method. Fig. 3.3 shows effect of tolerance size on accuracy of solution in nonlinear analysis. Sag tolerances of iterative process in the three transmission lines are conducted. Fig. 3.4, for example,

shows results of convergence checking of 615 m span in Line A, 624 m span in Line B and 439 m span in Line C. All of them reach convergence after three iterative steps (all of them fall in the range of  $1e-3$  to  $1e-5$ ).

### **3.2. Finite element model of the transmission line system**

The details of FE models for different components in three transmission lines are indicated in Fig. 3.5. The modeling of electric conductors is most essential in the FE modeling of the transmission line systems. FEMAP with NX Nastran is different from other commercial software. It does not deal with cable element. For modeling cable property, tension-only one-dimension element has been used. In creating the FE models of the transmission line systems, conductor profile under its body-load has been derived carefully due to the nonlinear characteristics of conductor and significant effect of sag-to-span ratio on the natural frequencies of vertical symmetric modes as shown in Fig. 7 (Ramberg, Griffin, 1977 and Irvine, 1981).

The spacers in the transmission line systems have a function to maintain the distance between conductors in a bundled-conductors and each conductor is clamped at the end of spacer arm. The tangential rotation of each conductor can be free or fixed depending upon the tightness of clamp thereby affecting on the torsional stiffness of conductor bundle. However, it has been found by preliminarily checking different types of spacer models that the spacer type does not change the torsional frequencies significantly. In this study, therefore, the spacers are modeled by two-node rigid tube elements having the rigid connection with the conductors.

The insulators consist of small links or ball-socket joints and have very low bending stiffness. Therefore, both tension and suspension insulators are modeled by three degree-of-freedom, two-node tube elements with zero bending stiffness. In the cases of Line A and Line B, the connections between insulators and conductors are established by the complex assembly of yoke plates, which affects the torsional frequencies of bundled-conductors (Keutgen, Lilien, 2000). In this analysis, the yoke plates are modeled by rigid plate elements.

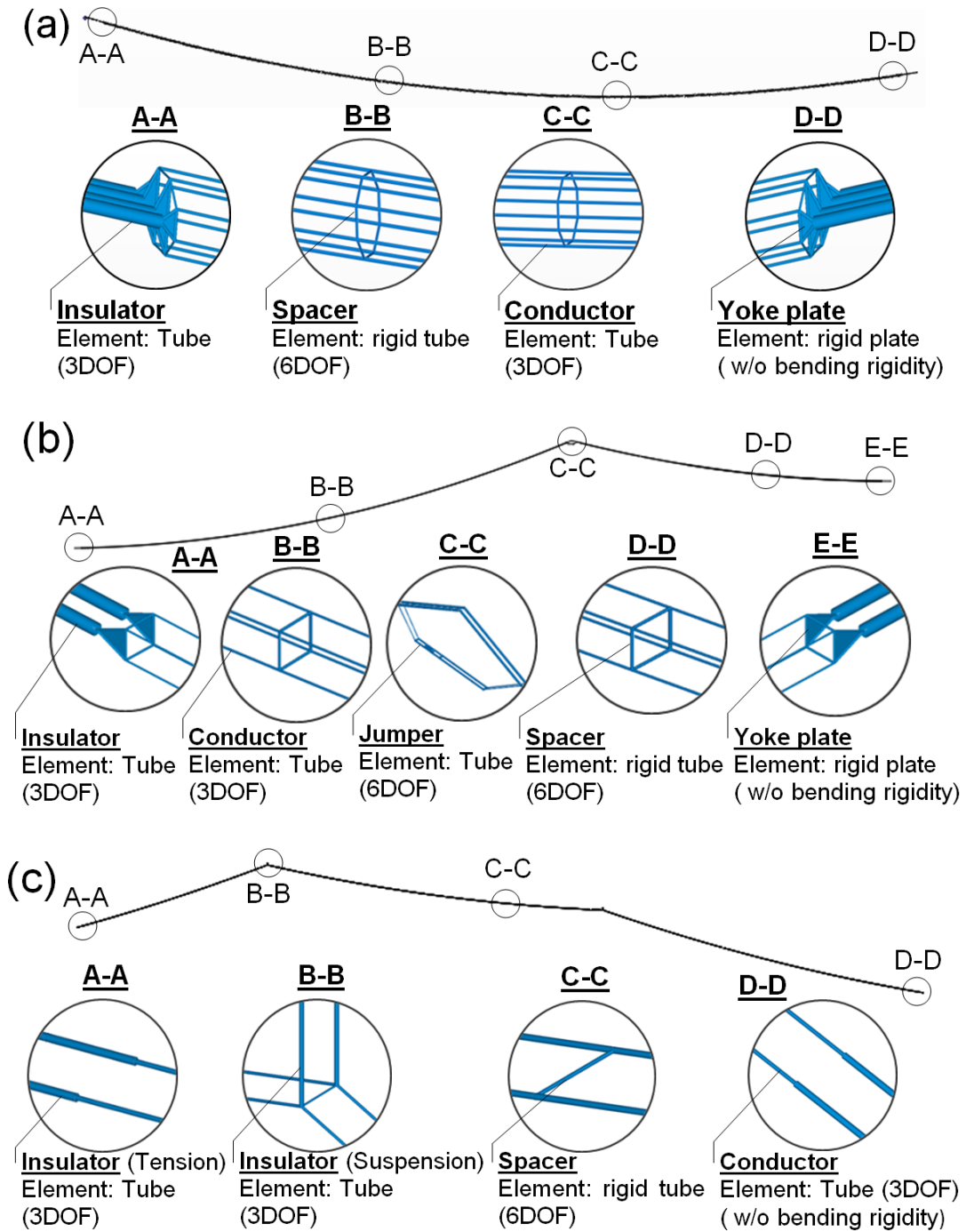


**Fig.3.5:** FE models of the transmission lines: (a) Line A; (b) Line B; and (c) Line C.

Finite element model of jumper is modeled and shown in Fig. 3.7(b). Mechanism of jumper's vibrations might be quite different from mechanism of span vibrations in the transmission line system. In this component, attention is paid to its

vibrations in local and global modes. Finally dynamic characteristic determined by FEM analysis are used to interpret measured spectra of jumper.

In the case of Line B, the main part of jumper is jumper pipe, which impose the conductors through the tower. The jumper pipes are connected to the insulators through the flexible jumper hangers at both ends by pivotal connections. In this analysis, the jumper pipes are modeled by two-node rigid tube elements, while three degree-of-freedom, two-node tube elements are applied to the flexible jumper hangers. Details of different components of the three transmission lines are given in Table 3.1.

**Table 3.1:** Specification of the transmission lines: Line A, Line B, and Line C.

			Line A	Line B	Line C
Trans- -mission lines	No. conductors		8	4	2
	No. of spans		1	2	3
	Span length	(m)	615	624	439
	Sag /span ratio		0.057	0.051	0.023
Conductor	Elastic modulus	( $10^9\text{N/m}^2$ )	69.9	90.6	90.6
	Diameter	(mm)	40.3	22.4	24.5
	Spacing	(m)	0.4	0.4	0.4
	Weight	(kg/m)	3.056	1.11	1.328
Spacer	Weight	(kg)	28	9.5	27
	Elastic modulus	( $10^9\text{N/m}^2$ )	210	210	210
Tension insulator	Length	(m)	13.91	7.43	3.6
	Weight	(kg)	14330	4076	275
	Elastic modulus	( $10^9\text{N/m}^2$ )	210	210	210

---

Suspension insulator	Length	(m)	3.5
	Weight	(kg)	290
	Elastic modulus	( $10^9\text{N/m}^2$ )	210
Jumper pipe	Diameter	(mm)	120
	Elastic modulus	( $10^9\text{N/m}^2$ )	63
Jumper hanger	Diameter	(mm)	40
	Elastic modulus	( $10^9\text{N/m}^2$ )	210

### 3.3. Natural frequencies and mode shapes

The eigenvalue analyses are then conducted for the FE models of the transmission lines with proper static equilibrium configurations, and the results of eigenvalue analyses are summarized in Table 3.2. It is confirmed, in the case of horizontal mode in each transmission line, that the lowest natural frequency corresponds to one loop-per-span mode and that the higher natural frequencies are nearly equal to the integral multiple of the lowest one. As for the vertical and torsional modes, on the other hand, these trends are somewhat perturbed by the sag effect especially for Line A and Line B, as discussed previously on Fig. 3.1.

In the case of Line A, for example, the lowest frequency of vertical one-loop mode is very close to the second natural frequency of vertical two-loop mode, and the one-loop mode shape is modified from the half-sinusoidal waveform. It is also noted that the torsional natural frequency is very close to the vertical one for each loop-per-span mode except the one loop-per-span mode. It is because the vertical and torsional modes are in-phase and out-of-phase motions of conductors in the bundle, respectively.

In the case of Line C, 439 m span and 421 m span are similar in their geometries. Therefore, coupling modes between two spans can be seen in the horizontal modes. For example, in the 0.178 Hz, one-loop horizontal mode of 421 m span, one-loop horizontal

modes of 439 m span seem to exist with smaller amplitude. Similarly, in the 0.337 Hz, two-loop mode of 421 m span and 0.357 Hz, 439 m span, there exist other two-loop modes coupling with their modes.

**Table 3.2:** Natural frequencies and mode shapes of Line A (refer Hung et al. 2014 for Line B and C).

	Horizontal	Vertical	Torsion
Line A	0.096 Hz 	0.180 Hz 	0.148 Hz 
	0.192 Hz 	0.190 Hz 	0.201 Hz 
	0.287 Hz 	0.293 Hz 	0.298 Hz 
	0.383 Hz 	0.382 Hz 	0.394 Hz 

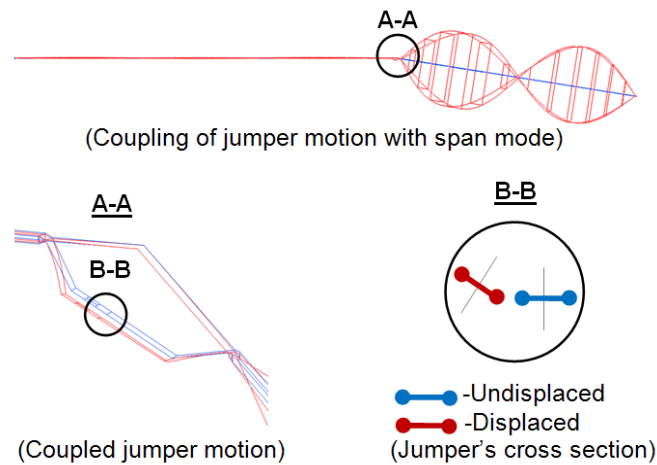


**Fig.3.6:** Coupling of jumper motion with two-loop torsional mode of 407 m span in Line B.

In the case of Line B, the jumper is also modeled to investigate its effect on the dynamic characteristics of the transmission lines. Figure 3.6 shows a coupling of jumper vibration with two-loop torsional mode of 407 m span in Line B. The corresponding natural frequency is 0.34 Hz. The figure shows clearly the coupling of horizontal and torsional vibrations of jumper with the torsional mode of the shorter span. Such coupling mode is important in the sense that large vibration in the jumper can be

induced by wind-induced span-vibration and result in its damage as observed by TEPCO.

### **3.4. Interpretation of characteristics of field-measured vibration**

The characteristics of field measured vibrations can be understood by the analytically evaluated natural frequencies and mode shapes. The spectral analysis is first conducted to investigate the time-averaged characteristics of wind-induced responses and wind velocities in the frequency domain. The dominant frequencies are then identified based on the peak response spectrum with the analytical natural frequencies and mode shapes.

Example of PSD of field-measured, wind-induced responses in the Line A are depicted in Fig. 3.7. All the dominant peak frequencies in the PSD are very close to the analytical natural frequencies, as shown in the figure where the analytical natural frequencies and associated mode shapes are also indicated.

In the case of Line A, there exist two equal-level dominant peaks corresponding to one-loop and two-loop modes in the horizontal PSD of quarter span response. These results in nearly equal RMS values of horizontal responses at the mid-span and quarter-span of Line A in Fig. 2.8. In the figure, the vertical RMSs are also in the same level, but this is caused by the fact that there exist almost identical one dominant peak for the mid-span and quarter-span responses, corresponding to the closely spaced natural frequencies of one-loop, and two-loop modes.

In the case of Line B, the dominant peak of quarter-span response, corresponding to the two-loop mode in the longer span, is most significant in the vertical PSD. This can clearly explain why the RMS of quarter-span response is larger than the others. Furthermore, the relatively large dominant peak of jumper response is recognized in its lateral PSD, associated with the torsional dominant peak of jumper as well as the torsional dominant peak of the quarter-point of 407 m span at almost same frequencies of about 0.34 Hz. This field observed phenomenon is clearly explained by previously discussed coupling mode of jumper and span in Fig. 3.6.

In the case of Line C, the PSDs of two spans are similar not only in their aspects but also in the levels of dominant peaks. This phenomenon can be seen in all three-direction responses. The horizontal PSD, for example, shows dominant peaks of two spans at almost same frequency of about 0.17 Hz for the mid-span and 0.35 Hz for the quarter-span. This may be caused by the fact that two spans characterized by the similar structural mechanics and geometry may behave similarly and easily to couple the modes between two spans as the results of eigenvalue analyses in Table 3.2.

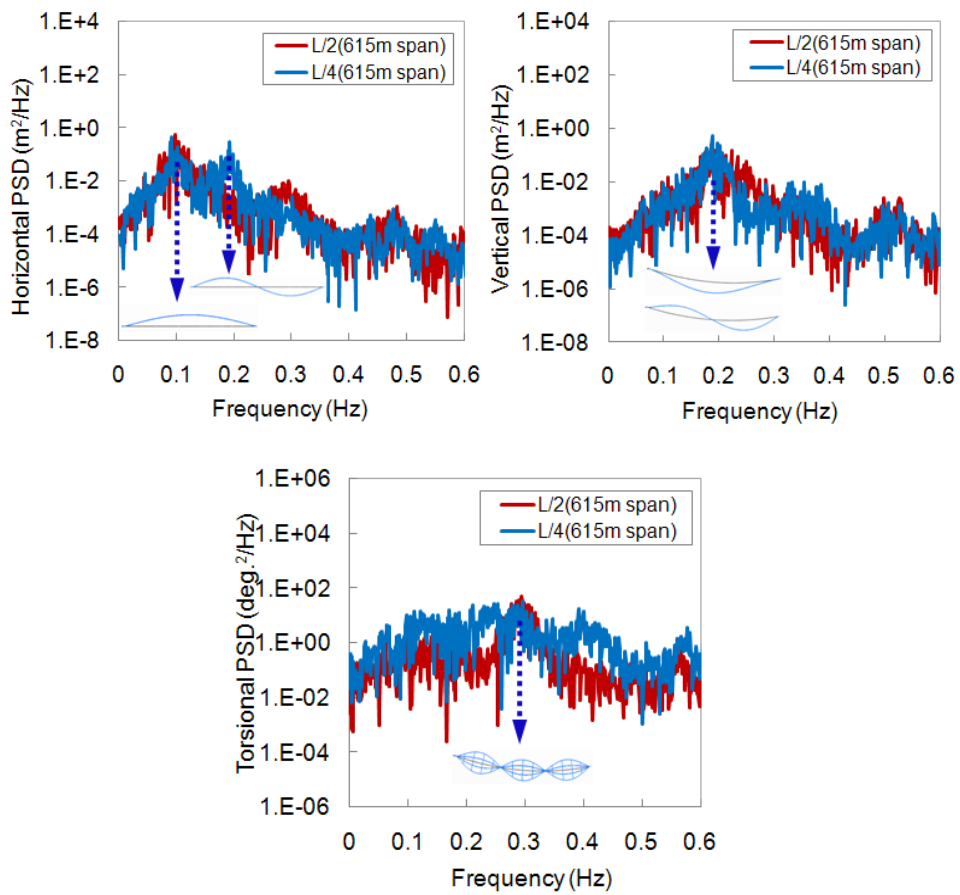


**Fig.3.7:** Examples of PSD of field measured responses of Line A (due to copyright of Elsevier, refer Hung et al. 2014 for Line B and C).

### 3.5. Conclusions

In this chapter, the static-equilibrium configurations of the three transmission lines have been created properly. The dynamic characteristics of the transmission lines have been identified reliably based on the result of eigenvalue analysis in FEMAP with NX Nastran computing software. The results of natural frequencies and mode shapes are used to interpret the field-measured vibration. Some major conclusions can be conducted as follows.

The well-known elastic-catenary theory that associated with the proposed iterative-algorithm can be usable to obtain the realizable static-equilibrium configuration of the conductor and to plays an important role to derive the appropriate FE models.

The results of eigenvalue analysis present a realizable natural frequencies and mode shapes that are used to interpret well the field-measured vibration in the frequency domain.

The coupling motion of the span and jumper can induce the very large-amplitude vibration of the jumper that can cause the damage of the jumper that was observed in the field.

**References**

- Wilson, A.J. and Wheen, R.J., (1974), "Direct Design of Taut Cables Under Uniform loading," ASCE Journal of Structural Division, Vol. 100, No. ST3, pp. 565-578
- Irvine, H.M., (1975), "Statics of Suspended Cables," ASCE journal of the engineering mechanics division, Vol. 101, No. EM3, pp. 187-205.
- Irvine, H.M. and Sinclair, G.B., (1976), "The Suspended Elastic Cable under the Action of Concentrated Vertical Loads," Journal of Solids and Structures, Vol. 12, pp 309-317.
- Irvine, H.M., (1981), Cable Structures, Dover Publications, New York.
- Vallabhan, C.V.G. and Kewaisy, T.H., (2001). "Stability of Step-by-Step integration for Nonlinear Cable Dynamics," Proceedings of ASCE/Texas Section Spring meeting, San Antonio, Texas.
- Ramberg, S.E., Griffin, O.M., (1977), "Free Vibrations of Taut and Slack Marine Cables," ASCE Journal of the Structural Division, Vol. 103, No. ST1 1, pp. 2079-2092.
- Leonard J.W., (1988), Tension Structures: Behavior & Analysis, McGraw-Hill, hic. New York.
- Keutgen R., Lilien J.L., 2000. Benchmark cases for galloping with results obtained from wind tunnel facilities-validation of a finite element model. IEEE Trans Power Delivery, 15, pp. 367-374.
- Hung, PV., Yamaguchi, H., Isozaki, M., Gull, JH, (2014). Large amplitude vibrations of long-span transmission lines with bundled conductors in gusty wind. J. Wind Eng. Ind. Aerodyn. 126, 48–59

## CHAPTER 4

### INTERPRETATION OF FIELD-MEASURED RESPONSES

#### BASED ON GUST RESPONSE ANALYSIS

---

1. Introduction
  2. Buffeting theory
  3. Assumptions on parameters in gust response analysis
  4. Results of gust analysis and comparison field-measured responses
  5. Conclusions
  6. References
- 

#### 4.1. Introduction

The framework of the buffeting theory that was proposed by Davenport 1962 is popular for the gust-response prediction of the civil structures such as bridges, towers and the transmission line in the frequency domain, in which the spectral analysis and statistical computation that is associated the modal-based structural analysis are the core. The theory also introduces a so-called correction functions such as the aerodynamic admittance function, coherence function to deal with assumptions of the quasi-steady theory. Even though the theory needs to accept the existence of the assumptions and uncertainties, but Davenport's method validates for the gust response prediction of the line-like structure in practice.

Irwin (1977) developed Davenport's method with suggesting the von Karman-typed power spectral densities for the atmospheric turbulence and coherence of the buffeting forces. Then, the theory was applied in the gust response analysis of the Lions' Gate suspension bridge.

The buffeting force generally depends on the geometrical configuration of structure, ongoing turbulent flow, and reduced frequency. The quasi-steady buffeting forces firstly proposed using the quasi-steady theory in the time domain. These buffeting forces are corrected by supplementing the frequency-dependant aerodynamic-admittance function to account the difference between the turbulence wind and the buffeting forces in the frequency domain as well as to cope with the limitation of the quasi-steady theory. With account of the spatial distribution characteristic of the buffeting forces, the spatial coherence function is added to deal with the limitation of the strip theory.

#### **4.2. Buffeting theory**

In the frequency-domain approach or the indirect buffeting analysis, Fourier transform is applied in associated with the statistical computation and the spectral analysis technique. The correction function has been added in the transformation steps. Furthermore, the modal analysis technique in generalized coordinates is applied to decompose the multi-degree-of-freedom motion system into the single-degree-of-freedom. Thus, the core of the frequency-domain buffeting analysis relates to the modal decomposition method and the modal-based superposition technique that are associated with the spectral analysis method.

Davenport's approach for determining the resonant dynamic responses of a structure in the particular modes under gusty wind is summarized in Fig. 4.1 and is applied to analyze the wind-induced vibrations of the transmission lines.

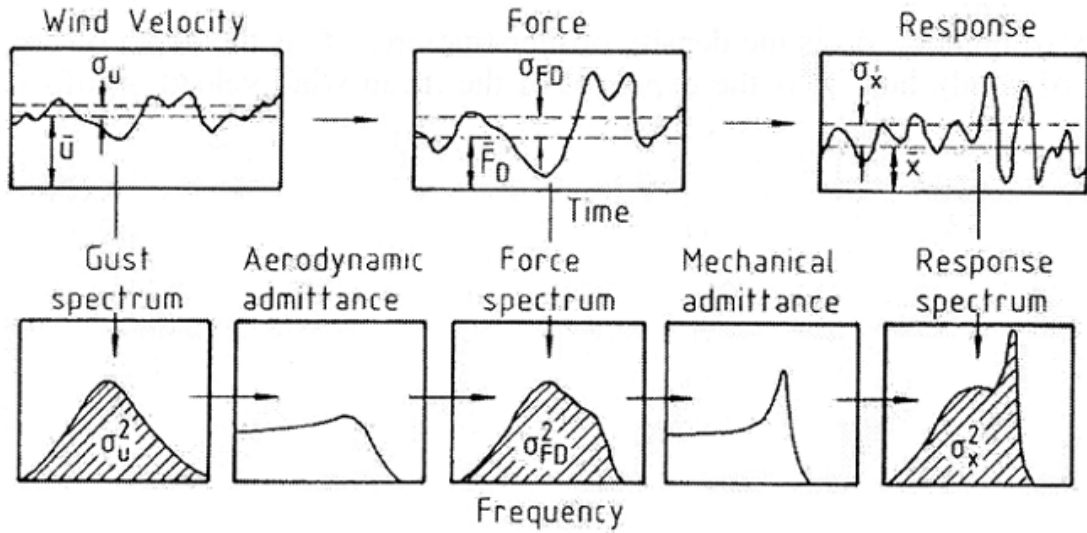


**Fig. 4.1:** Davenport's approach for wind-induced resonant response (Davenport 1967)

In the frequency domain, the buffeting theory presented in Fig. 4.1 can be expressed by Eq. (4.1). Equation (4.1) is derived by neglecting both the aerodynamic interaction among conductors in a conductor bundle and nearly-zero lift force in individual conductor because of circle-cross section of conductor. The first assumption is plausible because the separation between two conductors is larger than 10 times of conductor diameter (Zhang et al., 2000) and the second assumption can be justified by conductor's circular shape in absence of ice. Buffeting theory is presented in detail in Appendix B.

$$S_r(f) = S_u(f) \times \left[ \rho C_D \chi_i(f) d_c n_c l \bar{U} \right]^2 \sum_{i=1}^N \frac{\phi_i^2}{M_i^2} |J(f_i)|^2 |H(f_i)|^2 \quad (4.1)$$

where  $S_r$ ,  $S_u$  are the power spectral densities of dynamic response and wind velocity fluctuation,  $\rho$  is the air density,  $C_D$  is the drag force coefficient for a single conductor,  $|\chi_i(f)|^2$  is the aerodynamic admittance,  $d_c$  is the diameter of conductor,  $n_c$  is the

number of conductors in a bundle,  $l$  is the span of the transmission line,  $\bar{U}$  is the mean wind velocity normal to the transmission line,  $\phi_i$  is the mode shape vector of  $i^{th}$  mode.  $M_i$  is the mass-normalized coefficient and can be expressed as follows.

$$M_i = m \int_0^l \phi_i^2(x) dx \quad (4.2)$$

where  $m$  is the mass per unit length of a bundle of conductors.

$|J_i(f)|^2$  in Eq. (4.1) is the joint-acceptant ffunction, can be thought as a weighting function for wind loads dependant on the frequency dependant correlation of wind velocity across the structure, n as follows.

$$|J_i(f)|^2 = \int_0^l \int_0^l \exp\left(-\frac{kf}{\bar{U}}|x_1 - x_2|\right) \phi_i(x_1) \phi_i(x_2) dx_1 dx_2 \quad (4.3)$$

where  $x$  is position along the length of the transmission line;  $\exp\left(-\frac{kf}{\bar{U}}|x_1 - x_2|\right)$  represents the frequency-dependant correlation of wind velocity and  $k$  is an empirical constant.

Furthermore,  $|H_i(f)|^2$  is the mechanical admittance of the transmission line and can be expressed as follows.

$$|H_i(f)|^2 = \frac{I}{(2\pi f_i)^4} \frac{I}{\left\{1 - (f/f_i)^2\right\}^2 + (2\xi_i f/f_i)^2} \quad (4.4)$$

where  $f_i$  is the natural frequency of  $i^{th}$  mode and  $\xi_i$  is the sum of structural and aerodynamic damping ratios for the  $i^{th}$  mode.

Once the PSD of response is obtained by Eq. (4.1), the RMS of response can be calculated by the following equation.

$$RMS_r = \left[ \int_0^{\infty} S_r(f) df \right]^{0.5} \quad (4.5)$$

### 4.3. Assumptions on parameters in gust response analysis

The measured wind data is used to calculate the gust responses of three transmission lines, while there are many uncertain parameters assumed in the gust response analysis. Table 4.1 and 4.2 summarized the assumed values of that uncertain variable in the present analysis, and the following are brief explanations and discussions on their appropriateness.

The air density depends on the temperature, pressure and presence of moisture, and is  $1.342 \text{ kg/m}^3$  at  $-10^\circ\text{C}$  and  $1.204 \text{ kg/m}^3$  at  $20^\circ\text{C}$  under the standard atmospheric pressure and in absence of moisture. In this analysis, its value is taken as  $1.204 \text{ kg/m}^3$  because the possible change in its value may not affect the results of analysis significantly.

The force coefficients for different conductors are provided by TEPCO, and their values for un-iced single conductor normally range from 1.25 to 0.89, which can be affected by the turbulence intensity of wind. In this study, an average value of 1.0 is assumed, while the RMS response calculated by using this averaged value can have 16 % difference from the one by using the extreme value of force coefficients.

The aerodynamic admittance is introduced to counter the effect of flow modification due to the motion of structure on the force coefficients. The transmission line conductors, being very slender and moving with very small velocity as compared to

the velocity of oncoming wind, do not modify the flow significantly. Therefore, the aerodynamic admittance for the transmission lines is assumed as one.

An appropriate value of  $k$ , which is the empirical constant in the frequency-dependent correlation of wind velocity, can be determined only through experimentation, but Holmes discusses on its general range from 10 to 20 (Holme JD, 2001). The possible change in its value may not affect the results significantly and therefore the value of  $k$  is taken as 15.

The damping in the transmission lines is dominated by the aerodynamic damping because their structural damping is negligible small. Matheson et al (1981) and Holmes (2001) pointed out that the resonant response of the transmission line conductor is largely damped out because of the very large aerodynamic damping of about 20% to 25% of critical damping for high wind velocity. Regarding the structural damping of the transmission line conductor, McClure et al. (2003) selected 2% of critical damping for the bare cable. By referring to the quasi-steady theory of aerodynamic damping (Stroman EN, 2006), approximately appropriate values of damping ratios, that gives appropriate sharpness and width of resonant peak, are assumed in the current analysis, as given in Table 4.2.

The objective of the gust response analysis in this section is to interpret and characterize the field-measured responses as gust response but not to investigate the effects of varying-uncertain parameters on the gust responses. Furthermore, it is not feasible to run a series of values for studying the propagation of uncertainties corresponding to such a huge dataset of field-measured responses.

Table 4.1 Uncertain parameters assumed in gust response analysis.

Variable	Description	Value
$\rho$	Air density (kg/m <sup>3</sup> )	1.204
$C_{D,L,M}$	Drag coefficient single conductor	1.0
$\chi$	Aerodynamic admittance	1

$k$	Empirical constant in frequency dependant correlation of wind velocity	15
-----	--	----

Table 4.2 Aerodynamic damping ratios assumed in gust response analysis.

Mode	Line A			Line B			Line C		
	<i>Hor.</i>	<i>Vert.</i>	<i>Tor.</i>	<i>Hor.</i>	<i>Vert.</i>	<i>Tor.</i>	<i>Hor.</i>	<i>Vert.</i>	<i>Tor.</i>
1	6%	4%	2%	5%	2%	2%	4%	2%	1%
2	7%	3%	2%	4%	2%	1%	3%	3%	1%
3	5%	3%	1%	4%	2%	1%			
4	4%	3%	1%						

#### 4.4. Results of gust analysis and comparison with field measured responses

The analytically evaluated RMS responses were compared with all the measured-vibration data at all the measure point of three transmission lines, and it was found that almost all the cases show good agreement. In the followings, therefore, some important examples of RMS comparison are only discussed. In order to understand completely the field-measured vibrations, beside the cases of good agreement in RMS comparison, some other cases with the particular characteristics are also selected to be discussed. The discussed cases are underlined as shown in Table 4.3.

##### 4.4.1. *Gust response analysis of Line A*

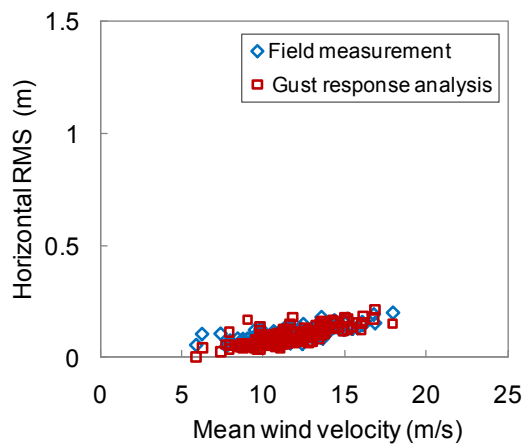
One example of the good agreement in the horizontal RMS comparisons is the case of Line A at the mid-point of 615 m span, as shown in Fig. 4.2. It is found that all of three response components are reproduced very well by the theory-based gust response analysis. The good-agreement can be understood by looking into the PSD

comparison of each event, and the PSD of typical event in the gust response analysis of Line A is depicted in Fig. 4.3, in which the analytical and experimental responses show very small discrepancy.

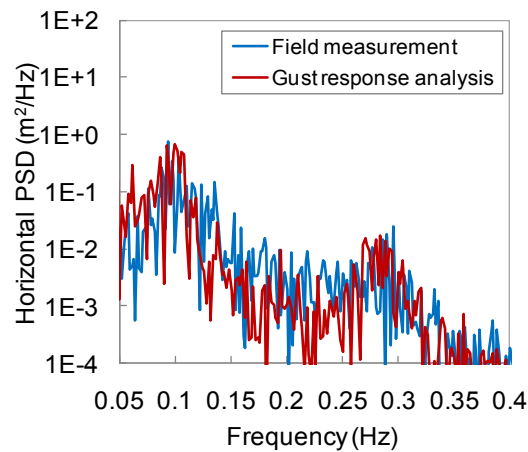
Table 4.3 Results of RMS comparison

Line	Span	Point	Scattering/Agreement/(Case study)		
			Horizon	Vertical	Torsion
Line A	615m	L/2	<u>1/a</u>	<u>1/a</u>	<u>1/a</u>
		L/4	1/a	1/a	1/a
Line B	624m	L/2	2/b	2/a	2/a
		L/4	2/a	<u>2/b</u>	1/a
	Jumper	L/2	<u>1/a</u>	1/a	<u>1/a</u>
	407m	L/2	<u>2/b</u>	<u>1/a</u>	<u>3/b</u>
		L/4	2/a	1/a	1/a
Line C	439m	L/4	1/a	<u>3/c</u>	1/a
	421m	L/4	1/a	1/a	1/a

Note: "1", "2", "3" corresponding to very small, small, large scattering of data RMS ; and "a", "b", "c" corresponding to very good, good, weak agreement between data and theory RMS



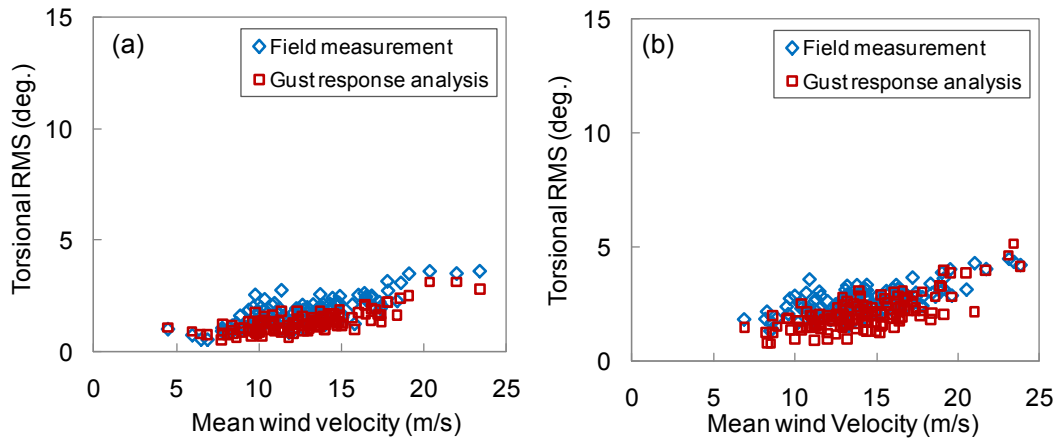
**Fig. 4.2:** Horizontal RMS comparison at L/2 of 615 m span in Line A (refer Hung et al. 2014 for other RMS comparisons).



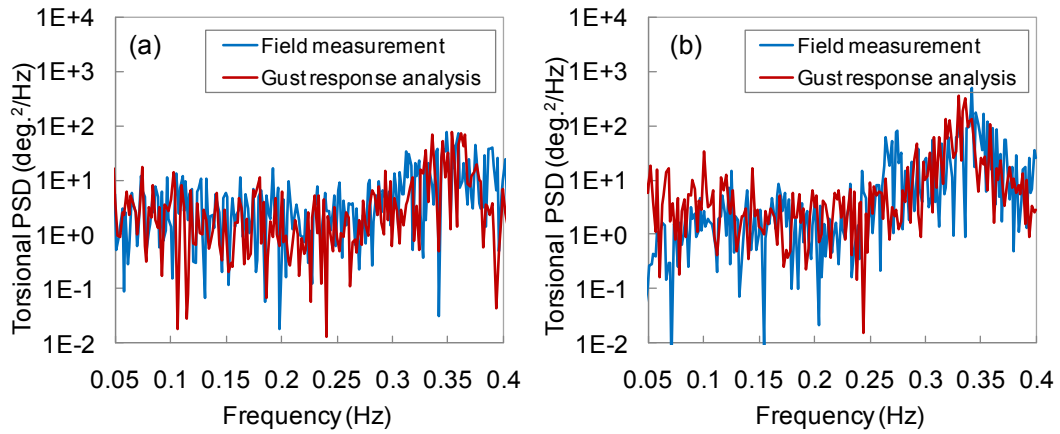
**Fig. 4.3:** Horizontal PSD comparison at L/2 of 615 m span in Line A (refer Hung et al. 2014 for other PSDs).

#### 4.4.2. Gust response analysis of Line B

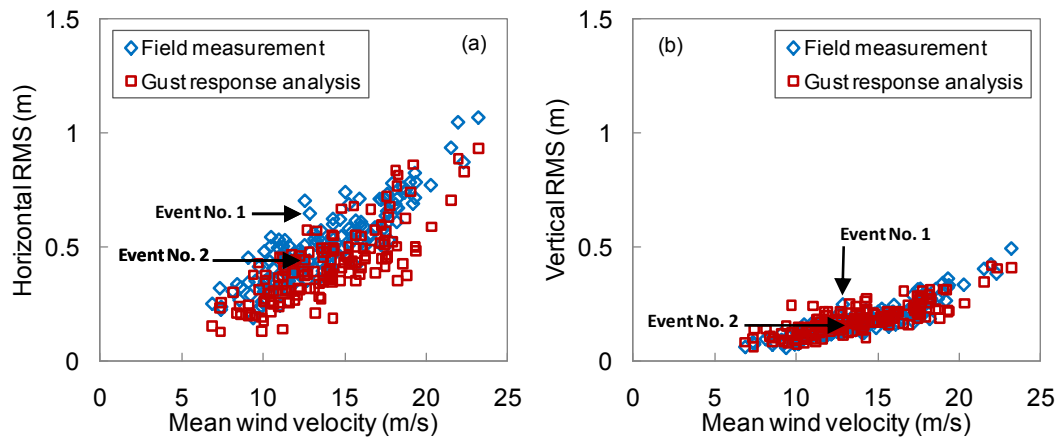
As mentioned previously in the results of eigenvalue analysis, the horizontal and torsional motions of jumper are coupled with the torsional motion of span at the natural frequency of 0.34 Hz in the case of Line B. This characteristic was reflected in the gust response analysis and results in the good agreement in the RMS comparison in Fig. 4.4, which is supported by the small discrepancy in PSD comparison in Fig. 4.5. The coupling characteristics can be also seen in these figures. The torsional RMS responses of jumper in Figs. 4.4(a) show similar tendency to the torsional RMS response of the quarter-point of 407 m span in Fig. 4.4(b), and all of the PSD comparisons in Fig. 4.5 show the same dominant peaks around their coupling frequency of 0.34 Hz.



**Fig. 4.4:** RMS comparison of coupled jumper and span responses in Line B: (a) Torsional RMS of jumper; (b) Torsional RMS of quarter-point 407 m span.



**Fig. 4.5:** PSD Comparison of jumper in Line B. (a) Torsional PSD of jumper and (b) Torsional PSD of quarter-point 407 m span.



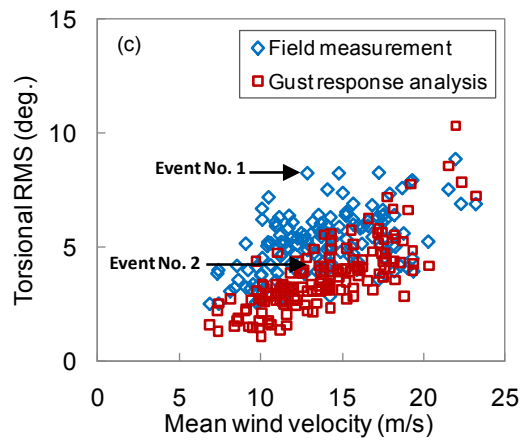
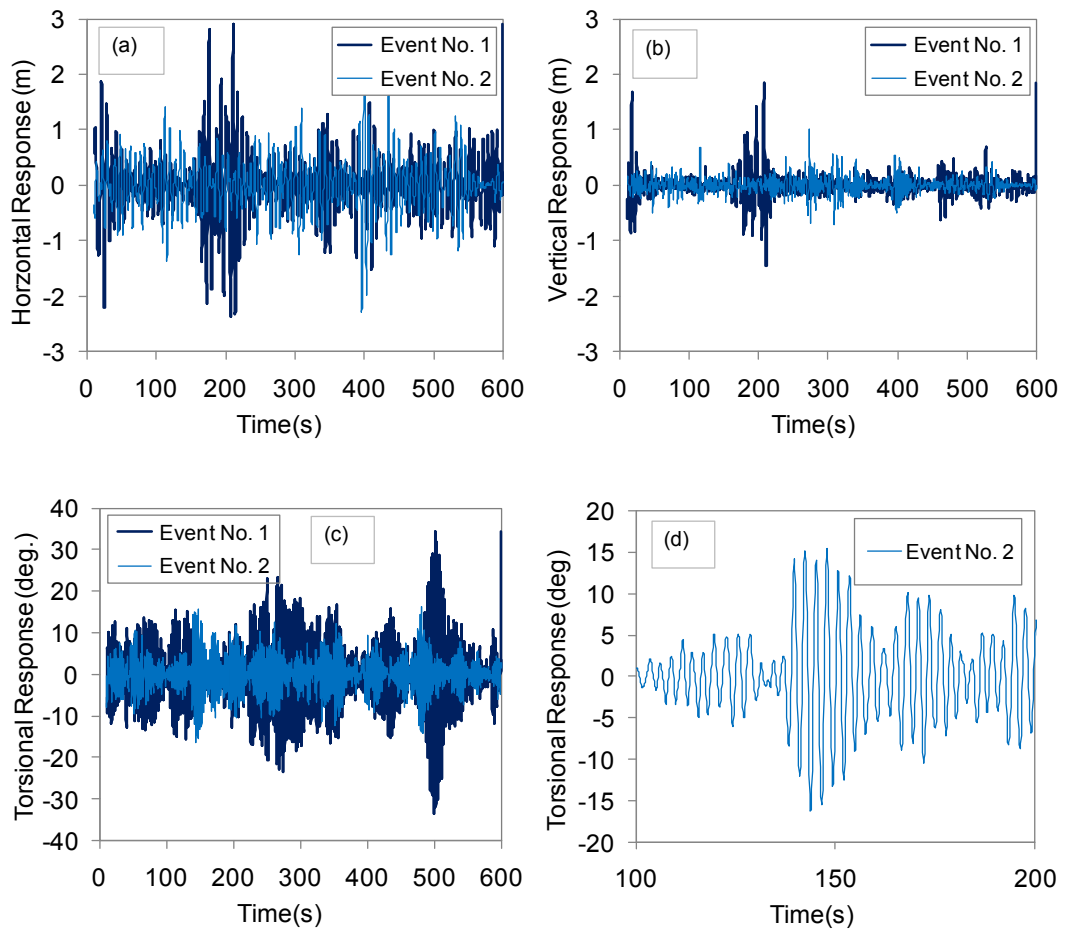
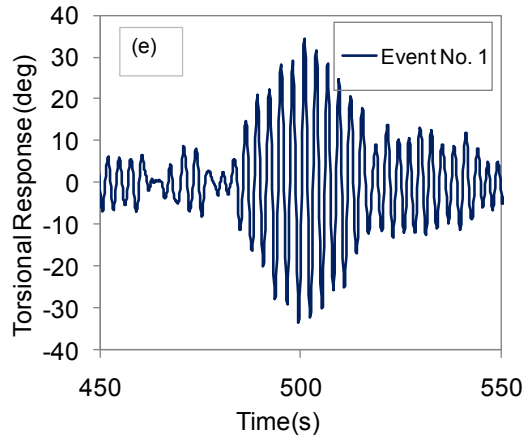
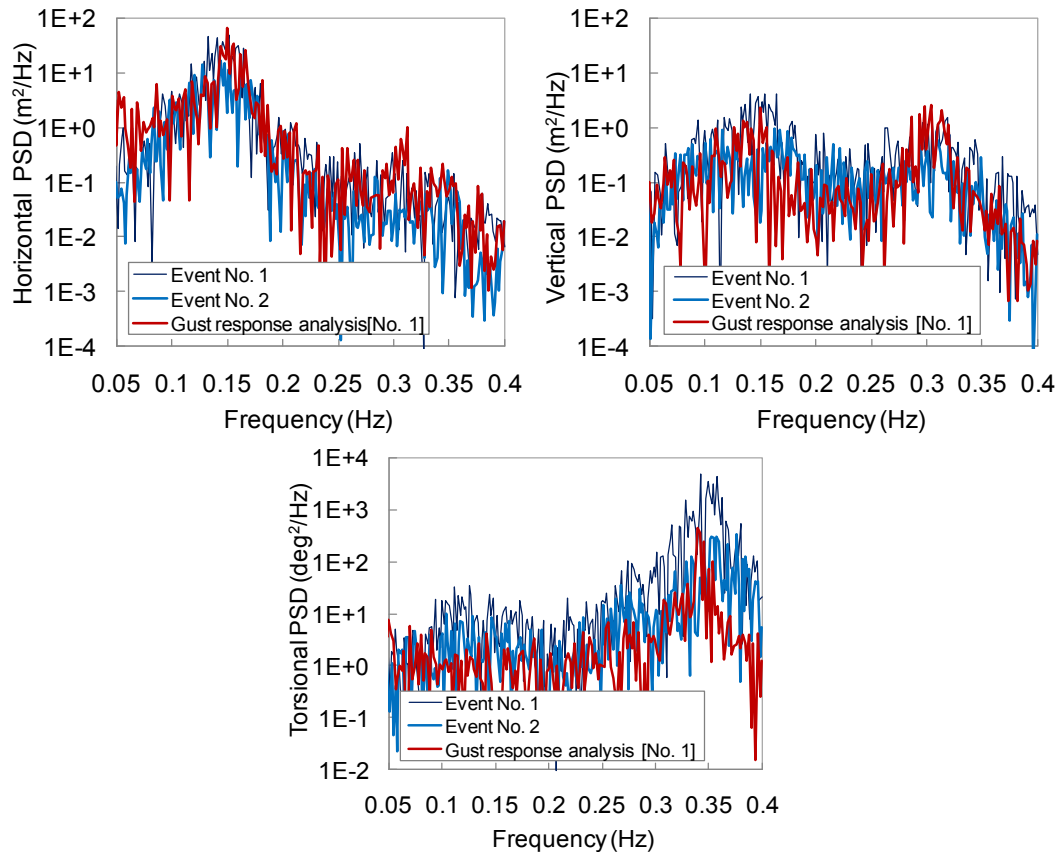


Fig. 4.6: RMS comparison at L/2 of 407 m span in Line B.





**Fig. 4.7:** Time series of responses in Events No. 1 and No. 2: (a) Horizontal, (b) Vertical, (c) Torsional, (d) Event No. 2-maximum amplitude torsional, and Event No.1-maximum amplitude torsional responses.



**Fig. 4.8:** PSD comparison at L/2 of 407 m span in Line B.

Another special case in the case of Line B is the vibration responses at the mid-point of 407 m span that have very large response amplitudes compared to all other cases in three lines, as shown in Table 2.3. Their RMS comparisons between the field

measurement and the gust response analysis are shown in Fig. 4.6. In the figures, scatterings of RMS are small with good agreements in the horizontal and vertical RMS comparisons. While, relatively large discrepancy is seen in the torsional RMS comparison. Fig. 4.7 shows the time series of response in two events selected in Fig. 4.6, in which Event No. 1 and Event No. 2 are located at same mean wind velocity with good agreement and weak agreement in the torsional RMS, respectively. The time series of two events suggest that both the horizontal and vertical responses are possibly gust responses because of suddenly developed large amplitudes in short period of time, but that the torsional response could not be a galloping response because of gradually developed large amplitude round 500 sec in the Event No. 1 as shown in Fig. 4.7(e). These suggestions are supported partly by the PSD comparison having good agreement in the horizontal and vertical responses but significant discrepancy in the torsional response in the Event No. 1, as shown in Fig. 4.8.

#### *4.4.3. Gust response analysis of Line C*

One more example of large discrepancy in the RMS comparison is the vertical response at L/4 of 439 m span in Line C in Fig. 4.9 (a), where Event No. 3 and No. 4 are selected for the cases of weak agreement and good agreement, respectively. Their PSD comparisons are shown in Fig. 4.9 (b, c), indicating very significant discrepancy in the case of Event No. 3. This suggests that the Event No. 3 could not be a gust response, while study that is more detailed is indispensable. Based on the above results and discussions, it can be concluded that the gust response analysis can reproduce well the field-measured vibrations and that most of the field-measured large amplitude vibrations of three transmission lines are possibly gust-type vibrations except some cases.

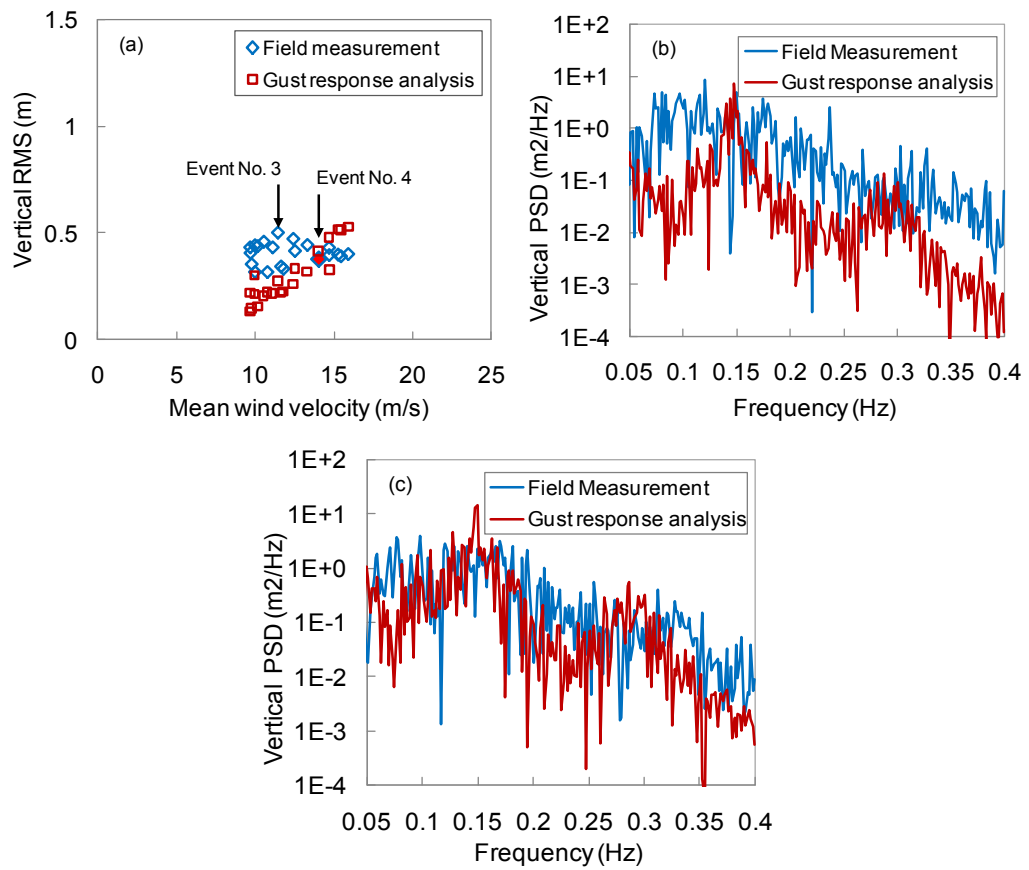


**Fig. 4.9:** Comparison of vertical response at L/4 of 439 m span in Line C: (a) RMS; (b) PSD of Event No. 3 (weak agreement) and (c) PSD of Event No. 4 (good agreement).

## 4.5. Conclusions

In this chapter, Davenport's approach for determining the resonant dynamic responses of the particular modes of the transmission line in the presence of the gusty wind is employed. The results give a good understanding about the characteristics of field-measured data. Based on the clear identification about the characteristics of the field-large-amplitude vibration, the appropriate vibration-controlled method can be considered in the further works. From the results, some conclusions can be conducted as follows.

The analytical RMS was compared with the measured-RMS of the vibration response of the three transmission lines. The result shows that the almost cases have a good agreement between the analytical and measured vibration response.

The time series of the events that show the weak agreement point out that those events could not be a gust response because of gradually developed large amplitude.

The range of the frequency in which the low-frequency peaks contribute to the total response much larger than that that of the higher-frequency peaks in the response spectra.

From the results of the parabolic trend in the RMS comparison, it can be preliminarily concluded that almost the field-measured vibration is possibility of gust response.

## References

- Davenport, A.G. (1962), "The response of slender, line-like structures to a gusty wind", Proc. Inst. Civ. Eng., 23, pp. 389-408.
- Davenport, A.G., 1980: "Gust Response Factors for Transmission Line Loading". Wind Engineering, Proc. of the Fifth International Conference on Wind Engineering, J.E. Cermak, Ed. (Fort Collins, CO; July 1979), Pergamon Press, New York, NY.
- Fekr, M.R., McClure, G., 1998. Numerical modeling of the dynamic response of ice shedding on electrical transmission lines. Atmospheric Research 46, 1–11.
- Holme JD, 2001. Wind loading of structures. London: Spon Press.
- Matsumoto, M. (2000), Aeroelasticity and bridge aerodynamics, Textbook for Int'l Advanced Course on Wind Engineering, Genoa, Italy.
- Simiu, E., Scanlan, S.H. (1997), Wind Effects on Structures, John Wiley&Sons.
- Solari, G., Tubino, F. (2005), "Gust response of long span bridges by double modal transformation", The 4th Euro. and Afri. Conf. on Wind Eng. (EACWE4), Prague, Czech.
- Stroman EN, 2006. Theory of Bridge Aerodynamics. Springer.
- Zhang Q. et al., 2000. Galloping of bundled-conductor. Journal of sound and vibration 234 (1), pp. 115 134.
- Hung, PV., Yamaguchi, H., Isozaki, M., Gull, JH, (2014). Large amplitude vibrations of long-span transmission lines with bundled conductors in gusty wind. J. Wind Eng. Ind. Aerodyn. 126, 48–59

## CHAPTER 5

# PREDICTION OF LARGE AMPLITUDE GUST RESPONSE IN

## TIME DOMAIN

---

1. Introduction
  2. Time-domain-gust-response analysis
  3. Wind-field simulation
  4. Gust response simulation
  5. Remark and future works
  6. References
- 

### 5.1. Introduction

A significant feature of approach of time-domain gust response analysis is that the time-dependent characteristics of the unsteady aerodynamic forces and nonlinearities of the both aerodynamic and structural origins can be taken into account. There are two different numerical methods for the gust-response analysis: modal and direct response analysis methods. The direct method that performs numerically the time integration on the complete coupled equations of motion is applied in this analysis. The other one utilizes the mode shapes of the structure to reduce and uncouple the equations of motion (when modal or no damping is used). Then, the solution is obtained through the summation of the individual-mode responses.

Regard to the time-domain vibration analysis of the line-like-structure such as bridge, transmission line... many research have been conducted. Matsumoto et al. 1994, Boonyapinyo et al. 1999 ... have conducted the buffeting response analysis of bridges in coupling with the aero-elastic forces in the time domain. Liang et al. 2002 pointed out that the proper orthogonal decomposition-POD (Lumley 1970), has been applied in many engineering fields. Tubino and Solari 2005 simulated random fields. Carassale et al. 1999, Solari and Carassale 2000, Chen and Kareem 2000 studied stochastic dynamic response, etc. The stochastic response of structures formulated in the time domain using the covariance-proper transformation is appropriate because of its direct and capable solutions for nonlinear problems and unsteady aerodynamics.

In the time-domain-gust-response analysis of the transmission line subjected to the wind field, the wind-load time series at the sites of the transmission lines are important for accurate simulation since aerodynamic behaviors are sensitive to the selected winds (Bocciolone et al., 1992; Chen et al., 2000). However, since it is difficult to measure the time series of the turbulence field at the all points in the site, therefore the digital simulation techniques are often used to generate the time histories of turbulence field by using two approaches: the spectral-representation methods and the time-series-representation ones. In the former, the decomposition techniques such as the Cholesky' decomposition and the modal decomposition have been applied, whereas some methods such as the auto-regressive technique, moving-average technique and auto-regressive and moving average technique. In the wind-field simulation, the field-measured-wind velocity that is the typical large-amplitude events are selected for simulating the space-time-depended wind field. The FE model of the transmission line subjected to the nodal space-time-depended wind is analyzed by using FEMAP with NX Nastran computing software. The results of the simulated nodal-response time series will compare with the measured nodal-response time series at the middle- and quarter-point.

## **5.2. Time-domain-gust-response analysis**

### 5.2.1. Typical time series of the vibration response

The transmission line conductor is wind-sensitive structure. A typical form of response for the line-like structure subjected to the wind loading is illustrated in Fig. 5.1. In the figure, the total response is consisted of three components: (1) Mean response in time  $\bar{r}$ , (2) Background response  $\tilde{r}_B$ , (3) Resonant response  $\tilde{r}_{Rj}$ . In the following analysis, nodal vibration response at middle-points and quarter points of two transmission line models are compared with that of the field-measurement.

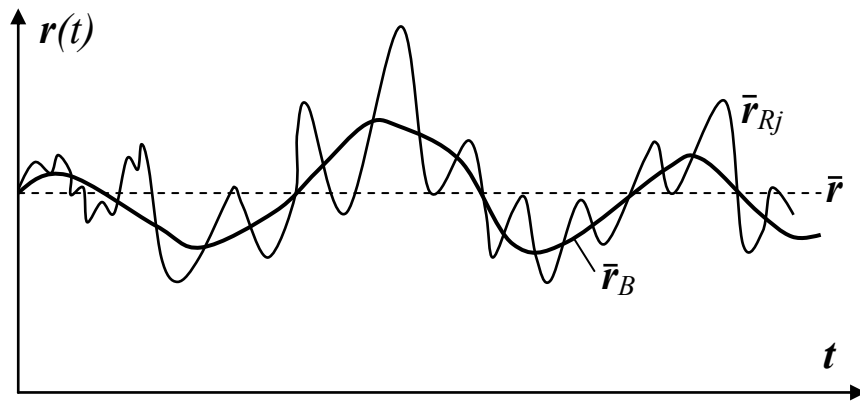


Fig.5.1: Typical response time history of structure to wind.

### 5.2.2. Equation of motion

Multi-DOF motion equations of the transmission line conductor subjected to the buffeting forces is expressed generally as follows:

$$\mathbf{M}\ddot{\mathbf{u}}(x,t) + \mathbf{C}\dot{\mathbf{u}}(x,t) + \mathbf{K}\mathbf{u}(x,t) = \mathbf{F}_b(t) \quad (5.1)$$

where  $\mathbf{u}(x,t)$ ,  $\dot{\mathbf{u}}(x,t)$ ,  $\ddot{\mathbf{u}}(x,t)$  are the deflection and its first, second order derivatives.  $\mathbf{M}$ ,  $\mathbf{C}$ ,  $\mathbf{K}$  are the mass, damping, stiffness matrices;  $\mathbf{F}_b(t)$  is the buffeting forces.

The buffeting forces per unit length of conductor bundle can be expressed and corrected by the frequency-dependant admittance functions as follows.

$$L_b(t) = \frac{1}{2} \rho U^2 d_c n_c \left[ C_L \chi_{L_u}(f) \frac{2u(t)}{U} + (C'_L + C_D) \chi_{L_w}(f) \frac{w(t)}{U} \right] \quad (5.2.a)$$

$$D_b(t) = \frac{1}{2} \rho U^2 d_c n_c \left[ C_D \chi_{Du}(f) \frac{2u(t)}{U} + (C'_D - C_L) \chi_{Dw}(f) \frac{w(t)}{U} \right] \quad (5.2.b)$$

$$M_b(t) = \frac{1}{2} \rho U^2 (d_c n_c)^2 \left[ C_M \chi_{Mu}(f) \frac{2u(t)}{U} + C'_M \chi_{Mw}(f) \frac{w(t)}{U} \right] \quad (5.2.c)$$

where  $C_L$ ,  $C_D$ ,  $C_M$  are the aerodynamic coefficients at the balanced angle;  $C'_L$ ,  $C'_D$ ,  $C'_M$  are the first-order derivatives with respect to the angle of attack;  $d_c, n_c$  are the diameter of the bundle-conductor and number of bundled-conductor;  $\chi_{Fv}(F=L, D, M; v=u, w)$  is the aerodynamic transfer functions between the turbulent components and forces.

Based on the dynamic equation of the motion in the matrix form as shown in Eq. (5.1), the structural response is solved at each fixed discrete-time step  $\Delta t$ . A benefit presents itself if  $\Delta t$  remains constant during the analysis. The efficiency of the direct solution is that the output time-interval could be greater than that of the solution time-interval due to reducing the cost of the analysis time. In many cases, it is not necessary to sample output response at each solution time. The theory of time-domain analysis is summarized in Appendix C.

### 5.2.3. Solution for vibration response analysis

The equations of motion, Eq. (5.1), will be solved by using the direct-time-integrate method that is employed the solver of NX Nastran computing software based on the FE model of the transmission line and the simulated-nodal wind force.

For the basic NX Nastran solver, the nonlinear-direct-transient-response analysis that is the most general method for the computing-based-dynamic response analysis is used. The purpose of the nonlinear-direct-transient-response-analysis is to compute the dynamic response of the transmission line subjected to the time-varying excitation. The time-varying excitation is explicitly defined by the time-dependent function. All of the forces that apply to the transmission line are known at the every time steps. The obtained results from the analysis are the nodal translation in the three directions. In the NX Nastran basic solver, the option of the nonlinear properties, “geometry” and “large displacement”, is selected in the bulk-data setup. The “direct time integration” solution

type is selected in the modal-analysis setup. The wind velocity is recorded in 600 seconds with the time step of 0.02 second. However, in present analysis, a 200-second-wind time series is used because the 200-second-wind time series is appropriate length to capture the type of vibration response as well as to reduce the cost of the time analysis and computer capacity. It should be noted that the field data of the wind and response is synchronized for the real time in the 200-second that will make sense in the measured-simulated response comparison. The analysis program is discussed in detail in the section 5.4. Due to the cable-type structure, the overall structural damping is selected as assumed in the frequency-domain analysis. The loading case is combined of the body-load and the simulated-nodal-wind force time series, in which the simulated-nodal-wind force is presented in chapter 5.3.

### **5.3. Wind-field simulation**

#### *5.3.1. Introduction*

It is difficult to obtain the time series of wind velocity at all points in the site. Therefore, the digital simulation techniques are often used to generate the time series of wind field at all of the simulated nodes. In the time domain analysis, the accurate of results depends significantly on the simulated time series of wind load acted on the conductors since the aerodynamic response are sensitive to the winds (Chen et al., 2000). Nodal-wind force per unit length of conductor is calculated using Eq. (5.2) based on the mean wind velocity and the turbulent wind that vary in the time and space along span.

There are some wind field simulation techniques to simulate the stochastic wind field, in which spectral representation technique and time-series representation one are often used. The present analysis employs the spectral representation technique to generate the nodal wind time-series based on the measured wind records.

### 5.3.2. Hypotheses for wind field simulation

The transmission line conductor is a two-dimensional, large-scale structure. The continuous wind fields should be divided into the finite parts to facilitate the calculation. Each part has two components; mean and turbulent wind in three directions, along  $u(t)$ , vertical  $v(t)$ , and lateral  $w(t)$  turbulences (Simiu and Scanlan, 1978). Because of the small effect, the longitudinal turbulent wind  $w(t)$  is often neglected.

The turbulent wind with zero mean is a function of time  $(t)$  and spatial coordinates  $(x, y, z)$  while the mean wind is a function of the spatial coordinates. The mean wind at different location depended on height of the simulated points is consistent with the power law and obtained using Eq. (2.1). Along  $u(t)$  and vertical  $v(t)$  turbulent wind are considered as the two independent one-dimensional multi-variate spatially correlated Gaussian random processes. These stochastic processes at the simulated points are obtained from the cross-spectral matrix using Cholesky decomposition technique in which the empirical PSD functions of Kaimal and Panofski in Eq. (2.6) are fitted the measured PSD of turbulence.

It is assumed that all of nodes in the same cross-section of the conductor bundle have a same wind time series. Therefore, only one wind time series is simulated at one cross-section of conductor bundle.

### 5.3.3. Theory of wind-field simulation

As mentioned previously, along and vertical turbulent components  $u(t)$ ,  $w(t)$  are considered as two multi-variate spatially-correlated Gaussian-random processes with zero mean. The turbulent fields at “n” discrete nodes (Fig.5.2) are expressed as follows:

$$u(t) = \{u_1(t), u_2(t), \dots, u_n(t)\}^T \quad (5.3-a)$$

$$v(t) = \{v_1(t), v_2(t), \dots, v_n(t)\}^T \quad (5.3-b)$$

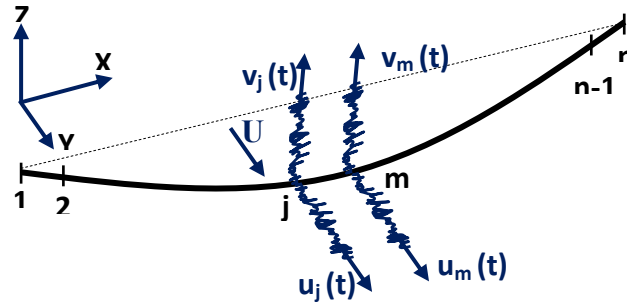


**Fig.5.2:** Turbulent field at nodes.

The cross-spectral density matrix  $S^0(\omega)$  of one-dimension n-variate process  $[u(t) \text{ or } w(t)]$  is given by:

$$S^0(\omega) = \begin{bmatrix} S_{11}^0(\omega) & S_{12}^0(\omega) & \dots & S_{1n}^0(\omega) \\ S_{21}^0(\omega) & S_{22}^0(\omega) & \dots & S_{2n}^0(\omega) \\ \vdots & \vdots & & \vdots \\ S_{n1}^0(\omega) & S_{n2}^0(\omega) & \dots & S_{nn}^0(\omega) \end{bmatrix} \quad (5.4)$$

To simulate the one-dimensional multi-variate stationary stochastic process, using Cholesky's method,  $S^0(\omega)$  can be performed as follows in which  $H(\omega)$  matrix is a lower-triangular matrix:

$$S^0(\omega) = H(\omega)H^{T*}(\omega) \quad (5.5)$$

$$H(\omega) = \begin{bmatrix} H_{11}(\omega) & 0 & \dots & 0 \\ H_{21}(\omega) & H_{22}(\omega) & \dots & 0 \\ \vdots & \vdots & & \vdots \\ H_{n1}(\omega) & H_{n2}(\omega) & \dots & H_{nn}(\omega) \end{bmatrix} \quad (5.6)$$

Where the diagonal elements are real and non-negative functions of  $\omega$ , and off-diagonal elements are generally complex functions of  $\omega$ .

Then, the stochastic process can be simulated by the following series (Wag et al.)

$$f_j(t) = 2 \sum_{m=1}^j \sum_{l=1}^N |H_{jm}(\omega)| \sqrt{\Delta\omega} \cos(\omega_{ml}t - \theta_{jm}(\omega_{ml}) + \phi_{ml}) \quad (5.7)$$

Where:

$$f(t) = u(t), w(t); j = 1, 2, \dots, n$$

m: moving node index

l: moving point/freq. range

N: freq. interval number

$\Delta_n$ : freq. interval

$n_{ml}$ : freq. point/freq. range

$\theta_{jl}$ : complex phase angle of  $H_{jm}$

$\phi_{ml}$ : random phase angle  $[0-2\pi]$

To derive the element of  $H(\omega)$  matrix in eq. (5.7), let's consider the cross-spectra of the appropriate-wind turbulence between nodes j and m.

$$S_{jm}^0(\omega) = \sqrt{S_{jj}^0(\omega)S_{mm}^0(\omega)} \text{Coh}(\Delta_{jm}, \omega) = S(\omega) \text{Coh}(\Delta_{jm}, \omega) \quad (5.8)$$

where

$$\text{Coh}(\Delta_{jm}, \omega) = \exp\left(-\frac{\lambda\omega\Delta_{jm}}{2\pi U(Z)}\right) = \exp\left(-\frac{\lambda\omega\Delta|j-m|}{2\pi U(Z)}\right) = \left(\exp\left(-\frac{\lambda\omega\Delta}{2\pi U(Z)}\right)\right)^{|j-m|} = C^{|j-m|} \quad (5.9)$$

The cross-spectral density matrix  $S^0(\omega)$  can be rewritten as:

$$\mathbf{S}^0(\omega) = \mathbf{S}(\omega) \begin{bmatrix} 1 & C & \dots & C^{n-1} \\ C & 1 & \dots & C^{n-2} \\ \vdots & \vdots & & \vdots \\ C^{n-1} & C^{n-2} & \dots & 1 \end{bmatrix} \quad (5.10)$$

Using Cholesky's method,  $H(\omega)$  matrix can be determined as follows:

$$\mathbf{H}(\omega) = \sqrt{\mathbf{S}(\omega)} \mathbf{G}(\omega) \quad (5.11)$$

$$\text{Where } \mathbf{G}(\omega) = \begin{bmatrix} 1 & & & & & 0 \\ C & \sqrt{1-C^2} & & & & \\ C^2 & C\sqrt{1-C^2} & \sqrt{1-C^2} & & & \\ C^3 & C^2\sqrt{1-C^2} & C\sqrt{1-C^2} & \sqrt{1-C^2} & & \\ \vdots & \vdots & \vdots & \vdots & \sqrt{1-C^2} & \\ C^{n-1} & C^{n-2}\sqrt{1-C^2} & C^{n-3}\sqrt{1-C^2} & C^{n-4}\sqrt{1-C^2} & \dots & \sqrt{1-C^2} \end{bmatrix} \quad (5.12)$$

Therefore, for example, along wind time series at  $i^{\text{th}}$  node can be simulated by the following equation:

$$u_i(t) = \sqrt{2\Delta\omega} \sum_{l=1}^n \sum_{k=1}^N \sqrt{\mathbf{S}_{ii}(\omega_k)} \mathbf{G}(\omega_k) \cos(\omega_k t + \phi_{lk}) \quad (5.13)$$

$$\text{where } G_{jm}(\omega) = \begin{cases} 0, & 1 \leq j < m < n \\ C^{|j-m|}, & m=1, m \leq j \leq n \\ C^{|j-m|} \sqrt{(1-C^2)}, & 2 \leq m \leq j \leq n \end{cases}$$

#### 5.3.4. Application of wind-field simulation

As mentioned previously, the wind field changes along span. Therefore, to facilitate the wind simulation at the finite nodes of the conductor, a grid that defines the coordinates of Line A is considered as shown in Fig. 5.3, in which the wind time series at every grid points are simulated. Based on the measured-wind record at the reference point (top of tower, node#1), the mean wind at each grid point is obtained by using the power law theory with the consideration of the terrain condition and the turbulence spectra is obtained based on the fitted cross-spectra and the cross-spectra-density matrix.

In the application, a grid of the structural coordinate has the height and width of 100m and 600m, respectively, in which the number of horizontal segment and vertical segment are 30 and 10 segments, respectively. The mean-wind velocity at the referred point is 19.4m/s (top of tower). The fitting result of the referred-point spectra to Kaimal spectra model  $\frac{fS_u(f)}{u_*^2} = \frac{an}{(1+bn)^{5c/3}}$  that is used to simulate the grid-point turbulence

spectra is conducted as follows:  $a=220$ ;  $b=45$ ;  $c=0.95$  with  $k=0.4$ ;  $z_1=0.01\text{m}$ ;  $z_2=100\text{m}$ ;  $u_* = 1.5$ ;  $\alpha=0.2$  (terrain condition) whereas in the Kaimal spectrum the parameters are  $a=200$ ;  $b=50$ ;  $c=1$ . The along-turbulence spectra comparisons are plotted in Fig. 5.4.

Some assumptions in this simulation are selected as follows. Horizontal and Vertical length of grid size are 600m and 100m. Number of grid steps is 30 steps for Horizontal direction and 10 steps for Vertical direction. Spectral of  $u(t)$  is Kaimal model. Line A with dataset number 155 is applied.  $\alpha$  is selected to be 0.2 in Line A terrain condition with mountains + bushes. Davenport introduced  $\lambda$  parameter from seven to ten. Frost corrected it with  $\lambda$  equal to 7.5, also selected in this simulation. Wind spectra is obtained by using constant  $k$  equal to 0.4, altitude  $Z$  equal to 100m, roughness length  $Z_0$  equal to 0.5m. Length of wind time series is 10 minutes with sampling Frequency equal to 50Hz, time step equal to 0.02 second, and Butterworth of high-pass filter used 0.05Hz for cutoff frequency.

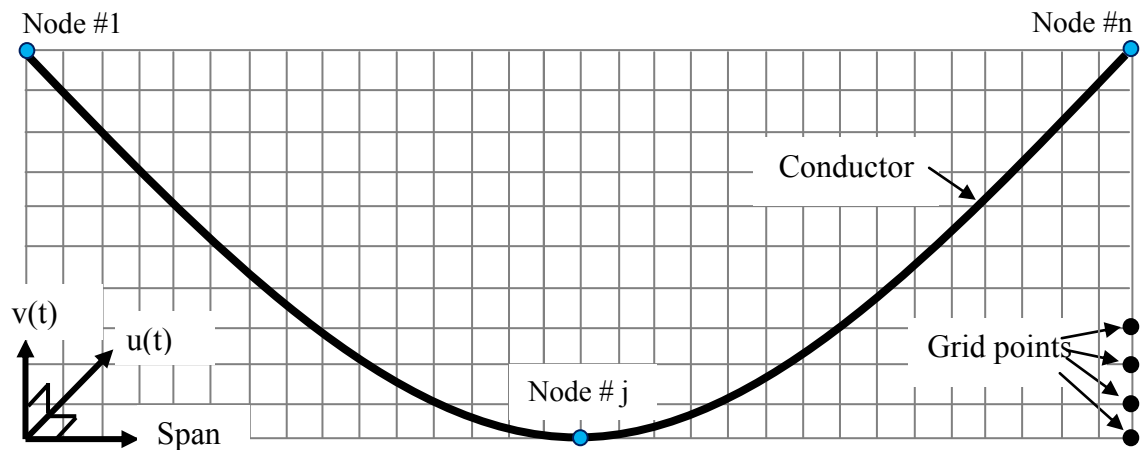


**Fig.5.3:** Grid used in turbulence simulation

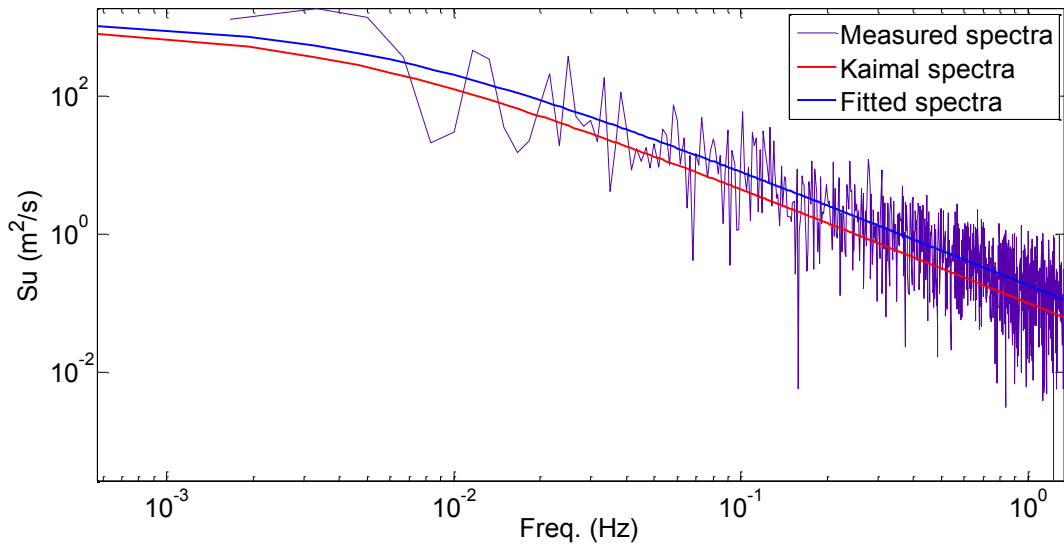
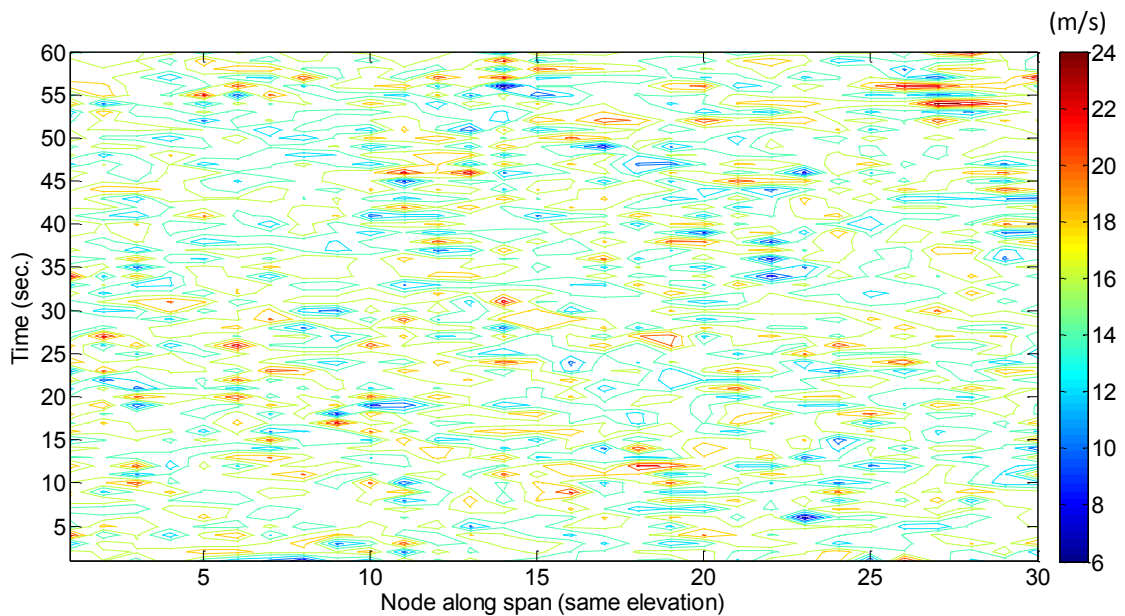


**Fig.5.4:** Comparison of PSD in along wind direction.

Results of the simulated-wind time series of Line A listed as follows. In the Fig.5.5, the distribution of the wind series along span (same elevation) is considered at mid- and quarter-span, for example. Figure 5.6 shows three nodal-wind time series at three sample grid points. It could be said that it is impossible to obtain the simulated-wind field that is equal exactly to the measured-wind field because of the stochastic procedure. However, with the consideration of the fitting the spectra model to the measured spectra and the terrain condition in the site, the result of the wind simulation is expected to be appropriate with the wind field.

At L/2 elevation



At L/4 elevation

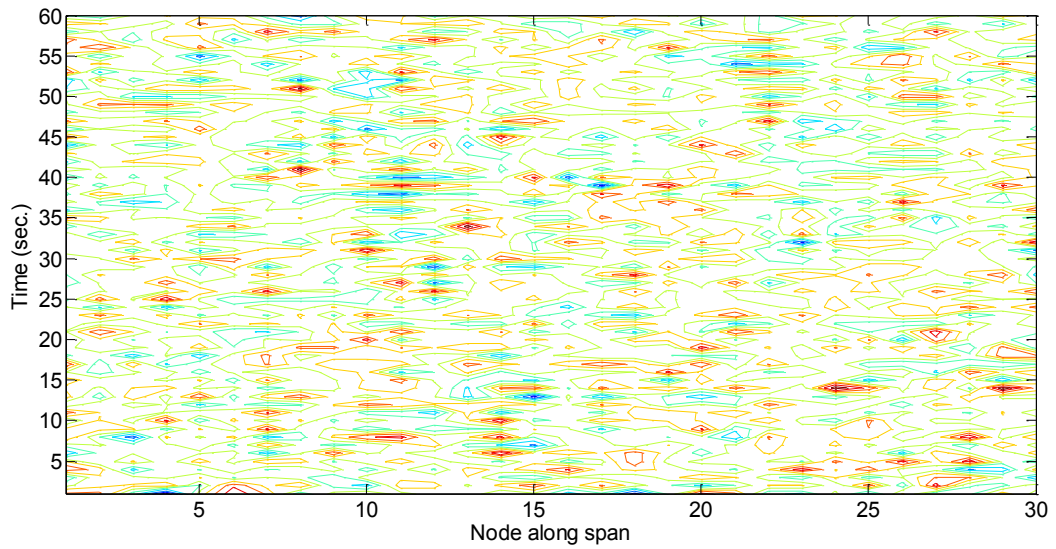
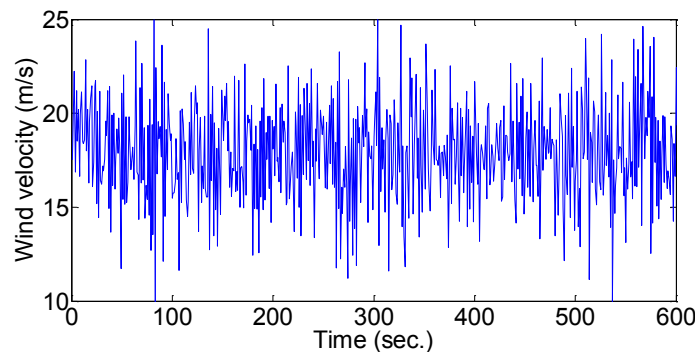
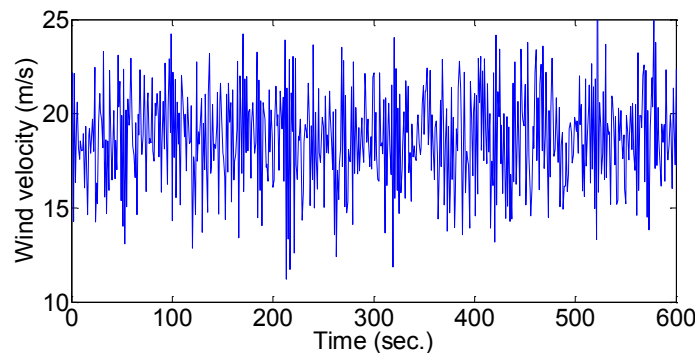


**Fig.5.5:** Distribution of the wind series along span

At L/2 node (mean wind= 17.9 m/s)



At L/4 node (mean wind=18.6 m/s)



At top-tower node (mean wind=19.4 m/s)

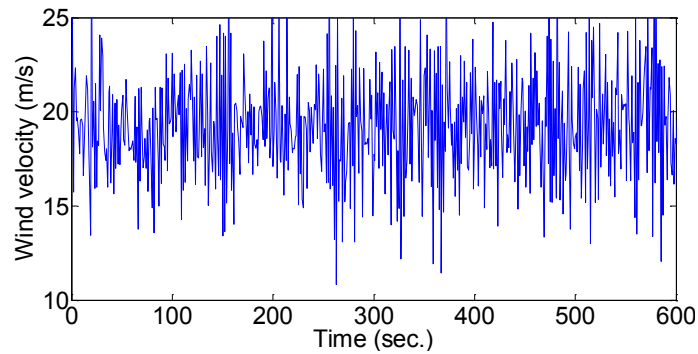


**Fig.5.6:** Wind time series at node

## 5.4. Gust response simulation

### 5.4.1. Assumptions on parameters

The nodal-wind-force is calculated from Eq. (5.2). In the equation, there are some uncertain parameters assumed in the following analysis. Almost parameters are selected in Table 4.1. In the preliminary-time-domain gust-response analysis, along and vertical wind turbulence are selected from the result of the wind-field simulation. Based on Eq. (5.2), the nodal-wind-force time series are applied on all of the considered nodes. Tables 5.1 summarize the assumed values of those uncertain variables in the present analysis.

In this study, the simulated-response time series is compared with the field-measured response that synchronized the measured-turbulent wind used in the wind-field simulation. Scheme of the time-domain gust-response comparison is shown in Fig. 5.7. As mentioned previously, a 200-second time series is used in the simulation and comparison because the time series of 200 seconds is sufficient to capture the structural vibration response dominated by the wind forces. Obviously, FE model of the long-span, large-conductor bundle transmission lines has an enormous number of node and element. Therefore, a long time series often leads to some trouble due to the cost and analysis time, etc. Although the simulated-vibration responses is obtained from the simulated-

wind field based on the measured wind. However, as mentioned previously the simulated-wind is not equal exactly to the wind field in the site due to the stochastic process and uncertain assumptions. It is impossible to get an exact-vibration response time series as the measured-vibration-response time series. Therefore, main objective of this analysis is to investigate the distribution of the large-amplitude gust response in the time series. Based on the result, the large amplitude or MPPA of bundle-conductor due to the gusty wind can be predicted for further purposes such as design code, structural health monitoring (phase-to-phase flashovers), etc.

In comparison, some points of discussion can be given as follows. Firstly, an agreement between the field-measured response and simulated one is unexpected in the first 100-seconds because the result lack of the history of the excitation and response before the 100-second time series. Secondly, the simulated-vibration response should be conducted in the same sampling frequency (10Hz) with field-measured vibration response for an appropriate comparison.

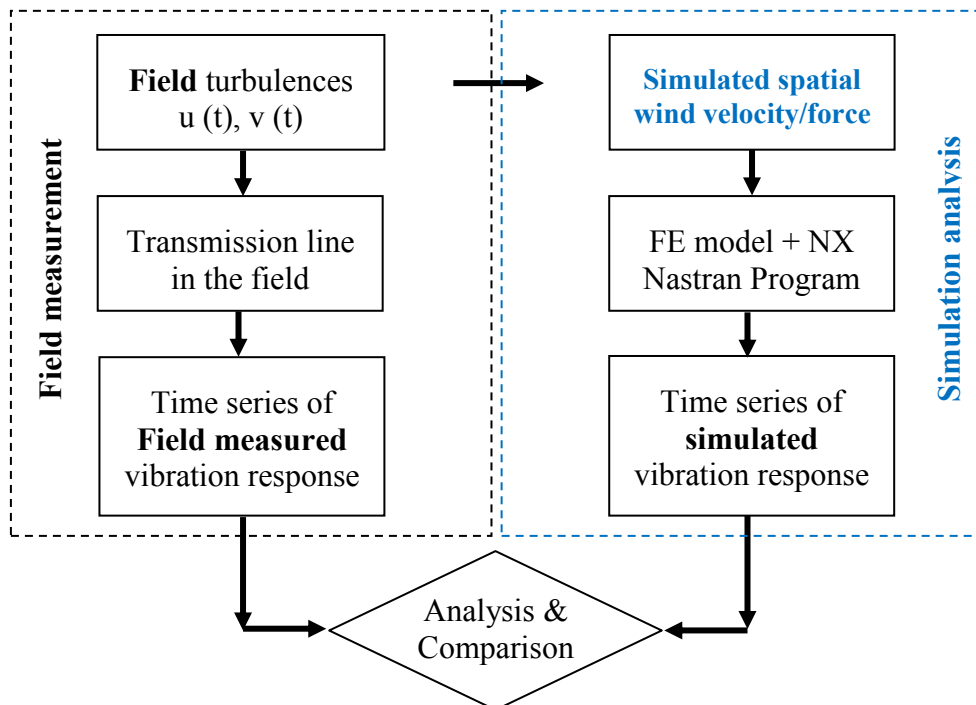


Fig. 5.7. Scheme of framework in time-domain gust-response analysis.

5.4.2. Time-domain gust response analysis

In this chapter, the time-domain gust-response analysis of Line A (Fig.5.8) subjected to the simulated-wind in chapter 5.3 is conducted by using the basic NX Nastran solver. The time series of drag-, lift- and torsional-wind forces are calculated by using Eq. 5.2. Based on length of elements, the nodal-wind-force time series is obtained. For example, the nodal-wind-force time series at mid-span that is resulted from assumed parameters in Table 5.1 is shown in Fig.5.9.

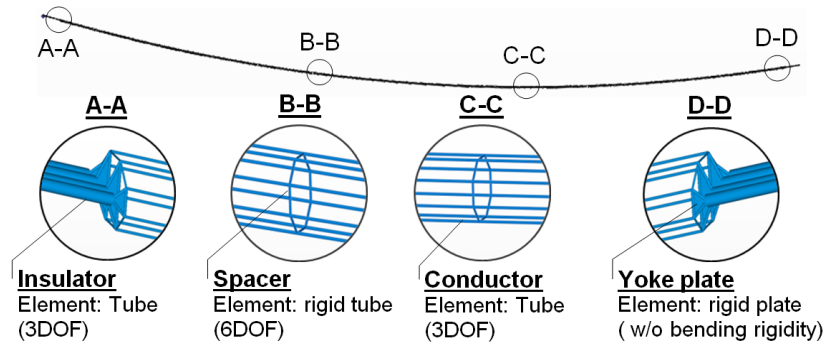


Fig. 5.8. FE model of Line A

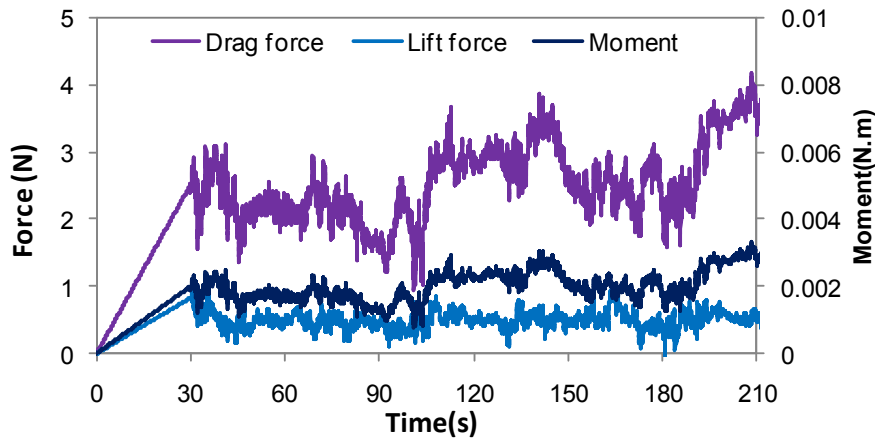


Fig. 5.9. An example of nodal wind force of sub-conductor at mid-span with 30s-gredually-increased loading

Table 5.1

$\rho$ air density (kg/m <sup>3</sup> )	U mean wind (m/s)	$d_c$ cable diameter (m)	$n_c$ number of cable	$\chi$ Aerodyn. admittance	$C_D, C_L, C_M$ Force coefficient ( $\varphi=0$ )	$C'_D, C'_L, C'_M$ 1 <sup>st</sup> derivatives ( $\varphi=0$ )
1.204	17.9	0.0403	8	1	0.76; 0.05; -0.003	0.1; -0.006; -0.0002

The basic NX Nastran solver is employed to analyze the time-domain-gust response, in which the solver is setup to run a 26000-step calculation with 0.02-second of the time increment to obtain a 200-second vibration-response time series. Damping

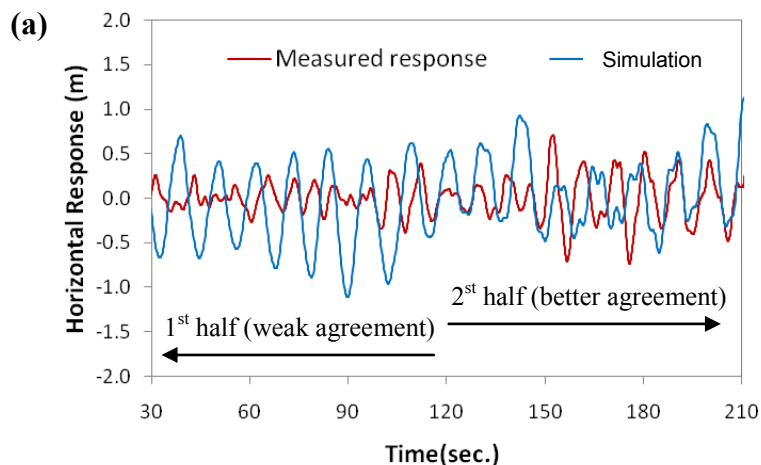
ratio is selected to be 1% critical damping that is recommended for dynamic analysis in NX Nastran.

Fig.5.10 (a), (b), and (c) show the time series of the conductor-response at mid-span in the horizontal, vertical, and torsional directions, respectively. In case of horizontal response, amplitude of vibration response is larger than field-measured response. This could be due large along wind force even a pre-loading of 30 seconds was applied. From 100<sup>th</sup> second to 200<sup>th</sup> second, the vibration amplitude of both simulation and measurement has good agreement about response magnitude and shape of response. As mentioned previously, the second half of response history, conductor vibrated without affection of along wind force at beginning of loading.

In the case of vertical response, the response amplitudes look similar whole history. The first reason could be due to linear-force coefficient used in the calculation of model wind force. The second reason could come from the affection of dead-load that is combined with wind force in this analysis.

In the case of torsional response, the vibration response of simulation and measurement has good agreement. Almost amplitudes are similar excepted amplitude around 150<sup>th</sup> second. The measured amplitudes are bit larger than that of simulation.

In preliminary analysis, time-varied force coefficient and aerodynamic damping matrix have not included into the analysis program. These two critical points are recommended to solve in future work for a better simulation. However, it could be understood the fact that, a lot of uncertain parameters concerning FE model, spatial wind simulation, wind force model,



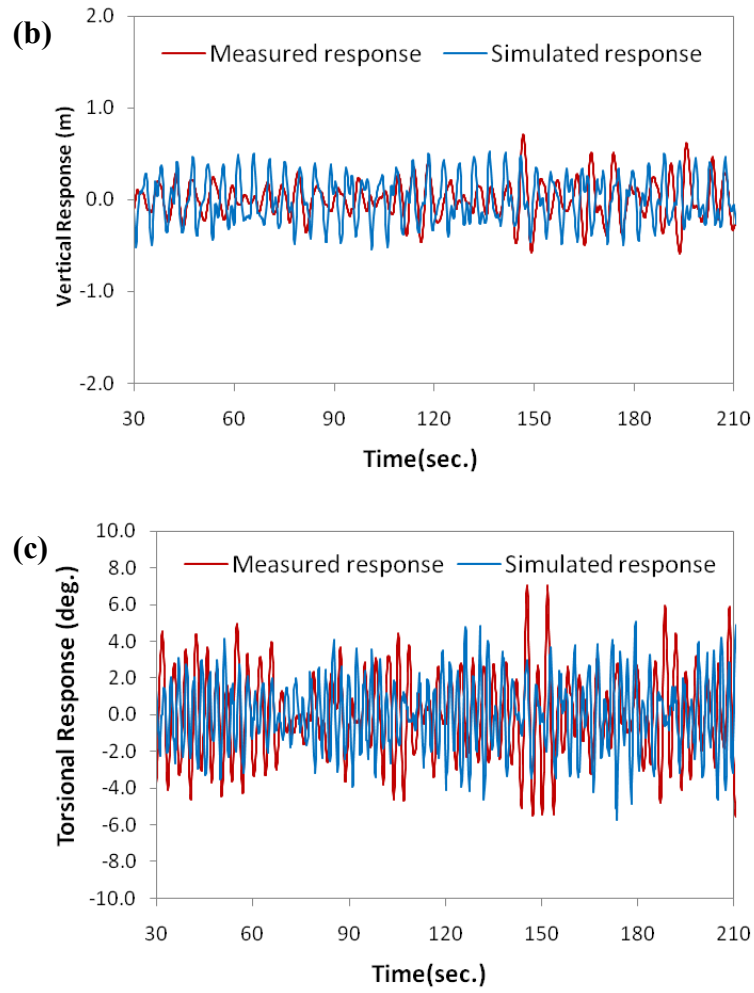


**Fig. 5.10:** Time series of response at mid-span.

### 5.5. Remark and future works

The time-domain gust-response analysis of the transmission lines is preliminarily studied. There are some remarks as follows.

To deal with the spatial wind-field simulation for all nodes of transmission line model of which the nodal coordinates change in the two dimensions, the grid of finite locations of the wind-time series that covers all of nodes of the conductor bundle is used. By doing so, the wind time series at any coordinate can be easily obtained. Additionally, the grid of nodal wind time series makes the advance NX Nastran solver become more convenient due to interpolating the coordinates of the structural and aerodynamic model.

FE model of the transmission lines associated model of the spatial wind is analyzed in NX Nastran computing software by using the basic solver, the “nonlinear-direct transient response analysis”. The simulated-response time series seem to be understandable. However, the basic solver is inconvenient for the aerodynamic analysis, especially for setting the damping matrix. Additionally, the structural node will change in time due to the continuously-movement of conductor in space leading change of the attacked angle as well as force coefficient. The aerodynamic response of the transmission line should be continued studying more in the future works with consideration of the advance NX Nastran Solver.

In fact, it is not easy to simulate exactly the spatial-wind that can induce the vibration response of the transmission lines as observed in the field. However, by using the time-domain gust-response analysis, the time-dependent characteristics of unsteady aerodynamic forces and nonlinearities of the both aerodynamic and structural origins can be taken into account in characterizing the large-amplitude gust response.

**References**

- Chen, X., Matsumoto, M., Kareem, A. (2000), "Time domain flutter and buffeting response analysis of bridges", *J. Engrg. Mech., ASCE* 126(1), pp. 7-16.
- FEMAP with NX Nastran. User guide. 2010
- Matsumoto, M., Chen, X., Shiraishi, H. (1994), "Buffeting analysis of long-span bridges with aerodynamic coupling", *Proc. 13th National Symposium on Wind Engineering, JAWE* pp. 227-232.
- Matsumoto, M., Chen, X. (1996), "Time domain analytical buffeting responses for long-span bridges", *Proc. 14th National Symposium on Wind Engineering, JAWE* pp. 515-520.
- Matsumoto, M., Shirato, H., Le, T.H. (2007), "Time and frequency domain gust response prediction using proper orthogonal decomposition", *The 12th Int'l Conference on Wind Engineering (ICWE12), Cairne Australia, July* pp. 1-6.
- Solari, G.; Carassale, L. (2000), "Modal transformation tools in structural dynamics and wind engineering", *Wind & Structures*, 3(4), pp. 221-241.
- Tamura, Y., Suganuma, S., Kikuchi, H., Hibi, K. (1999), "Proper orthogonal decomposition of random wind pressure field", *J. Fluid Struct.*, 13, pp. 1069-1095.
- ThaiHoa, L., (2009), Proper orthogonal decomposition and recent advanced topics in wind engineering, *VNU Journal of Science, Mathematics - Physics* 25, 21-38.
- Wang, H., Zong, Z., Li, A. (2012), Digital simulation of 3D turbulence wind field of Sutong Bridge based on measured wind spectra, *J Zhejiang Univ-Sci A (Appl Phys & Eng)* 13(2):91-104

## CHAPTER 6

### CONCLUSIONS

---

The full-scale measurements of the large-amplitude vibrations and their characterization by the extensive analysis of the enormous numbers of datasets are conducted in the different types of the transmission lines. The essential conclusions can be summarized as follows.

The field-measurements of wind-induced vibration and wind-field data in the three different types of the transmission lines enable the interpretation of the field-observed vibrations. The high turbulence intensities and the parabolic pattern of RMS response verses the mean wind velocity indicate the possibility of the observed vibrations as gust responses. Based on scattering of RMS response, the larger conductor bundle seems to be more stable than the other ones.

The results of eigenvalue and gust-response analyses give meaningful information in the identification of the field-measured events, in which the proper FE models of the transmission lines with their accurate static-equilibrium-configurations play an important role. A coupling between the similar-length spans pointed out that the span length affects significantly to the natural frequencies and mode shapes. In the conductor bundle, the type of spacer does not change much their torsional frequencies and model shapes.

The reasonable agreement of RMS between the gust-theory and the field responses as well as their PSDs confirms that most of the observed vibrations could be the gust response. The Buffeting theory is usable to different type of the bundled-conductor transmission lines. There might be a possibility of galloping phenomena in some cases and more vivid interpretation for identifying the galloping phenomenon is required in future.

For further interpretation about the large-amplitude gust response developed in time, the time-domain-gust analysis is considered. The significant feature of this approach is that the time-dependent characteristics of the unsteady-aerodynamic forces and nonlinearities of the both aerodynamic and structural origins can be taken into account in estimating the gust response. In future works, the results is expected to be improved for the design code or usable for controlling the large-amplitude vibration in order to avoid the phase-to-phase flashover that could lead to interrupt the electrical-power supply.

Based on the long-time observation at the site by TEPCO in the different type of the transmission line systems, the present analysis is a first extensive and intensive study on the causes of the recently field observed damages in the very long-span, large bundled-conductor transmission line systems. The most meaningful point of the researches is to confirm that the large-amplitude field-measured vibration is gust response. The gust responses can be sufficient large to cause the damages in the overhead transmission lines. The confirmation blasts the embroilments in the identification of vibration characteristics. The results may be a good reference for the design-code evaluation as well as the application of the vibration control to minimize the large-amplitude vibration.

# APPENDIX - A

## THEORY OF CATENARY EQUATION

In the following presentation, it is assumed that the self-weight of conductor distributed along its length; the cross-sectional area of the conductor is kept constant; The Cartesian coordinates of support points are  $(0, 0, 0)$  and  $(l_x, l_y, l_z)$ ; The Lagrangian coordinates of the un-deformed and deformed configuration are  $(s_0)$  and  $(s)$ , respectively.

### *A-1. In-extensible catenary equation*

In-extensible catenary is assumed that the conductor is perfectly flexible (zero bending stiffness,  $IE = 0$ ), in-extensible (very large axial stiffness,  $AE = \infty$ ), free of torsional rigidity and to be able to sustain only tensile forces. It means the in-extensible catenary has no elastic deformation. In order to derive catenary equation of in-extensible conductor, a segment of in-extensible catenary conductor is considered and shown in Fig. A.1.

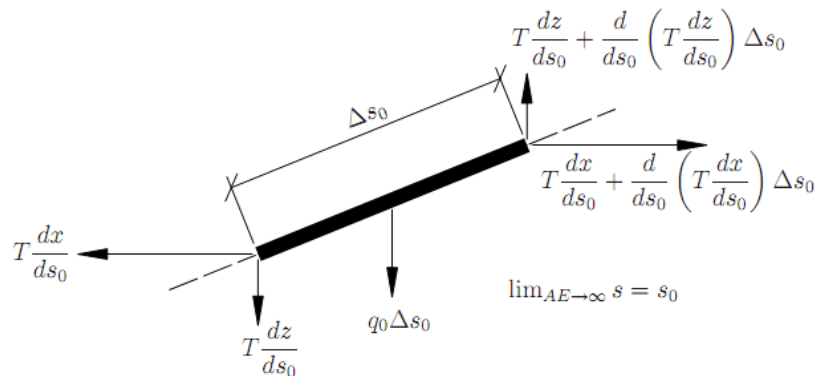


Fig. A.1. An in-extensible conductor segment.

Vertical equilibrium equations for conductor segment in Fig. A.1 can be written as follows.

$$\frac{d}{ds_0} \left( T \frac{dz}{ds_0} \right) = q_0 \quad (\text{A.1})$$

where  $s_0$  is un-deformed length ( $s$ = Lagrangian coordinate);  $q_0$  is conductor weight per unit length;  $T$  is tension in cable.

Horizontal equilibrium equations, similarly, is written as follows.

$$\frac{d}{ds_0} \left( T \frac{dx}{ds_0} \right) = 0 \quad (\text{A.2})$$

Integrating Eq. (A.2) yields:

$$T \frac{dx}{ds_0} = H \quad (\text{A.3})$$

where  $x$  and  $z$  are Castesian coordinates;  $H$  is the constant horizontal component of cable tension.

Substituting Eq. (A.3) into equation (A.1) results:

$$H \frac{d^2z}{dx^2} = q_0 \frac{ds_0}{dx} \quad (\text{A.4})$$

Rewriting Eq. (A.4) by using the geometric constraint of  $(dx)^2 + (dz)^2 = (ds)^2$  leads to

$$H \frac{d^2z}{dx^2} = q_0 \left( 1 + \left( \frac{dz}{dx} \right)^2 \right)^{1/2} \quad (\text{A.5})$$

The solution of Eq. (A.5) is the function of in-extensible catenary curve.

$$z = \frac{H}{q_0} \cosh\left(\frac{q_0}{H}x + C_1\right) + C_2 \quad (\text{A.6})$$

## A-2. Extensible catenary equation

A real conductor is extensible-type cable as it has a finite axial stiffness. The differential equations of equilibrium of a stretched conductor satisfy Hooke's law. It means that an extensible catenary will elongate when it is loaded (e.g. self-weight).

The equilibrium equations of the segment shown in Fig. A.2 in horizontal and vertical directions are written as follows.

Vertical equilibrium equation:

$$T \frac{dz}{ds} = H \quad (\text{A.7})$$

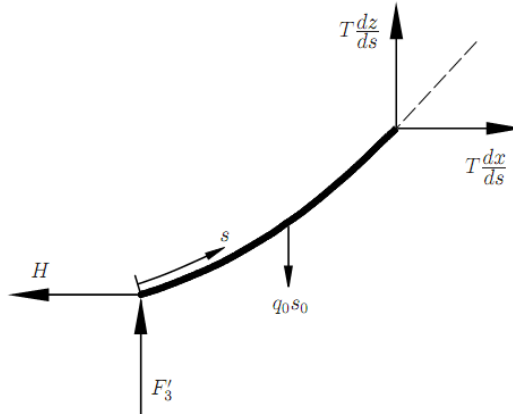


Fig. A.2. Extensible conductor segment.

Horizontal equilibrium equation:

$$T \frac{dx}{ds} = q_0 s_0 - F'_3 \quad (\text{A.8})$$

Finally, Eq. (A.7) and (A.8) are squared and substituted into geometric constraint equation of  $(dx)^2 + (dz)^2 = (ds)^2$  results.

$$T(s_0) = [H^2 + (q_0 s_0 - F_3)^2]^{1/2} \quad (\text{A.9})$$

It is assumed that “only axial normal tensile stress occurs along the conductor” and conductors behaves as a homogenous linearly elastic material that satisfy Hooke’s law.

$$T = AE \left( \frac{ds}{ds_0} - 1 \right) \quad (\text{A.10})$$

where AE is axial stiffness of conductor.

In other hand, a relationship of “s<sub>0</sub>” and “s” coordinate is expressed as follows.

$$\frac{dz}{ds_0} = \frac{dz}{ds} \frac{ds}{ds_0} \quad (\text{A.11})$$

$$\text{where } \frac{dz}{ds} = \frac{(q_0 s_0 - F_3)}{T} = \frac{q_0 s_0 - F_3}{\sqrt{H^2 + (q_0 s_0 - F_3)^2}} \quad (\text{From Eq. (A.8-9)}) \quad (\text{A.12})$$

$$\frac{ds}{ds_0} = \frac{1}{AE} \sqrt{H^2 + (q_0 s_0 - F_3)^2} + 1 \quad (\text{From Eq. (A.9-10)}) \quad (\text{A.13})$$

Solution of Eq. (A.11) is extensible catenary equation:

$$z = \frac{1}{AE} \left( \frac{q_0 s_0^2}{2} - F s_0 \right) + \frac{1}{q_0} \sqrt{H^2 + (q_0 s_0 - F_3)^2} + C \quad (\text{A.14})$$

Similarly, the following extensible catenary equation can be obtained.

$$x = \frac{H}{AE} s_0 + \frac{HL_0}{w} \cosh \left( \frac{q_0 s_0 - F_3}{H} \right) + C \quad (\text{A.15})$$

where  $w = q_0 L_0$ ;  $L_0$  is un-strained length of conductor;  $0 < s_0 < L_0$ .

# APPENDIX - **B**

## BUFFETING THEORY (DAVENPORT 1967)

Davenport's approach for determining the resonant dynamic responses of structures in particular modes under gusty wind summarized in Fig. B.1 is applied to the wind-induced vibrations of transmission lines.

From that point of view, the instantaneous wind velocity can be split into three components, the time average wind velocity, fluctuation wind velocity and structural motion induced velocity. Aerodynamic force per unit length acting on line-like structure at any instant of time is also assumed to be quasi static.

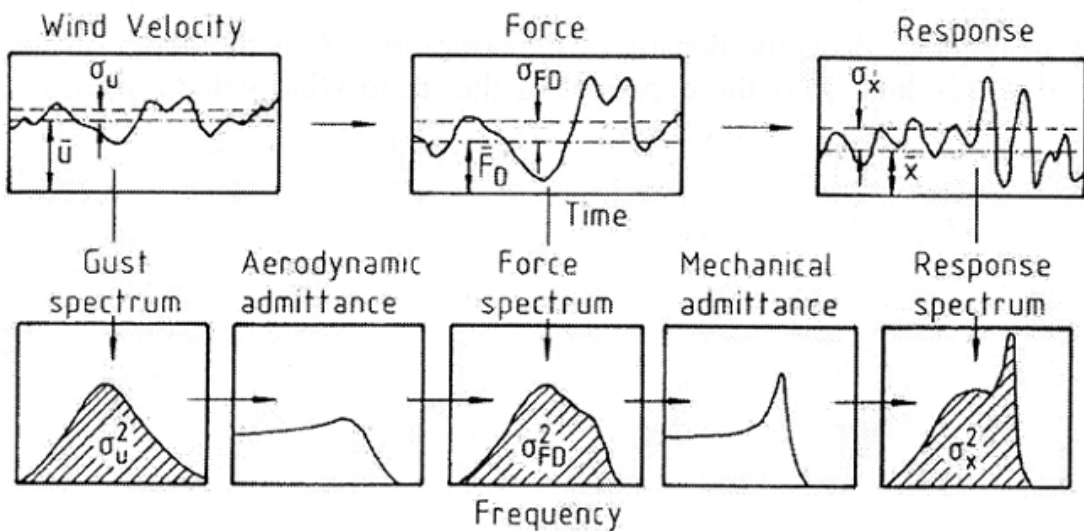


Fig. B.1. Davenport's approach for wind-induced resonant response (Davenport 1967)

Therefore, it is assumed that

$$q(x,t) = \frac{1}{2} \rho C_F U^2(t) \approx \frac{1}{2} \rho C_F \bar{U}^2 \left[ 1 + 2 \frac{u_F(t)}{\bar{U}} - 2 \frac{u_M(t)}{\bar{U}} \right] \quad (\text{B.1})$$

where the instantaneous wind velocity  $U(t)$  is the sum of the time average wind velocity  $\bar{U}$ , fluctuating component  $u_F(t)$  and structural motion induced component  $u_M(t)$ ; and where  $q(x,t)$ ,  $\rho$ ,  $C_F$  and  $x$  are, respectively, the instantaneous wind pressure, the air density, the aerodynamic shape coefficient and longitudinal coordinate of line-like structure. The terms involving high order parts  $u_F^2(t)$ ,  $u_M^2(t)$  etc. are assumed to be small and be omitted.

Consider an M-degree of freedom transmission line structure subjected to wind force, the equation of motion of in time domain is generally given by

$$\mathbf{M}\ddot{\mathbf{r}}(x,t) + \mathbf{C}\dot{\mathbf{r}}(x,t) + \mathbf{K}\mathbf{r}(x,t) = \mathbf{Q}(x,t) \quad (\text{B.2})$$

where  $\mathbf{r}(x,t)$ ,  $\mathbf{M}$ ,  $\mathbf{C}$ ,  $\mathbf{K}$ , and  $\mathbf{Q}(x,t)$  are displacement vector, mass matrix, damping matrix, stiffness matrix and dynamic force matrix, respectively.

By applying the principal transformation rule in Eq. (B.3)

$$\mathbf{r}(x,t) = \sum_{i=1}^N \boldsymbol{\varphi}_i(x) \boldsymbol{\eta}_i(t) \quad (\text{B.3})$$

and assuming that the structure has fundamental vibration modes, a time domain equilibrium equation of uncoupled-mode number  $i^{\text{th}}$  is generally given by

$$\ddot{\eta}_i(t) + 2\zeta_{S_i} (2\pi f_i) \dot{\eta}_i(t) + (2\pi f_i)^2 \eta_i(t) = \frac{1}{M_i} Q_i(x,t) \quad (\text{B.4})$$

where  $\boldsymbol{\varphi}_i(x)$ ;  $\boldsymbol{\eta}_i(t)$ ,  $Q_i(x,t)$ ,  $M_i$ ,  $m$ ,  $f_i$ ,  $\zeta_i$  and  $L$  are the natural eigen-mode, generalized coordinate, modal aerodynamic force, modal mass, mode shape, mass per unit length of structure, natural frequency, structural damping and length of structure, respectively.

Consider the meaningful part of wind force in Eq. (B.1), fluctuating wind force  $\mathbf{Q}_F(x,t)$  and its covariance between two space variables  $x_1$  and  $x_2$  is expressed, respectively, as follows (Stroman, 2006). The horizontal response is considered for example.

$$Q_{F_{yi}}(x, t) = \int_L \phi_{yi}(x) [\rho C_D D_c N_c \chi(f_{yi}) \bar{U} u_{F_{yi}}(x, t)] dx \quad (B.5)$$

$$\sigma_{Q_{yi}}^2 = \sigma_{u_f}^2 \frac{[\rho C_D D_c N_c \chi(f_i) \bar{U}]^2}{M_{yi}^2} \iint_L \phi_{yi}(x_1) \phi_{yi}(x_2) \rho_{u_f}(\Delta x, \tau) dx_1 dx_2 \quad (B.6)$$

where  $\rho$ ,  $C_D$ ,  $D_c$ ,  $N_c$ ,  $\chi(f_{yi})$ ,  $\bar{U}$ ,  $u_{F_{yi}}$ ,  $\phi_i(x)$ ,  $\rho_{u_f}(\Delta x, \tau) = \exp(\frac{-kf}{\bar{U}} \Delta x)$ ,  $k$  and  $L$  are the air density, the drag force coefficient, the conductor diameter, the number of conductor, the aerodynamic admittance, the mean wind velocity, the fluctuating wind velocity, the covariance coefficient,  $i^{\text{th}}$  mode shape, an empirical constant and the length of structure exposed to wind.

Aerodynamic admittance is a correction function. For low frequency, thin, lattice frame structure as transmission line conductors, aerodynamic admittance  $|\chi(f_i)|^2$  is variable and tends toward one. From Fig. B.2 (Liepmann et al., 1952), in the range of frequency of from 0.1 Hz to 0.5 Hz, the aerodynamic admittance is approximately equal to one.

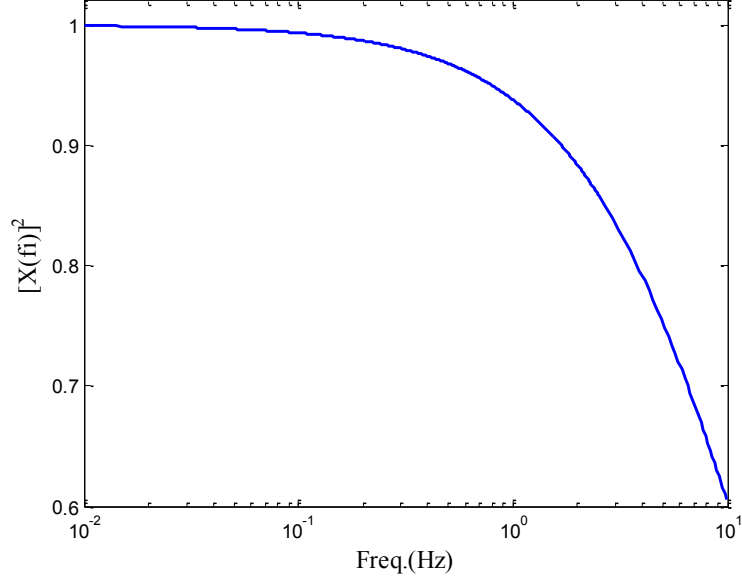


Fig. B.2. Aerodynamic admittance function

In fact, the mean square of any quantity is equal to area under spectral curve of that quantity. Therefore, the fluctuating wind force, the structure response, and the principal transformation, respectively, can be performed in the frequency domain as follows

$$S_{Q_{yi}}(f) = S_u(f) \left[ \rho C_D D_c N_c L \bar{U} \right]^2 \frac{1}{M_{yi}^2} |j_y(f)|^2 \quad (\text{B.7})$$

$$S_{\eta_y}(f) = |H_y(f)|^2 S_{Q_{yi}}(f) \quad (\text{B.8})$$

$$S_{ry}(f) = \sum_I^N \phi_{yi}^2 S_{\eta_y}(f) \quad (\text{B.9})$$

where  $|j_y(f)|^2 = \int \int_{L \ L} \rho_{u_F}(\Delta x, \tau) \phi_{yi}(\pi x_1) \phi_{yi}(\pi x_2) dx_1 dx_2$ ,  $\sigma_{Q_{yi}}^2 = \int_0^\infty S_{Q_{yi}}(f) df$ ,  $\sigma_{u_F}^2 = \int_0^\infty S_{u_F}(f) df$  are joint acceptance function, mean square of fluctuation wind force and mean square of fluctuation wind velocity.  $k$  is an empirical constant used to fit measured data.

Substituting Eq. (B.7) and (B.8) into Eq. (B.9), the response spectrum  $S_{ry}(f)$  can be calculated from the gust spectrum  $S_u(f)$  as follows

$$S_{ry}(f) = S_u(f) \times \left[ \rho C_D D_c N_c L \bar{U} \right]^2 \sum_I^N \frac{\phi_{yi}^2}{M_{yi}^2} |x(f_i)|^2 |j_y(f)|^2 |H_y(f)|^2 \quad (\text{B.10})$$

where  $|H(f)|^2 = \frac{1}{(2\pi f_i)^2} \left\{ \left[ 1 - (f/f_i)^2 \right]^2 + \left[ 2\zeta_i (f/f_i) \right]^2 \right\}^{-1}$ ,  $S_u(f) = FFT[u(t)]$  are the mechanical admittance function and the gust spectra obtained by taking the Fast Fourier Transform of gust time series.  $f_i$  is natural frequency of  $i^{th}$  mode;  $\zeta_i$  is sum of structure and aerodynamic damping for  $i^{th}$  mode.

Mechanical admittance is frequency transfer function. Transfer function depends much on natural frequencies, mode shapes and damping (generalized structural damping + generalized aerodynamic damping). Estimation of such damping also creates uncertainties. Fig. B.3 shows mechanical admittance for single mode-single component of 0.1 Hz mode.

By using Eq. (B.10), the power spectral density of response based on Davenport's buffeting theory can be obtained. Eq. (B.10) is derived by neglecting both the aerodynamic interaction among conductors in a conductor bundled-and the lift force on individual conductor. The first assumption is plausible because the separation between two conductors is

larger than 10 conductor diameters (Zhang Q. et al., 2000) and the second assumption can be justified by conductor's circular shape in absence of ice.

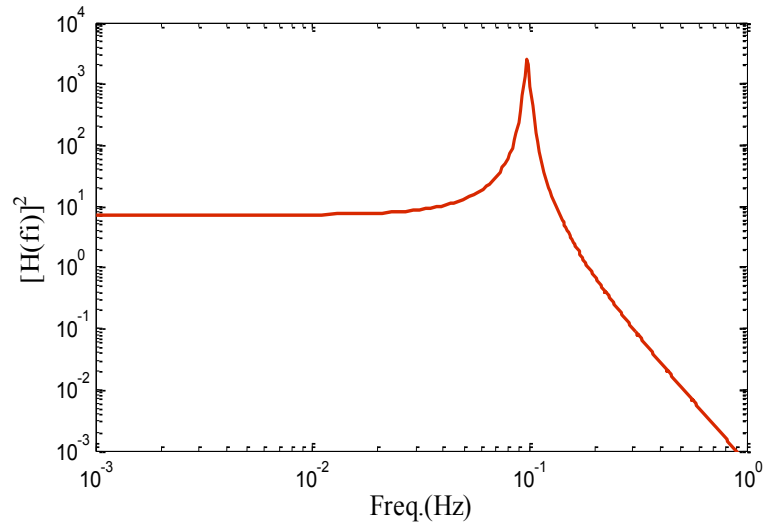


Fig. B.3. Mechanical admittance for single mode-single component of 0.1 Hz mode

# APPENDIX - C

## THEORY OF TIME DOMAIN GUST RESPONSE ANALYSIS IN

### C-1. Modal response analysis

Multi-DOF motion equations of transmission line conductor subjected to the buffeting forces is expressed:

$$\mathbf{M}\ddot{\mathbf{u}}(x,t) + \mathbf{C}\dot{\mathbf{u}}(x,t) + \mathbf{K}\mathbf{u}(x,t) = \mathbf{F}_b(t) \quad (\text{C.1})$$

where  $\mathbf{u}(x,t)$ ,  $\dot{\mathbf{u}}(x,t)$ ,  $\ddot{\mathbf{u}}(x,t)$  are deflection and its first, second order derivatives;  $\mathbf{M}$ ,  $\mathbf{C}$ ,  $\mathbf{K}$  are mass, damping, stiffness matrices;  $\mathbf{F}_b(t)$  is full-scale buffeting forces.

Decomposing into the modal space using the mass matrix-based normalized structural modal transformation as  $\mathbf{u} = \Phi \xi \approx \sum_{i=1}^M \phi_i \xi_i$ , single-DOF motion equation in the  $i^{\text{th}}$  generalized structural coordinate due to the generalized buffeting forces can be obtained:

$$\ddot{\xi}_i + 2\zeta_i \omega_i \dot{\xi}_i + \omega_i^2 \xi_i = \phi_i^T F_b(t) \quad (\text{C.2})$$

where  $\Phi = [\phi_1, \phi_2, \phi_3, \dots, \phi_M]$ ;  $\omega_i, \zeta_i, M$  are circular frequency, damping ratio and number of truncated structural mode.

The uniform turbulent-induced forces (buffeting forces) are expressed due to the quasi-steady theory corrected by frequency-dependant admittance functions as follows.

$$\begin{aligned} L_b(t) &= \frac{1}{2} \rho U^2 d_c n_c \left[ C_L \chi_{L_u}(f) \frac{2u(t)}{U} + (C'_L + C_D) \chi_{L_w}(f) \frac{w(t)}{U} \right] \\ D_b(t) &= \frac{1}{2} \rho U^2 d_c n_c \left[ C_D \chi_{D_u}(f) \frac{2u(t)}{U} + (C'_D - C_L) \chi_{D_w}(f) \frac{w(t)}{U} \right] \end{aligned} \quad (\text{C.3.a, b, c})$$

$$M_b(t) = \frac{1}{2} \rho U^2 (d_c n_c)^2 \left[ C_M \chi_{Mu}(f) \frac{2u(t)}{U} + C'_M \chi_{Mw}(f) \frac{w(t)}{U} \right]$$

where  $C_L, C_D, C_M$  are aerodynamic coefficients at balanced angle;  $C'_L, C'_D, C'_M$  are first-order derivatives with respect to angle of attack;  $d_c, n_c$  are diameter of bundle-conductor and number of bundle-conductor;  $\chi_{Fv}(F=L, D, M; v=u, w)$  is aerodynamic transfer functions between turbulent components and forces.

Accordingly, full-scale buffeting forces can be obtained due to a linearized force distribution as follows.

$$F_b(t) = \frac{1}{2} \rho U d_c n_c [C_u \chi_{Fu}(f) u(t) + C_w \chi_{Fw}(f) w(t)] \quad (C.4)$$

where  $C_u, C_w$  are full-scale force coefficient matrices.

The covariance matrix-based orthogonal vectors are found as the eigenvector solutions of the zero-time-lag covariance matrix  $C_v(f)$  of the N-variate random turbulent field  $v(t)$ :

$$C_v \Theta_v = \Gamma_v \Theta_v \quad (C.5)$$

where  $\Theta_v = [\theta_{v1}, \theta_{v2}, \theta_{v3}, \dots, \theta_{vN}]$  and  $\Gamma_v = \text{diag}(\gamma_{v1}, \gamma_{v2}, \gamma_{v3}, \dots, \gamma_{vN})$  are covariance eigenvalue and eigenvector (turbulent mode) matrices, which satisfy the orthonormal conditions:

$$\Theta_v \Theta_v^T = I; \Theta_v C_v \Theta_v^T = \Gamma_v \quad (C.6)$$

Accordingly, the turbulence field and its covariance matrix can be expressed due to the covariance proper transformation as summed approximation as follows:

$$u(t) \approx \tilde{u}(t) = \Theta_u \tilde{x}_u(t) = \sum_{j=1}^{\tilde{M}} \theta_{uj} \tilde{x}_{uj}(t); \quad w(t) \approx \tilde{w}(t) = \Theta_w \tilde{x}_w(t) = \sum_{j=1}^{\tilde{M}} \theta_{wj} \tilde{x}_{wj}(t) \quad (C.7)$$

$$C_u = \Theta_u \Gamma_u \Theta_u^T(f) \approx \sum_{j=1}^{\tilde{M}} \theta_{uj} \gamma_{uj} \theta_{uj}^T; \quad C_w = \Theta_w \Gamma_w \Theta_w^T(f) \approx \sum_{j=1}^{\tilde{M}} \theta_{wj} \gamma_{wj} \theta_{wj}^T \quad (C.8)$$

where  $\tilde{x}_v(t) = \{\tilde{x}_{v1}(t), \tilde{x}_{v2}(t), \tilde{x}_{v3}(t), \dots, \tilde{x}_{v\tilde{M}}(t)\}$  are covariance-based turbulent principal coordinates as the N-variate uncorrelated Gaussian random process;  $\tilde{M}$  is number of truncated turbulent modes ( $\tilde{M} < N$ ); Covariance principal coordinates can be determined from observed data:

$$\tilde{v}(t) = \Theta_v^{-1} v(t) = v(t) \Theta_v = \sum_{i=1}^N v_i(t) \theta_{vi}$$

(C.9)

The full-scale buffeting forces in Eq. (C.4) are presented in which the two N-variate turbulent processes  $u(t)$ ,  $w(t)$  are decomposed into uncorrelated turbulent principal coordinates using the covariance proper transformation as Eq. (C.7). The single-DOF motion Eq. (C.2) is rewritten:

$$\ddot{\xi}_i(t) + 2\zeta_i \omega_i \dot{\xi}_i(t) + \omega_i^2 \xi_i(t) \approx \frac{1}{2} \rho U d_c n_c \left[ \phi_i^T C_u \sum_{j=1}^{\tilde{M}} \theta_{uj} \tilde{x}_{uj}(t) + \phi_i^T C_w \sum_{j=1}^{\tilde{M}} \theta_{wj} \tilde{x}_{wj}(t) \right] \quad (C.10)$$

where  $\sum_{j=1}^{\tilde{M}} \phi_i^T C_u \theta_{uj}$  and  $\sum_{j=1}^{\tilde{M}} \phi_i^T C_w \theta_{wj}$  are cross modal coefficient matrices accounting for interrelation between the turbulent modes and the structural modes.

Time series and its derivatives of the generalized responses can be obtained by using methods such as the Newton- $\beta$ . Finally, the global responses are determined.

## C-2. Direct response analysis

In direct response analysis, structural response is computed by solving a set of coupled equations using direct numerical integration. Beginning with the dynamic equation of motion in matrix form as shown in Eq. C.1, the fundamental structural response (displacement) is solved at discrete times, typically with a fixed integration time step  $\Delta t$ . By using a central finite difference representation for the velocity  $\dot{u}(x,t)$  and the acceleration  $\ddot{u}(x,t)$  at discrete time as Eq. (C.11) and averaging the applied force over three adjacent time points, the equation of motion can be rewritten as Eq. (C.12).

$$\{ \dot{u}_n \} = \frac{1}{2\Delta t} \{ u_{n+1} - u_{n-1} \} \quad (C.11)$$

$$\{ \ddot{u}_n \} = \frac{1}{\Delta t^2} \{ u_{n+1} - 2u_n + u_{n-1} \}$$

$$[A_1] \{ u_{n+1} \} = [A_2] + [A_3] \{ u_n \} + [A_4] \{ u_{n-1} \} \quad (C.12)$$

where  $[A_1] = \left[ \frac{M}{\Delta t^2} + \frac{C}{2\Delta t} + \frac{K}{3} \right]$

$$[A_2] = \frac{1}{3} \{P_{n+1} + P_n + P_{n-1}\}$$

$$[A_3] = \left[ \frac{2M}{\Delta t^2} - \frac{K}{3} \right]$$

$$[A_4] = \left[ -\frac{M}{\Delta t^2} + \frac{C}{2\Delta t} - \frac{K}{3} \right]$$

Matrix  $[A_1]$  is termed the dynamic matrix, and  $[A_2]$  is the applied force. This approach is similar to the classical Newmark-Beta direct integration method.

A significant benefit presents itself if  $\Delta t$  remains constant during the analysis. With a constant  $\Delta t$ , the  $[A_1]$  matrix needs to be decomposed only once. If  $\Delta t$  is changed,  $[A_1]$  must be re-decomposed, which can be a costly operation in large problems.

Efficiency in the direct solution is that the output time interval may be greater than the solution time interval. In many cases it is not necessary to sample output response at each solution time.

# APPENDIX -D

## DETAILS OF FIELD MEASURED DATA

Table D.1 Data for Line A Midpoint

Data No.	Date	End Time	Peak-to-Peak Response			Unorm (m/s)	Iu	Iv
			H(m)	V(m)	T(deg)			
1	7-Mar-09	1:14	0.581	0.374	7.816	11.5	0.186	0.097
2	7-Mar-09	1:59	0.764	0.578	8.642	12.7	0.154	0.088
3	7-Mar-09	2:29	0.461	0.734	7.340	11.3	0.198	0.089
4	7-Mar-09	2:54	1.196	1.027	7.353	14.4	0.166	0.088
5	7-Mar-09	3:14	1.315	0.605	9.795	14.6	0.133	0.077
6	7-Mar-09	3:44	0.960	0.821	11.758	15.0	0.152	0.079
7	7-Mar-09	4:19	0.783	0.668	7.733	14.0	0.101	0.063
8	7-Mar-09	4:54	0.543	0.496	5.793	10.1	0.202	0.105
9	7-Mar-09	5:44	0.719	0.433	7.693	10.6	0.167	0.118
10	7-Mar-09	6:19	0.807	0.556	8.913	11.8	0.166	0.090
11	7-Mar-09	6:49	0.435	0.429	5.585	12.0	0.153	0.084
12	7-Mar-09	8:34	0.741	0.826	7.994	10.6	0.240	0.137
13	7-Mar-09	9:04	0.596	0.446	5.431	9.5	0.229	0.141
14	7-Mar-09	9:39	1.214	0.859	8.477	13.6	0.161	0.090
15	7-Mar-09	9:59	0.758	0.640	8.614	13.2	0.190	0.102
16	7-Mar-09	10:29	0.852	0.862	8.393	12.3	0.165	0.109
17	7-Mar-09	10:49	0.712	0.527	7.100	12.3	0.184	0.080
18	7-Mar-09	11:44	0.523	0.521	7.130	11.0	0.162	0.101
19	7-Mar-09	12:29	0.609	0.404	7.672	10.7	0.202	0.098
20	7-Mar-09	16:29	0.539	0.488	7.062	10.3	0.171	0.092
21	10-Mar-09	14:18	0.486	0.428	6.057	9.1	0.206	0.112
22	10-Mar-09	15:32	0.589	0.496	6.465	9.0	0.238	0.114
23	10-Mar-09	16:02	0.536	0.468	8.242	10.9	0.161	0.083
24	10-Mar-09	20:37	0.832	0.564	6.931	11.0	0.147	0.085
25	11-Mar-09	5:27	0.531	0.367	7.994	8.8	0.217	0.109
26	11-Mar-09	9:07	0.513	0.590	9.199	8.0	0.204	0.129
27	11-Mar-09	9:57	0.668	0.445	8.191	10.1	0.204	0.108
28	11-Mar-09	10:57	0.698	0.358	5.986	9.8	0.171	0.103

Table D.2 Data for Line A Quarter point

Data No.	Date	End Time	Peak-to-Peak Response			Unorm (m/s)	Iu	Iv
			H(m)	V(m)	T(deg)			
1	7-Mar-09	3:09	1.167	0.809	7.125	14.6	0.16	0.082
2	7-Mar-09	3:29	0.630	0.692	6.218	13.2	0.176	0.09
3	7-Mar-09	3:54	0.745	0.709	5.899	14.3	0.174	0.083
4	7-Mar-09	10:39	0.885	0.647	9.721	13.0	0.177	0.086
5	10 Mar 09	12:49	0.625	0.483	4.379	11.9	0.137	0.089

36	27-Apr-09	13:23	0.493	0.471	4.013	11.8	0.158	0.106
37	14-May-09	18:21	0.992	1.208	6.615	14.4	0.207	0.109
38	14-May-09	20:41	1.619	1.534	9.807	19.4	0.147	0.081
39	14-May-09	21:06	1.279	1.031	7.525	13.8	0.225	0.109
40	14-May-09	23:11	0.508	0.486	3.318	9.5	0.241	0.173
41	22-May-09	10:40	0.529	0.598	4.887	13.5	0.182	0.086

Table D.3 Data for Line b Midpoint (1st span)

Data No.	Date	End Time	Peak-to-Peak Response			Unorm (m/s)	Iu	Iv
			H(m)	V(m)	T(deg)			
1	31-Dec-08	5:36	0.974	0.618	8.430	7.0	0.376	0.233
2	31-Dec-08	7:06	1.022	1.131	13.777	10.5	0.328	0.212
3	31-Dec-08	7:56	1.227	1.213	11.372	9.2	0.328	0.207
4	31-Dec-08	8:21	0.994	0.753	8.428	8.6	0.302	0.185
5	31-Dec-08	8:46	1.423	1.238	12.820	10.1	0.284	0.188
6	31-Dec-08	9:06	1.056	0.722	13.227	9.8	0.308	0.209
7	31-Dec-08	9:51	1.314	0.818	13.871	8.6	0.350	0.262
8	31-Dec-08	10:26	1.698	0.821	12.193	6.8	0.407	0.282
9	31-Dec-08	20:31	1.287	0.832	14.660	7.3	0.433	0.244
10	31-Dec-08	20:56	1.536	0.695	12.253	8.1	0.266	0.207
11	3-Jan-09	18:29	0.999	0.885	8.890	7.5	0.416	0.250
12	3-Jan-09	19:04	1.412	0.842	9.786	5.1	0.561	0.325
13	3-Jan-09	22:04	1.239	1.118	12.464	6.7	0.391	0.210
14	3-Jan-09	22:24	1.123	0.836	10.273	7.8	0.329	0.228
15	4-Jan-09	0:04	0.997	0.849	7.447	7.4	0.348	0.207
16	4-Jan-09	0:24	1.263	0.735	14.184	7.1	0.341	0.235
17	4-Jan-09	0:44	1.306	0.926	13.171	7.2	0.394	0.217
18	4-Jan-09	1:24	2.125	1.049	10.863	9.0	0.341	0.215
19	4-Jan-09	1:54	1.857	0.941	10.536	6.6	0.411	0.317
20	10-Jan-09	8:04	1.735	1.060	16.682	12.8	0.357	0.209
21	10-Jan-09	9:19	2.613	1.366	14.366	15.2	0.282	0.187
22	10-Jan-09	9:54	2.366	1.816	24.521	14.6	0.314	0.202
23	10-Jan-09	10:29	2.162	1.921	18.925	11.5	0.404	0.262
24	10-Jan-09	11:39	2.803	2.126	24.628	14.7	0.334	0.216
25	10-Jan-09	12:39	2.502	1.920	20.594	18.2	0.239	0.160
26	10-Jan-09	12:59	1.908	1.362	18.662	14.4	0.306	0.199
27	10-Jan-09	15:14	2.077	1.459	18.239	14.1	0.348	0.221
28	10-Jan-09	16:19	2.275	2.737	20.164	10.0	0.490	0.288
29	10-Jan-09	16:39	3.126	1.375	24.182	8.8	0.470	0.318
30	10-Jan-09	17:09	4.108	1.961	17.178	9.2	0.467	0.312
31	10-Jan-09	17:29	2.387	1.179	22.074	10.5	0.429	0.260
32	10-Jan-09	17:49	2.774	1.820	28.071	16.9	0.261	0.197
33	10-Jan-09	18:09	3.141	2.151	22.327	13.6	0.357	0.205
34	10-Jan-09	18:59	3.260	2.013	29.061	8.7	0.432	0.265
35	10-Jan-09	19:29	4.621	2.312	24.221	8.9	0.446	0.295
36	10-Jan-09	20:19	2.404	1.597	27.420	14.6	0.357	0.247
37	10-Jan-09	22:09	1.446	0.820	11.512	6.6	0.578	0.325
38	10-Jan-09	22:39	1.978	1.115	14.115	7.1	0.594	0.378
39	10-Jan-09	22:59	2.453	1.460	24.465	9.6	0.513	0.329
40	11-Jan-09	3:09	1.879	0.993	13.435	9.3	0.396	0.265

86	14-May-09	20:20	3.284	3.400	23.794	17.7	0.334	0.210
87	14-May-09	21:00	3.358	1.991	29.068	21.6	0.237	0.143
88	14-May-09	22:05	2.265	1.546	29.668	20.9	0.259	0.170

Table D.4 Data for Line b Quarter point (1st span)

Data No.	Date	End Time	Peak-to-Peak Response			Unorm (m/s)	Iu	Iv
			H(m)	V(m)	T(deg)			
1	26-Dec-08	3:05	1.167	0.577	9.205	10.8	0.273	0.198
2	26-Dec-08	6:40	1.304	0.954	9.441	7.9	0.379	0.290
3	26-Dec-08	21:05	0.695	0.918	8.756	7.5	0.454	0.204
4	26-Dec-08	22:10	1.268	1.426	10.608	9.2	0.390	0.241
5	26-Dec-08	23:20	1.179	0.890	10.288	6.1	0.529	0.305
6	27-Dec-08	0:00	1.523	1.405	12.418	6.9	0.476	0.286
7	27-Dec-08	0:40	1.346	0.988	8.712	7.4	0.457	0.233
8	27-Dec-08	3:25	2.854	1.558	15.677	10.7	0.383	0.253
9	27-Dec-08	11:25	1.400	1.043	12.145	6.3	0.406	0.203
10	27-Dec-08	13:40	1.310	1.149	8.888	7.6	0.393	0.257
11	27-Dec-08	14:00	1.981	1.178	11.030	8.6	0.427	0.270
12	27-Dec-08	14:45	1.050	0.880	11.876	7.5	0.435	0.254
13	27-Dec-08	15:35	0.909	1.012	9.515	6.1	0.441	0.267
14	27-Dec-08	16:00	1.735	1.512	11.846	6.5	0.513	0.248
15	27-Dec-08	17:10	1.540	1.219	11.428	5.9	0.412	0.243
16	28-Dec-08	14:15	1.388	1.090	9.184	5.7	0.451	0.245
17	28-Dec-08	15:10	0.902	0.999	8.510	5.0	0.439	0.260
18	28-Dec-08	15:35	1.424	1.330	13.630	5.1	0.414	0.308
19	28-Dec-08	16:05	2.098	1.564	13.497	5.8	0.440	0.271
20	28-Dec-08	16:25	1.269	0.818	13.474	6.5	0.411	0.237
21	28-Dec-08	17:00	1.151	0.818	9.031	6.2	0.392	0.272
22	28-Dec-08	17:20	1.987	1.304	16.613	7.1	0.468	0.252
23	28-Dec-08	18:00	1.931	1.716	15.754	7.5	0.468	0.294
24	28-Dec-08	18:20	2.906	2.396	19.576	6.9	0.404	0.286
25	28-Dec-08	21:05	1.643	1.640	13.009	7.7	0.554	0.277
26	28-Dec-08	21:25	3.316	1.342	12.665	8.4	0.490	0.289
27	28-Dec-08	22:20	1.774	1.380	15.301	9.3	0.533	0.271
28	28-Dec-08	23:00	2.688	2.134	14.937	9.2	0.382	0.287
29	28-Dec-08	23:25	3.105	2.409	16.844	12.0	0.358	0.263
30	28-Dec-08	23:45	2.917	1.818	16.090	9.4	0.342	0.267
31	29-Dec-08	0:05	1.865	2.241	15.691	9.0	0.466	0.245
32	29-Dec-08	0:40	1.752	1.695	17.954	8.5	0.383	0.226
33	29-Dec-08	1:00	2.250	1.837	14.484	9.9	0.398	0.245
34	29-Dec-08	1:35	2.220	2.567	18.646	10.4	0.363	0.200
35	29-Dec-08	2:25	1.884	2.003	18.913	8.8	0.353	0.248
36	29-Dec-08	2:45	2.081	1.322	15.217	10.2	0.314	0.197
37	29-Dec-08	3:05	2.757	1.743	15.528	10.4	0.353	0.223

128	21-Feb-09	14:29	1.330	1.423	10.126	5.8	0.442	0.268
129	2-Mar-09	10:18	1.600	1.264	12.981	9.3	0.386	0.278
130	2-Mar-09	13:08	1.557	1.144	15.358	9.6	0.384	0.271
131	11-Mar-09	4:52	1.909	1.785	14.482	8.7	0.440	0.322
132	11-Mar-09	5:17	1.601	1.424	15.073	9.5	0.424	0.267
133	12-Mar-09	7:17	3.395	1.780	17.812	19.3	0.210	0.132
134	12-Mar-09	8:22	2.021	1.155	18.596	18.5	0.215	0.146
135	21-Mar-09	2:41	2.348	1.723	20.307	13.1	0.240	0.173
136	21-Mar-09	3:36	2.368	1.766	17.908	16.4	0.239	0.175
137	21-Mar-09	5:31	1.940	2.417	19.198	17.9	0.224	0.156
138	21-Mar-09	6:06	2.037	1.412	15.054	16.4	0.211	0.185
139	23-Mar-09	2:41	1.907	1.401	23.655	10.1	0.373	0.262
140	23-Mar-09	3:06	2.408	2.105	21.575	9.6	0.335	0.217
141	23-Mar-09	4:01	3.497	2.532	24.718	12.4	0.484	0.295
142	23-Mar-09	5:21	3.919	2.439	21.701	9.0	0.476	0.322
143	23-Mar-09	6:01	2.736	2.283	18.072	8.5	0.503	0.348
144	23-Mar-09	6:56	2.961	2.417	29.474	11.3	0.435	0.305
145	23-Mar-09	7:36	3.354	2.206	22.254	13.7	0.361	0.211
146	23-Mar-09	8:01	3.161	2.949	20.667	15.0	0.325	0.191
147	23-Mar-09	8:21	2.512	1.881	20.158	14.2	0.279	0.210
148	23-Mar-09	9:36	2.578	1.911	19.907	9.6	0.498	0.301
149	2-Apr-09	6:50	1.853	1.667	17.381	17.3	0.240	0.157
150	2-Apr-09	7:15	1.942	1.172	22.189	17.3	0.230	0.154
151	2-Apr-09	8:30	2.867	2.141	17.338	18.9	0.246	0.160
152	2-Apr-09	9:20	3.437	1.817	16.597	15.1	0.336	0.218
153	2-Apr-09	9:45	2.276	1.564	17.329	15.0	0.370	0.203
154	2-Apr-09	10:20	3.055	2.119	21.187	15.1	0.349	0.229
155	2-Apr-09	10:50	2.625	1.690	17.392	10.3	0.520	0.282
156	2-Apr-09	13:30	2.027	1.793	12.535	10.2	0.414	0.276
157	14-May-09	19:41	3.657	2.543	25.142	17.9	0.258	0.165
158	14-May-09	20:06	3.726	5.013	31.492	18.2	0.283	0.212
159	14-May-09	20:26	3.431	2.755	32.372	17.9	0.316	0.207
160	14-May-09	20:51	3.512	3.244	27.257	21.6	0.222	0.157
161	14-May-09	21:11	3.374	1.935	26.333	22.5	0.214	0.144
162	14-May-09	21:36	2.984	2.591	31.787	20.7	0.222	0.179
163	14-May-09	21:56	4.046	3.173	26.202	21.1	0.229	0.165
164	14-May-09	22:21	2.986	2.069	27.457	18.7	0.247	0.199
165	14-May-09	22:41	2.248	2.582	24.563	16.2	0.296	0.221
166	14-May-09	23:16	1.905	2.047	17.663	12.2	0.415	0.306

Table D.5 Data for Line b Quarter point (2nd span)

Data No.	Date	End Time	Peak-to-Peak Response			Unorm (m/s)	Iu	Iv
1	27-Dec-08	2:45	1.693	0.789	11.199	12.2	0.394	0.259

Table D.6 Data for Line b Midpoint (2nd span)

Data No.	Date	End Time	Peak-to-Peak Response			Unorm (m/s)	Iu	Iv
			H(m)	V(m)	T(deg)			
1	26-Dec-08	22:12	1.338	0.615	22.869	9.4	0.368	0.255
2	27-Dec-08	3:17	5.103	1.477	36.497	12.2	0.345	0.240
3	27-Dec-08	16:32	2.492	0.600	27.785	8.6	0.445	0.265
4	28-Dec-08	17:02	2.229	0.765	16.224	7.4	0.380	0.284
5	28-Dec-08	18:27	1.963	0.810	36.971	7.3	0.386	0.293
6	28-Dec-08	21:02	3.310	1.103	24.658	8.4	0.511	0.283
7	28-Dec-08	21:27	4.155	1.286	27.329	9.7	0.473	0.281
8	28-Dec-08	23:27	3.170	1.238	43.281	12.5	0.377	0.265
9	28-Dec-08	23:47	2.253	0.968	31.395	10.5	0.325	0.271
10	29-Dec-08	0:27	2.080	0.773	49.961	10.1	0.402	0.298
11	29-Dec-08	0:52	3.430	1.512	51.463	12.7	0.372	0.244
12	29-Dec-08	1:27	3.380	1.304	35.173	11.6	0.361	0.253
13	29-Dec-08	1:52	4.239	1.054	47.611	10.5	0.411	0.247
14	29-Dec-08	2:47	2.675	0.919	25.133	11.8	0.301	0.188
15	29-Dec-08	3:12	3.331	1.969	28.488	12.0	0.368	0.216
16	29-Dec-08	3:32	3.901	1.652	34.109	11.6	0.384	0.245
17	29-Dec-08	3:52	2.912	1.135	34.218	12.8	0.349	0.231
18	29-Dec-08	4:37	2.447	0.880	42.178	11.2	0.425	0.307
19	31-Dec-08	10:07	2.894	0.856	29.629	10.0	0.419	0.284
20	3-Jan-09	22:21	1.756	0.496	18.253	9.9	0.292	0.189
21	10-Jan-09	7:21	1.969	0.516	23.213	10.1	0.321	0.246
22	10-Jan-09	7:41	2.611	0.872	19.932	10.3	0.581	0.316
23	10-Jan-09	8:21	4.743	1.697	31.401	13.9	0.338	0.216
24	10-Jan-09	8:46	3.206	2.023	54.791	17.2	0.262	0.186
25	10-Jan-09	9:06	4.005	1.701	33.226	17.4	0.281	0.172
26	10-Jan-09	9:31	3.795	0.938	39.055	12.9	0.362	0.246
27	10-Jan-09	9:56	3.609	1.265	40.258	15.6	0.322	0.201
28	10-Jan-09	10:16	2.330	1.055	36.827	10.9	0.447	0.286
29	10-Jan-09	10:36	4.640	1.701	38.115	13.7	0.390	0.223
30	10-Jan-09	11:01	4.880	2.170	63.878	15.3	0.296	0.192
31	10-Jan-09	11:31	2.718	1.377	52.333	14.3	0.380	0.238
32	10-Jan-09	11:56	6.140	3.161	37.360	14.3	0.342	0.226
33	10-Jan-09	12:21	3.775	2.422	43.889	15.2	0.281	0.192
34	10-Jan-09	12:41	4.509	2.173	43.229	18.2	0.263	0.172
35	10-Jan-09	14:31	4.278	0.864	38.891	10.4	0.423	0.305
36	10-Jan-09	14:51	2.842	1.456	38.038	13.7	0.356	0.235
37	10-Jan-09	15:25	4.155	2.032	31.598	16.0	0.310	0.195
38	10-Jan-09	15:50	5.929	2.620	34.719	13.3	0.385	0.243
39	10-Jan-09	16:30	3.041	0.946	40.583	11.7	0.447	0.301
40	10-Jan-09	17:50	4.856	2.406	50.553	17.7	0.263	0.198

131	2-Apr-09	7:11	5.551	2.572	29.528	18.6	0.235	0.158
132	2-Apr-09	8:01	2.273	1.088	30.349	14.2	0.343	0.221
133	2-Apr-09	8:26	4.241	1.465	32.857	17.7	0.287	0.175
134	2-Apr-09	8:51	3.623	1.295	39.183	15.5	0.318	0.202
135	2-Apr-09	9:11	4.441	0.944	31.887	14.1	0.405	0.228
136	2-Apr-09	9:36	4.197	1.429	37.878	16.6	0.310	0.191
137	2-Apr-09	10:01	5.051	1.943	31.791	16.2	0.347	0.217
138	2-Apr-09	10:21	4.095	2.061	39.519	15.7	0.353	0.225
139	2-Apr-09	11:16	4.028	1.169	45.498	12.3	0.437	0.266
140	2-Apr-09	11:41	5.094	2.251	47.151	13.5	0.438	0.249
141	2-Apr-09	12:01	2.850	1.111	37.677	12.1	0.436	0.225
142	2-Apr-09	13:41	1.564	1.654	28.085	11.0	0.431	0.284
143	14-May-09	19:37	6.556	3.085	54.163	17.9	0.288	0.191
144	14-May-09	19:57	6.123	2.228	53.772	17.5	0.294	0.223
145	14-May-09	20:17	4.652	1.897	58.287	18.7	0.329	0.215
146	14-May-09	20:37	5.338	2.797	58.591	19.3	0.266	0.192
147	14-May-09	20:57	5.091	2.766	46.128	22.3	0.241	0.149
148	14-May-09	21:17	6.204	3.509	44.826	23.2	0.220	0.153
149	14-May-09	21:37	7.657	4.832	56.472	22.0	0.218	0.174
150	14-May-09	22:02	6.768	3.112	55.077	21.5	0.256	0.166
151	14-May-09	22:22	5.473	2.917	55.877	19.2	0.251	0.208
152	14-May-09	22:42	5.520	2.595	42.635	16.8	0.291	0.222

Table D.7 Data for Line b- Jumper

Data No.	Date	End Time	Peak-to-Peak Response			Unorm (m/s)	Iu	Iv
			H(m)	V(m)	T(deg)			
1	28-Dec-08	22:57	0.629	0.150	11.946	9.5	0.396	0.289
2	10-Jan-09	10:36	1.093	0.286	18.469	13.2	0.390	0.223
3	10-Jan-09	11:16	1.036	0.301	19.539	14.1	0.343	0.219
4	10-Jan-09	11:56	0.851	0.344	16.908	13.8	0.342	0.226
5	10-Jan-09	12:21	1.118	0.310	19.759	14.8	0.281	0.192
6	10-Jan-09	14:16	0.674	0.180	12.767	10.8	0.454	0.285
7	10-Jan-09	14:46	0.916	0.175	16.426	12.4	0.368	0.261
8	10-Jan-09	15:11	1.034	0.323	20.030	14.4	0.357	0.229
9	10-Jan-09	15:56	0.916	0.212	18.170	12.0	0.417	0.265
10	10-Jan-09	16:36	0.778	0.217	13.318	9.1	0.542	0.326
11	10-Jan-09	18:21	0.918	0.229	16.320	12.4	0.359	0.231
12	10-Jan-09	18:56	1.076	0.353	22.941	10.1	0.418	0.255
13	10-Jan-09	19:31	1.178	0.204	21.526	10.0	0.441	0.309
14	10-Jan-09	20:21	0.792	0.230	17.284	14.5	0.394	0.263
15	11-Jan-09	3:06	0.919	0.134	16.063	9.3	0.392	0.267
16	1-Feb-09	3:44	0.841	0.225	14.550	12.8	0.426	0.255
17	1-Feb-09	4:14	1.650	0.272	33.985	16.0	0.438	0.225
18	1-Feb-09	4:34	1.176	0.271	20.028	15.1	0.355	0.230



Table D.10 Data for Line c Quarter point (3rd span)

Data No.	Date	End Time	Peak-to-Peak Response			Unorm (m/s)	Iu	Iv
			H(m)	V(m)	T(deg)			
1	39850	0.558333	0.852769	1.444609	13.98519	10.0502	0.368043	0.227843
2	39852	0.447222	1.271777	1.804676	14.86247	12.69705	0.303502	0.211353
3	39852	0.471528	1.213806	1.827854	13.19531	12.53893	0.259114	0.210167
4	39852	0.485417	0.908968	2.242462	16.5328	12.25454	0.273309	0.201748
5	39852	0.520139	1.296313	1.780278	15.28035	13.05293	0.249977	0.185962
6	39852	0.540972	1.165473	1.562635	19.90649	13.32125	0.244618	0.173636
7	39852	0.558333	1.593126	1.303768	18.32528	14.15111	0.239079	0.170219
8	39852	0.572222	1.752056	1.319882	17.19914	15.46226	0.262438	0.170531
9	39852	0.603472	1.629598	1.640628	19.27067	16.18624	0.263305	0.17538
10	39852	0.624306	2.540743	1.294741	20.36149	15.06289	0.278589	0.195437
11	39852	0.638194	1.851113	1.759276	14.36442	14.9285	0.309291	0.191466
12	39852	0.655556	2.192636	1.851604	20.5328	15.82019	0.294764	0.181381
13	39852	0.672917	1.998123	1.382765	17.18734	13.55235	0.302484	0.211234
14	39852	0.686806	1.719193	1.553078	18.21566	13.87152	0.310816	0.201933
15	39852	0.707639	1.563736	1.376643	15.28499	11.58789	0.331279	0.234597
16	39852	0.721528	1.701554	1.212089	19.57259	12.44283	0.295313	0.225006
17	39852	0.784028	0.846962	1.712518	13.19865	10.31749	0.323978	0.224133
18	39863	0.345833	1.283804	0.894552	14.5988	11.26116	0.261913	0.206602
19	39869	0.803472	1.138644	0.901839	14.06901	11.54707	0.288101	0.197028
20	39879	0.3375	1.240377	1.836611	13.96647	10.4485	0.326059	0.22766
21	39882	0.920139	0.929344	1.386046	10.45101	11.0029	0.268545	0.193283
22	39883	0.135417	0.904689	1.148416	13.9825	10.16495	0.323078	0.249915
23	39883	0.149306	0.877119	1.041227	9.698649	11.35222	0.279133	0.168809
24	39886	0.885417	1.537104	1.440982	12.88037	6.584092	0.398239	0.328668
25	39893	0.13125	1.03981	1.656253	8.691162	10.56351	0.295207	0.203823
26	39895	0.297917	1.825363	1.269497	17.4506	14.40897	0.320779	0.213746
27	39895	0.436806	1.079549	1.295586	12.40698	11.30648	0.306394	0.217336

Table D.11 Data for Line c Middle point (3rd span)

Data No.	Date	End Time	Peak-to-Peak Response			Unorm (m/s)	Iu	Iv
			H(m)	V(m)	T(deg)			
1	39852	0.665278	2.971286	1.9873	20.72762	14.301	0.274469	0.207755

# APPENDIX - E

## FORCE COEFFICIENT FOR CONDUCTORS

Table E.1 Details of conductors for which drag coefficient is found

記号	実験者	年	供試電線	外 径 $D$ (mm)	素 線 径 $d$ (mm)	形状指数 $d/D$	測定最大 Re数 $\times 10^5$
○	近藤 (東大) <sup>(1)</sup>	1951	500mm <sup>2</sup> A.C.S.R	29.3	4.2	1/7	0.85
●	〃	〃	480 〃	31.5	4.5	〃	0.63
×	〃	〃	240 〃	22.4	3.2	〃	0.6
△	〃	〃	200 〃	20.3	2.9	〃	0.6
□	〃	〃	160 〃	18.2	2.6	〃	0.5
⊙	〃	〃	430 〃	29.2	4.6	1/6.3	0.95
△	〃	〃	410 〃	28.5	4.5	1/6.3	0.95
⊠	高野 (東大) <sup>(2)</sup>	1961	330 〃	25.3	4.0	1/6.3	0.59
⊗	〃	〃	240 〃	22.4	3.2	1/7	0.53
⊗	青木 (電研) <sup>(4)</sup>	1964	240 〃	22.4	3.2	1/7	0.6
⊗	〃	〃	330 〃	25.3	4.0	1/6.3	0.7
⊗	〃	〃	410 〃	28.5	4.5	1/6.3	0.8

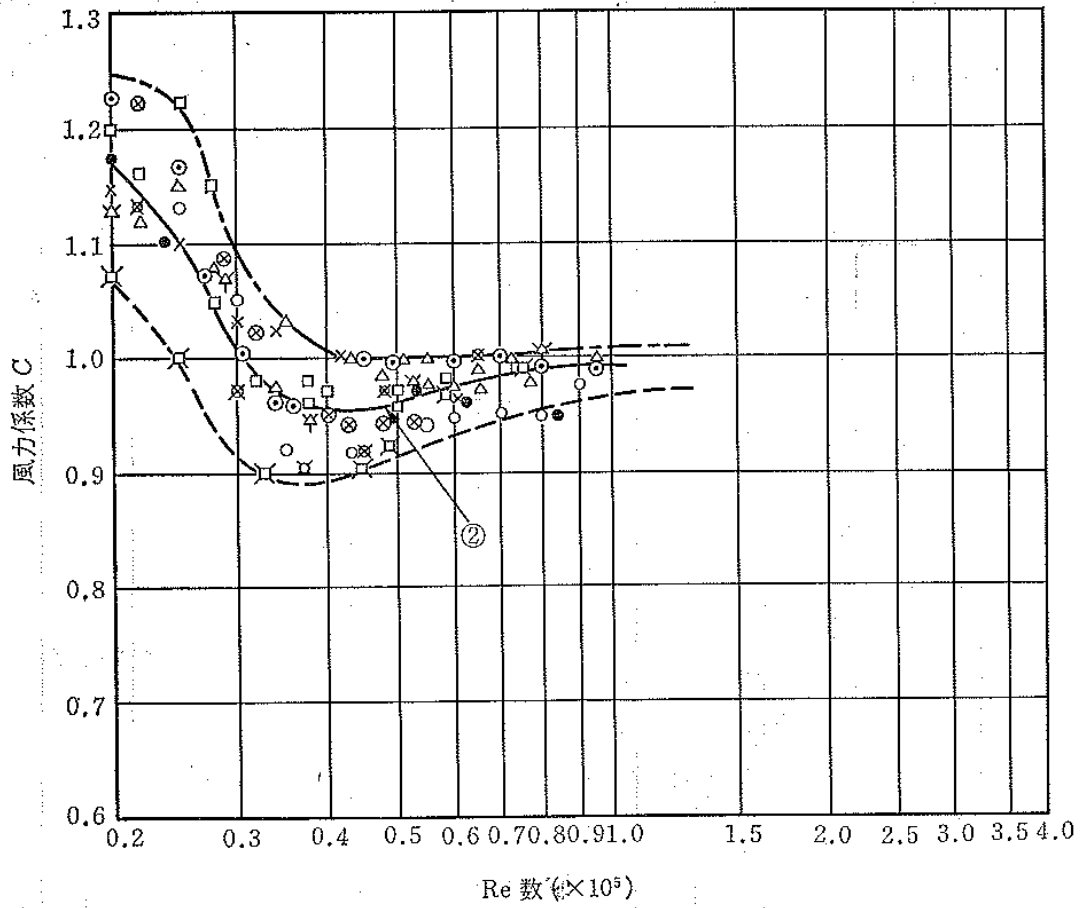


Fig. E.1 Drag coefficient for different conductor (Provided by Tokyo Electric Power Company)

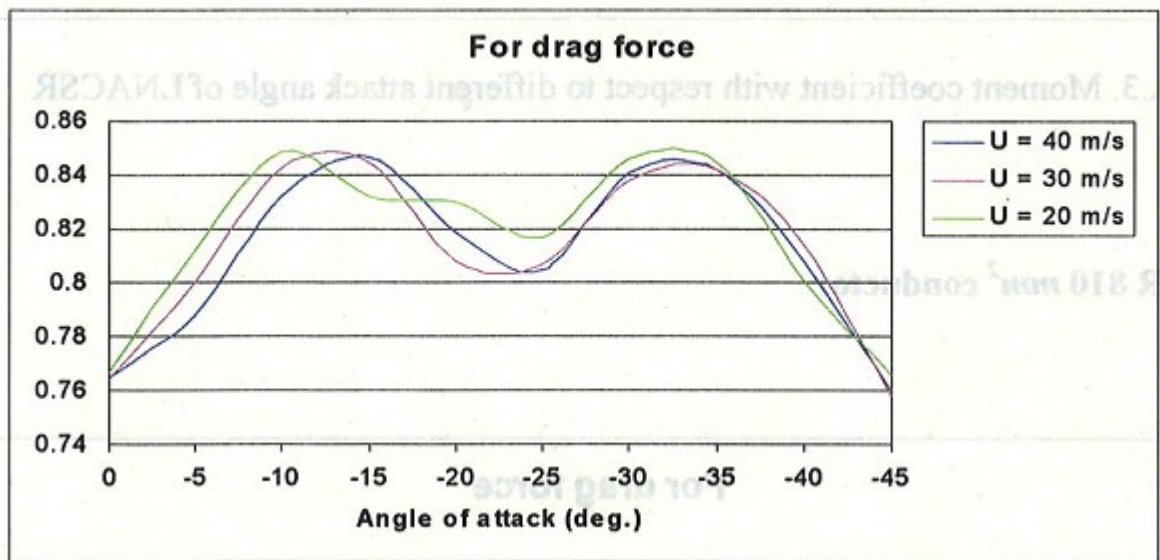


Fig. E.2 Drag coefficient for conductor -LNACSR-940mm<sup>2</sup> (Provided by TEPCO)

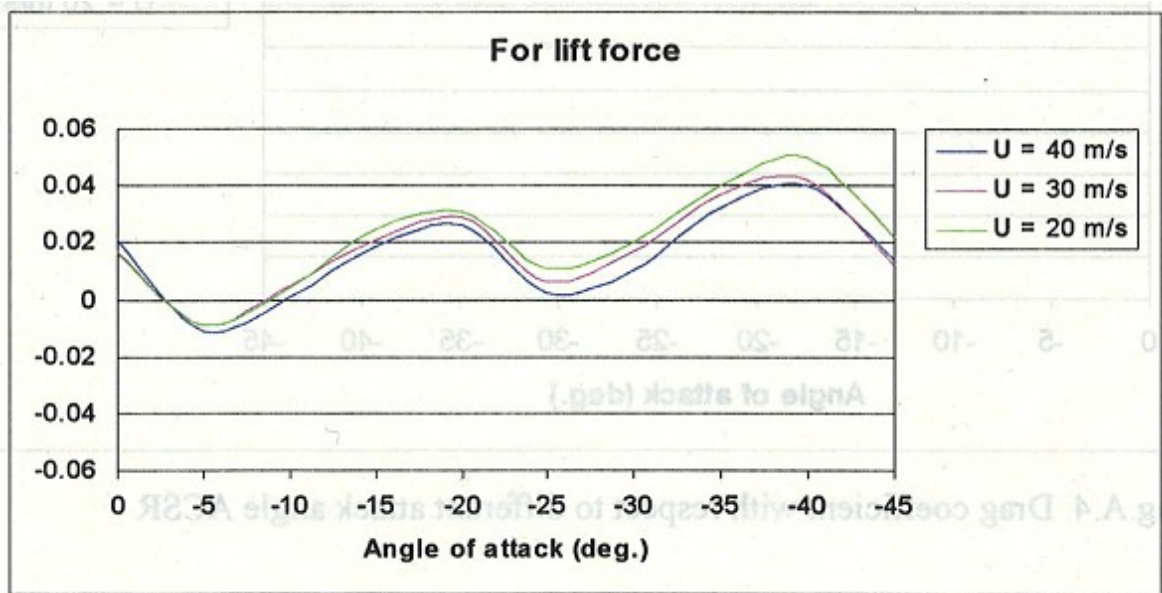


Fig. E.3 Lift coefficient for conductor -LNACSR-940mm<sup>2</sup> (Provided by TEPCO)

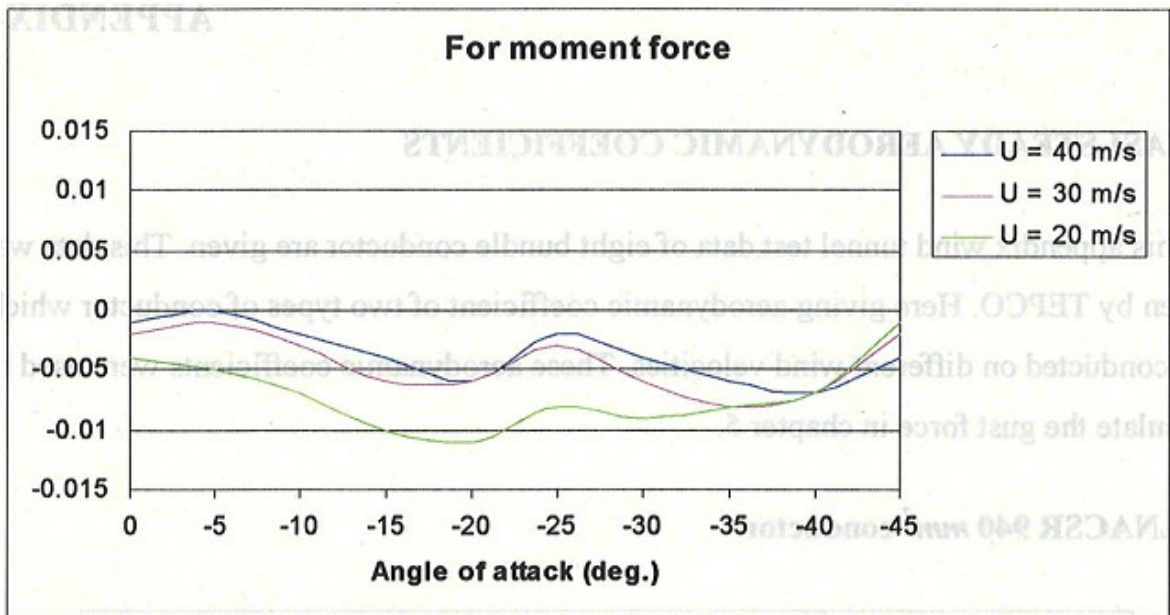


Fig. E.4 Moment coefficient for conductor -LNACSR-940mm<sup>2</sup> (Provided by TEPCO)